FACULTY OF SCIENCE AND TECHNOLOGY

MASTER'S THESIS

Study program/Specialization: Petroleum Technology/Drilling	Spring semester, 2017 Open
Author: Muhammad Yasser Haddad	…… (signature of author)

Supervisor:
Dr. Mahmoud Khalifeh

Title of master's thesis:

Theoretical Study on Utilization of X-ray Techniques for Verification of Casing Cement

Credits (ECTS): 30

Keywords: Cement Evaluation Plug & Abandonment Photons X-rays Compton Fiber Optics	Number of pages: 87 Stavanger, 15th of June/2017

Page intentionally left blank

Abstract

Establishing a hydraulic seal that prevents flow is the primary objective of any cement job, as it is essential throughout the life of a well. Evaluation of the cement in the annulus must be done to verify its quality. Tools based on acoustics are market leaders, although having limitations that may cause erroneous conclusions. It is of interest to find tools based on other principles that either replaces or supplements acoustic logs.

The thesis covers briefly barrier establishment, acoustic and fiber optic principles. A preliminary investigation into x-ray viability for cement evaluation has been done. Photon interactions, generation, detection and their subsequent challenges were also discussed. Heavy emphasis was placed on Compton scattering, as this is the basis for allowing both the transmitter and detector to be placed on the same side. To determine the viability of x-rays downhole several scenarios were created. We considered a single photon traveling through casing and a selection of materials before it is reflected at an angle.

Initial results based scenarios with concentric and eccentric cemented $9\frac{5}{8}$ casing showed that investigation of the cement-formation interface is too demanding of x-rays as it failed to provide sufficient penetration of the casing on its return. The attenuation due to Compton scattering is significant, dependent on energy level and angle of the beam it can reach 80% attenuation. The angle of reflection or transmission will provide additional attenuation due to added length of travel path for the beam. Material density must be taken into consideration, as it influences the attenuation rate of the x-rays beam. The beam experienced high degree of attenuation when passing through casing, the attenuation contrast between casing and cement was discernable. Materials such as foamed cement, seawater and gas were also investigated. All of the latter materials allowed for increased transmission compared to casing and cement. The contrast between foamed cement and seawater was low and of concern for applicability of x-rays for foamed cement evaluations. Gas channels in cement are easily detected if the size of channel is sufficient.

Investigation of the cement-formation interface did not provide satisfactory results due to the inability of the beam to return to the detector before complete attenuation. Reduction of the depth of investigation may provide satisfactory results and should be investigated.

Page intentionally left blank

Acknowledgments

I would like to thank my thesis supervisor Dr. Mahmoud Khalifeh of University of Stavanger for accepting and helping me develop my initial proposal. The writing of this thesis was not an easy task as there was many aspects to consider. His availability for any questions I had regarding the topics and structure was invaluable. The culmination of this thesis would not have been possible without the supervision and guidance provided by him.

I would also like to extend my gratitude towards Dave Gardner of IRIS, for allowing me to present my work and guiding me towards relevant papers.

I owe my deepest gratitude to my family and friends for keeping my spirits high not only during the writing of this thesis, but the last five years at the University of Stavanger.

List of Figures

List of Tables

Abbreviations

P&A	Plug and abandonment
WBS	Wellbore schematic(s)
MSD	Measured depth
DAS	Distributed acoustic sensing
DTS	Distributed temperature sensing
PMT	Photomultiplier tube
NCS	Norwegian Continental Shelf
UKCS	United Kingdom Continental Shelf
CBL	Cement Bond Log
VDL	Variable Density Log
USIT	Ultra-Sonic Imaging Tool
CET	Cement Evaluation Tool
SBT	Segmented Bond Tool
NIST	National Institute of Standards and Technology
Csg.	Casing
HSE	Health, Safety and Environment
$^{137}_{55}CS$	Caesium-137
NaI	Sodium Iodide
TI	Thallium

Nomenclature

Symbol	Denotes
E	Energy of photon
f	Frequency
h	Plank's Constant
c	Speed of light
λ	Wavelength
V_p	Velocity of the refracted P-wave
V_s	Velocity of the refracted S-wave
V_m	Velocity of the reflected P-wave
v	Phase velocity
n	Refractive index
θ	Scattering angle
Δv	Raman wavelength shift
T	Temperature
I	Intensity
C_- / C_+	Measured constants for DTS calculations
k	Boltzmann's constant
Z	Atomic number
$\Delta\alpha$	Difference in Attenuation rate
T_p	Period
P	Momentum
ϕ	Recoil electron angle
q	Electric charge
L	Mean escape length of excited electrons
ε	Normalized photon energy

Symbol	Denotes
γ	Pyroelectric coefficient
σ	Surface charge
HU	Heating units
J	Joule
Q	Heat
c_s	Specific heat
m	Mass
τ	Decay time
$(\frac{d\sigma}{d\Omega})$	Cross section
$\Delta\Omega$	Solid angle
N	Number of particles per unit area
E_K	Kinetic energy
Z_L	Depth/Distance
θ_1	Incident angle to the normal
θ_2	Refraction angle to the normal
$\theta_{critical}$	Critical angle
L	Length
t	time
T_{ref}	Reference temperature
β	Beta particle
Hz	Hertz
I_- / I_+	Anti-Stokes and Stokes intensities
I_0	Incident intensity
eV	Electron Volt

Symbol	Denotes
f'	Scattered photon frequency
η	Quantum efficiency
M	Molar Weight
ΔV	Differential voltage
k_α	K alpha x-rays
k_β	K beta x-rays
E_{e-}	Conversion Electron
E_{ex}	Excitation energy
E_B	Binding energy
σ	Surface charge
γ	Pyroelectric coefficient
R	Reflection coefficient
k	Full absorption coefficient of photons
P_V	Probability that light absorption may excite electrons to a level greater than vacuum level
P_s	Probability that electrons reaching the photocathode surface may be released into the vacuum
$a\tau$	Photoelectric attenuation coefficient
ft.	Feet
m	Meters

Symbol	Denotes
r_e	Radius of electron
$\bar{\omega}$	Fluorescence (characteristic) yield
P	Pressure
I_x	Attenuated intensity
I_{sc}	Scattered photons
E_K	Kinetic energy
P_v	Incident photon momentum
P_e	Recoil electron momentum
P_v'	Scattered photon momentum
m_e	Electron rest mass
F_{KN}	Klein-Nishina form factor, $f(h\nu, \theta)$
ρ	Density
R	Gas constant
μ/ρ	Mass attenuation coefficient
μ	Linear attenuation coefficient
‘’	inch
mm	Millimeters

Table of Contents

Page intentionally left blank

1 Introduction

Achieving a qualified zonal isolation in the casing-formation annulus is one of the main parameters for maintaining well integrity throughout a wells life cycle. The barrier elements that contribute are present during drilling, production and abandonment of the well. The latter begins with a plug and abandonment operation, also known as P&A. The operation is increasingly becoming a focus as demand is growing within the industry. All drilled wells will eventually be decommissioned and will require P&A. These operations provide no financial return for the operators (Abshire et al. 2012), and is mandated by several regulatory governmental bodies (Norsok D-010 2004, Oil & Gas Uk 2012a). Numerous wells on mature fields currently require decommissioning (Eshraghi 2013, Oil & Gas UK 2016) current drilling operations and future waves of wells means that P&A will stay prevalent long after the last oil has produced. Current methods of well abandonment require expensive equipment and time-consuming operations (Eshraghi 2013, Liversidge and Taoutaou 2006). Incremental improvements are beneficial as the economic costs are vast. Step-changes would alter the economic landscape for the industry.

Evaluation of the zonal isolation behind the casing is a crucial part of the planning of a P&A operation. The conclusion of the evaluation can decide between in a simple operation with a vessel, or a complex operation that requires removal of tubulars by using a rig. Acoustic tools that use soundwaves to penetrate the metal and gather information about the barrier dominate the market today. Variations of these tools are plentiful, but all are based on the same principles. Tools that uses a different method of investigation is rare, due to the inherent difficulty of penetrating the metal.

In the medical field, x-rays are used to gather knowledge about the bone structure of a patient among other methods (Podgorsak 2010). Border agencies use the technology to inspect luggage, cars and containers for illicit materials (Zentai 2008). The latter use of x-rays is of interest for zonal isolation evaluation. Adaptation of the technology for the oil and gas industry is not straight forward as the environmental and size conditions are vastly different.

This thesis sets out to provide a brief overview of acoustics and fiber optics. We will then examine several aspects of x-rays from generation, detection to x-ray interactions. The later chapters will analyze the viability of x-rays and discussion of the different parameters pertaining to x-rays.

The following chapter will provide a general insight into P&A operations, regulations and scope of P&A work.

2 Cementing a Well

2.1 Primary Cement

Primary cementing is important as it affects several aspects of a well, such as prevention of migration of reservoir fluids and stabilization of the casing. We will briefly discuss why there is a need for primary cement before moving on to plug and abandonment.

To optimize production, a good cement job as a foundation is necessary to prevent cross-flow between two formations. This phenomenon can occur due to reservoir depletion. As 15 % of all cementing jobs fail, costing an estimated USD 450 million. Thus, ensuring zonal isolation is crucial. The primary reasons for failures are as follows (Nelson and Guillot 2006):

- Improper balancing of pressures leading to mud and reservoir fluid contamination of cement
- Movement of pipe and cement during production
- Poor hole cleaning

The main objective of any cement job is to provide zonal isolation, which is effectively a hydraulic seal that is meant to prevent communication between two formations. Secondary objectives are to stabilize the casing and prevent corrosion. During production, the cement is susceptible to cracking and debonding, which reduces the effectiveness of the cement to provide zonal isolation.

2.2 Plug & Abandonment

The decision to P&A a well is a function of economy. If the production from the well does not cover the operational expenses, the well is a candidate for abandonment procedures. There are additional reasons for abandoning a well, some encounter problems during drilling that are too costly to repair or a well can be rerouted by plugging and starting a new path above the plug. Well integrity issues may require P&A of the original wellbore and lead to slot recovery. In any case, the intent of P&A is (Abshire et al. 2012):

- Isolate and protect all fresh and near freshwater zones
- Isolate and protect all future commercial zones
- Prevent leaks in perpetuity from or into the well
- Remove surface equipment and cut pipe to a mandated level below the surface

There are mainly two types of abandonment according to NORSOK D-010 and UK O&G, which are listed below (Norsok D-010 2004, Oil & Gas Uk 2012a)

- Temporary abandonment where one has the intent to return to the well
- Permanent abandonment where one has no intention to return to the well

The result of a permanent P&A operation is the restoration of the seabed or land to its initial condition, in other words restoring the cap rock. It entails removing or at least minimize any trace of the existence of the well. The removal of visible equipment on surface is one of the last steps,

as there are several steps downhole that need to be completed. As mentioned, the purpose of the barriers is to seal possible migration paths for well fluids to surface. The location of these barriers has to account for the fracture pressure, pore pressure, hydrocarbon gradients among other factors. Ahead of the operation start, one should perform an assessment of the conditions downhole. Planning these operations is critical to minimize the time, consequently money, spent on plugging each well.

There is an increased demand from the regulatory bodies to achieve a cross-sectional barrier shown in Figure 2-1 (Abshire et al. 2012), which is a barrier that does not allow any flow across it regardless of direction. To determine if the barrier conforms to the demand, it has to be evaluated. Currently this means the removal of production or injection tubing, log the casing cement to evaluate its condition and determine if it fulfills the requirements. If it is determined that there is poor zonal isolation, the usual course of action is to mill the casing and annuli cement.

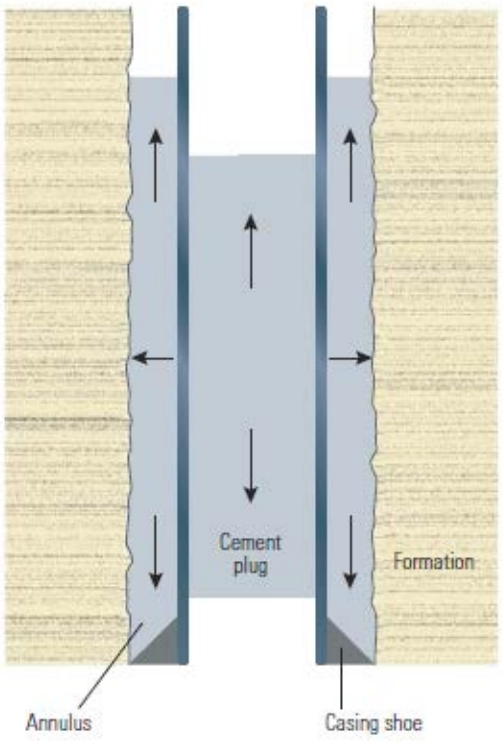

Figure 2-1- Cross-sectional plug (Abshire et al. 2012)

This action is time consuming and expensive, as it can take approximately ±40% of the time for a P&A operation (Scanlon and Garfield 2011). There are technologies that seek to replace or supplement the method like perforate, wash, cement technology, yet the best practice to ensure proper barrier placement might be through milling.

2.3 Well Barriers

NORSOK D-010 defines the barriers placed in a well by different categories. Presentation of these definitions can be found in Table 2.1. The placement of primary and secondary barriers is shared by both permanent and temporary abandonments while the surface/environmental barrier is only found in permanent abandonment.

Table 2.1 - Definitions of barriers

Barrier type	Definition
Primary	To isolate a source of inflow, formation with normal pressure or over-pressured/ impermeable formation from surface/seabed.
Secondary	Back-up to the primary well barrier, against a source of inflow
Crossflow well barrier	To prevent flow between formations (where crossflow is not acceptable). May also function as primary well barrier for the reservoir below.
Surface/Environmental	To permanently isolate flow conduits from exposed formation(s) to surface after casing(s) are cut and retrieved and contain environmentally harmful fluids. The exposed formation can be overpressured with no source of inflow. No hydrocarbons present.

What constitutes a well barrier envelope is several well barrier elements. Alone, each element is not sufficient to prevent flow across it but along with other elements, they form a well barrier envelope that is able. A well barrier envelope cannot be dependent on a single element, meaning no single failure of an element shall cause a failure of the entirety of the well barrier (Norsok D-010 2004). Shown in Figure 2-2 are examples of well barriers and their well barrier elements. In these wellbore schematics (WBS), the blue indicates the primary, red the secondary and green the surface/environmental barriers.

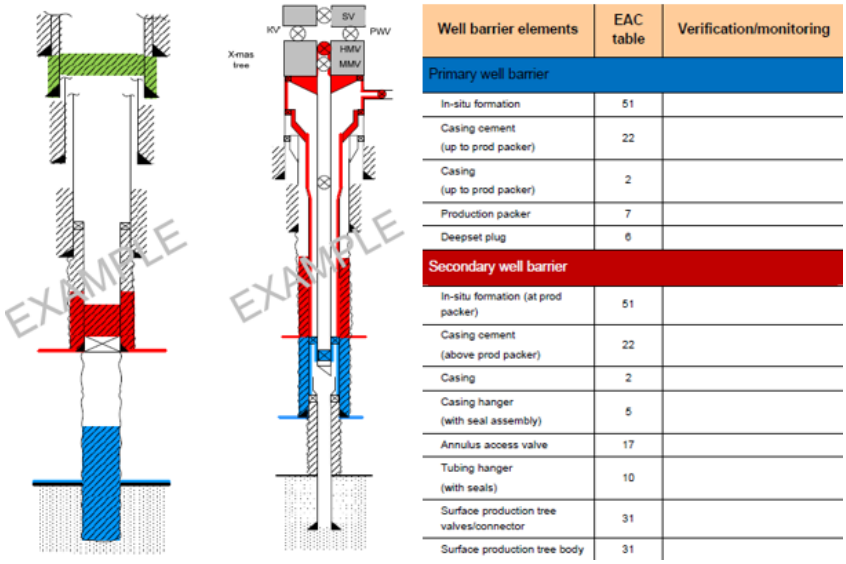

Well barrier elements	EAC table	Verification/monitoring
Primary well barrier		
In-situ formation	51	
Casing cement (up to prod packer)	22	
Casing (up to prod packer)	2	
Production packer	7	
Deepset plug	6	
Secondary well barrier		
In-situ formation (at prod packer)	51	
Casing cement (above prod packer)	22	
Casing	2	
Casing hanger (with seal assembly)	5	
Annulus access valve	17	
Tubing hanger (with seals)	10	
Surface production tree valves/connector	31	
Surface production tree body	31	

Figure 2-2 - Examples of WBS with well barriers and example table of well barrier elements. From left to right: Permanent abandonment, temporary abandonment and its well barrier elements. (Norsok D-010 2004)

The requirements set by NORSOK D-010 views the well barriers differently for the two types of abandonment. For temporary abandonment, the well barrier elements do not have to be everlasting, allowing for the use of mechanical well barrier elements with the condition that they will lasts twice as long as the predetermined abandonment time. The inclusion of monitoring and routine testing of the barriers, allows temporary abandonment to exceed the time limit of three years without monitoring. Permanent abandonment has one time requirement, that the barriers placed are everlasting.

2.4 Materials

So far, we have discussed the types of abandonment and well barriers. The focus of the following section will be on a particular well barrier element, cement. The use of cement in the industry is prevalent, and in addition to provide zonal isolation its function is to stabilize the casing once set in the borehole. The most common type is class G cement. Additives can be added to a neat cement to enhance strength, decrease or increase setting time and reduce density. Portland cement does not fulfill all the requirements found in NORSOK D-010 and UK Oil and Gas (van der Kuip et al. 2011), but is inexpensive and companies are experienced with the material. The requirements in NORSOK D-010 for material selection are presented in the list below, and Oil and Gas UK shares many of the same requirements (Norsok D-010 2004, Oil & Gas UK 2012b)

- Provide long-term integrity (eternal perspective);
- Impermeable
- Non-shrinking
- Able to withstand mechanical loads/impact
- Resistant to chemicals/substances (H_2S, CO_2 and hydrocarbons)
- Ensure bonding to steel
- Not harmful to the steel tubulars integrity

In addition to the requirements above, the length of the barriers is also pre-determined, presented in Table 2.2. The requirements differ for each country, a comprehensive list can be found in the following reference (van der Kuip et al.).

Table 2.2 - Length requirements of the cement plugs based on location (Norsok D-010 2004, Oil & Gas UK 2012b)

Placement	NORSOK D-010	Oil & Gas UK
Annuli – Not verified	50 m	100 ft.
Annuli – Verified by logging	30 m	100 ft.
Internal	30 m	100 ft.

2.5 Challenges

There are several challenges concerning cementing that need to be considered to ensure that no leaks reach the surface. Improper placement of cement can lead to a multitude of issues like contamination, channeling and lower than expected compressive strength. The techniques for cement placement can be found in the paper (Khalifeh et al. 2013). In this section, we will continue

with the assumption that cement has been improperly placed and not able to provide good zonal isolation.

There are three paths for hydrocarbons to flow (Skalle 2001):

- Through wellbore
- Through cement behind casing
- Through formation

Concerning the second point on the list. Cement slurry goes through two stages before finally setting, which are liquid to a gel before becoming a solid. In the liquid form, the pore pressure of the cement can be lower than the gas pressure, causing the cement to yield and allow gas in the matrix. As the cement hardens, the original volume of the cement becomes smaller. During the shrinkage, water and gas might be sucked into the pores as they develop in the cement. Higher temperatures reduces the problem as the hydration of cement occurs at a faster rate decreasing the available window for water and gas to be trapped inside (Skalle 2001, van der Kuip et al. 2011). Figure 2-3 shows numerous failures that can occur in cement and its bonding.

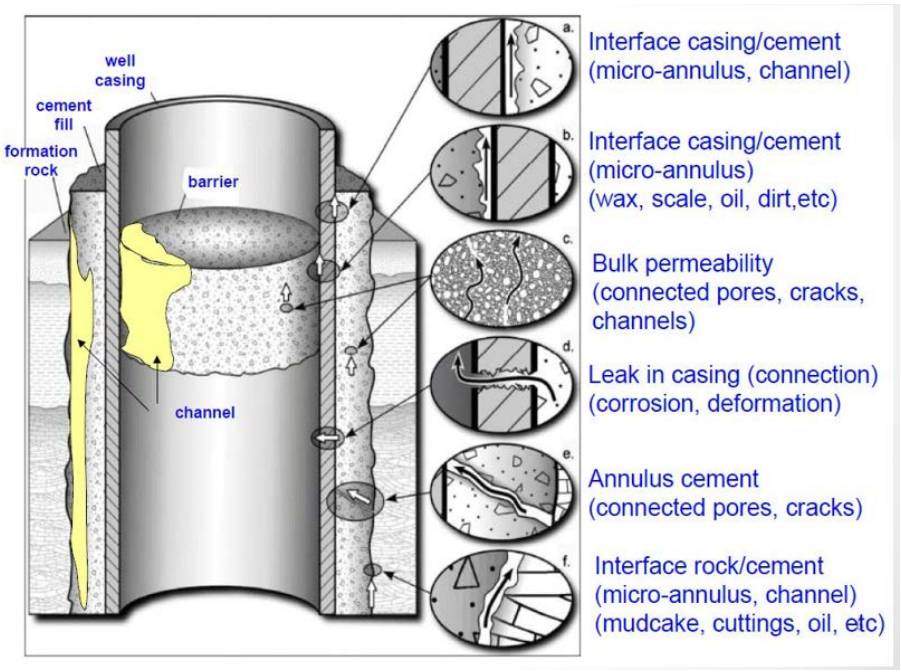

Figure 2-3 - Migration paths for fluids (Oil & Gas UK 2012b)

The appearance of CO_2 is a detrimental factor as it may cause damage to the cement over time, degrading the zonal isolation it provides. The causes for this can be that the gas enhances the porosity and permeability of the cement or corrodes the casing steel, creating new paths for migration. Extrapolation of laboratory results show that CO_2 can penetrate 1 m of cement after 10000 years. At conditions with elevated temperatures and lower pH, the penetration can reach 12.4 meters (van der Kuip et al. 2011). Mechanical loads from operational activities can cause de-bonding, which is separation of the casing-cement and cement-formation bonds that is conducive for the creation of new paths for leaks. A summary of the challenges in the North Sea is presented below (Scanlon and Garfield 2011).

- Tectonic stresses (shear stress and subsidence) are exerted by the formation
- High temperature
- Unconsolidated formations
- Well design
- Formation permeability
- Changes in formation because of depletion
- Lack of data of old drilled wells including cementing data
- Uncertain ultimate reservoir pressure after abandonment
- Deep section milling of casing

2.6 Plug and Abandonment Scope

As mentioned in the introduction the economic scope of P&A operations is immense, the following chapter will give a brief overview of what lies ahead.

The number of wells that require abandonment in the short term and in the future is not a certain quantity. This is due to the various factors that play a role when marking a well for decommissioning. Postponement of planned projects can occur if the operator is able to extend the life of a well, or if the economic situation is such that it is not feasible to plug a well permanently. Some operators may take advantage of the lower service rates due to the low oil price to move up planned projects. Therefore, any numbers presented by the industry is more of an indication of scope work and cost ahead.

For the United Kingdom Continental Shelf (UKCS), and Norwegian Continental Shelf (NCS), Oil & Gas UK is able to provide insight into future decommissioning work. The yearly expenditure for the work is presented in Figure 2-4 shows a substantial increase for the UKCS, while the NCS is expected not to increase its annual expenditure of GBP 1 billion. The discrepancy in cost is due to more mature fields in the UK sector (Oil & Gas UK 2016).

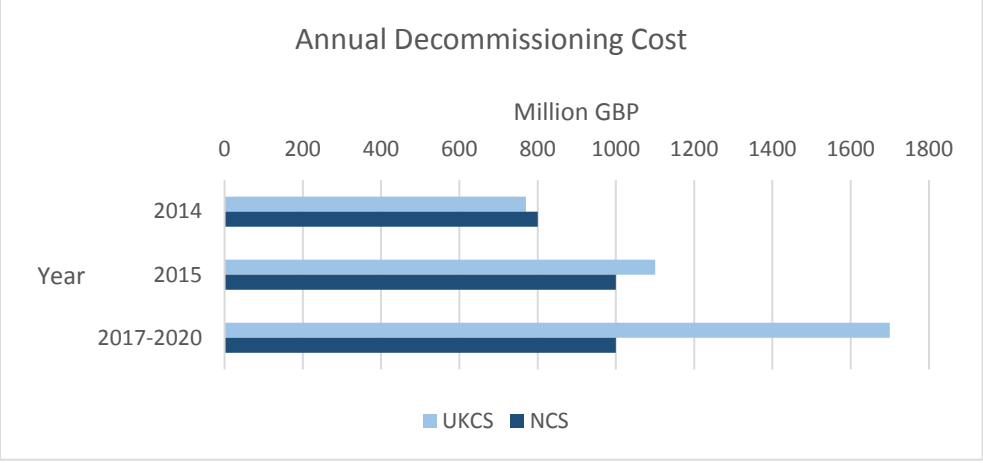

Figure 2-4 Annual Decommissioning Cost in the UKCS and NCS

The data presented in Figure 2-4 is for the total decommissioning work, which encompasses removal or partial removal of platforms, well abandonment and pipeline removal. Well abandonment accounts for a significant portion of the cost with 47% and 56% for UKCS and NCS

respectively. Expected average annual expenditure for the next ten years for NCS GBP 1 billion and GBP 1.7 billion for UKCS.

The number of wells expected to be plugged in the ten-year span of 2016 to 2025 is presented in Figure 2-5 (Oil & Gas UK 2016).

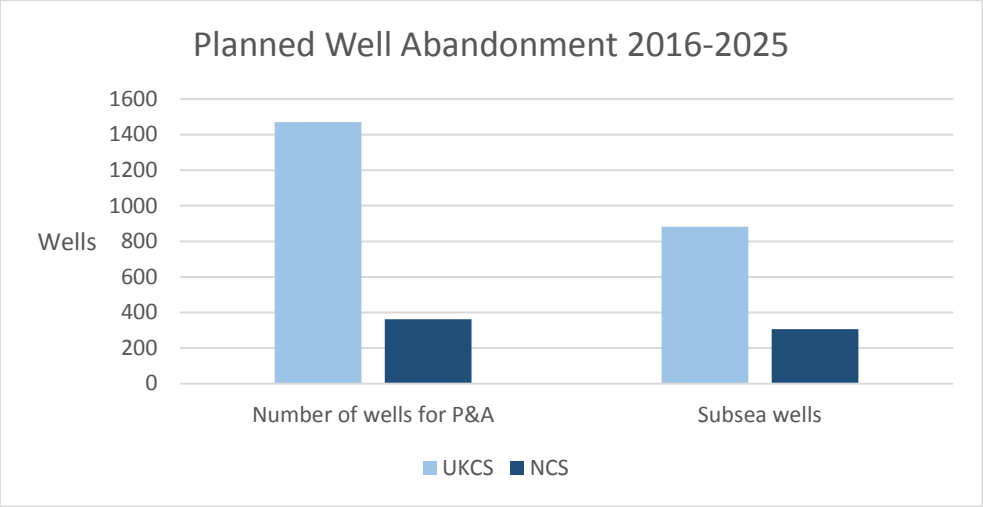

Figure 2-5 Number of planned well to be P&A in the UK and Norwegian continental sectors

So far, 3800 wells have been drilled on the NCS, with 3000 requiring abandonment in the future. Not taking into account new wells and assuming the expected pace of 35 wells each year in the future, it would take around 86 years to abandon these wells. The average cost of each well is presented in Table 2.3. One should take note that the values presented is just an estimate based on current costs, and may be subject to change in the future.

Table 2.3 - Average cost for plugging a well (Oil & Gas UK 2016)

	UKCS	NCS
Well type	Cost in million GBP	
Platform	3	10
Subsea exploration	6.1	16.1
Subsea production	9.6	16.1

The difference in cost for the UK sector and the Norwegian sector can be attributed to different regulatory agencies overseeing P&A operations and more expensive rates by the service providers.

3 Acoustics

Currently the most common and efficient method of cement evaluation is found in acoustic tools (Nelson and Guillot 2006). The method of investigation has been dominant since the 1950s, when the Cement Bond Log (CBL) was introduced. Since the introduction the understanding of sound propagation and interpretation of the measurements have improved (Benge 2016). Some of the principals of sound will be presented and an examination of how the different acoustic tools use sound to evaluate cement.

3.1 Principals

Sound propagation behaves differently in three phases of liquid, gas and solid. In the former density is affected due to compression and rarefaction, the latter experiences squeezing and stretching of the grains. The waves that can cause these motions are (Nelson and Guillot 2006):

- Compressional wave (P-waves): The motion of change occurs in the same direction as the propagation. This wave type can exist in both fluids and solids.
- Shear waves (S-waves): Motion is perpendicular to the propagation. This wave type only exists in solids.
- Plate wave: A wave that propagates in steel, with a lower velocity than the compressional wave.

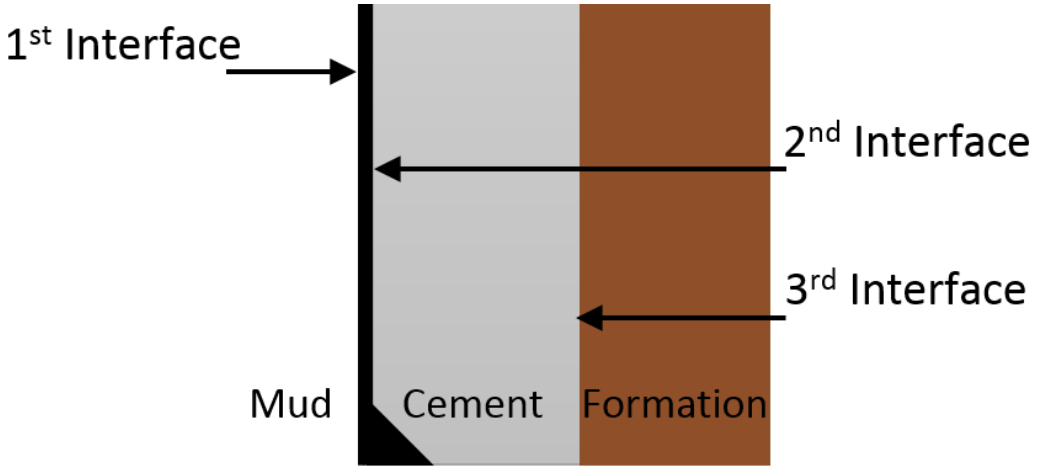

Figure 3-1 - Three interfaces in a wellbore

In Figure 3-1, we see the three different interfaces defined in Table 3.1. Our interest lie in the second and third interface, as knowledge about these will allow us to infer the quality of bonding the cement has with the casing and formation.

Table 3.1 - Definition of the interfaces

1st Interface	Mud – Casing
2nd Interface	Casing – cement
3rd Interface	Cement – Formation

A sound emitter placed inside a wellbore produces a sound wave. We assume a simple scenario, where tool effects are ignored and that the formation is homogenous and isotropic. In simplified 2D view, one can imagine the wave propagates as a circle from the transmitter. In reality, the wave propagates as a sphere that will make the scenario more complex but the principles stay the same (Haldorsen et al. 2006). The wave will travel through the mud, and interact with the first interface. The incident wave will be separated into three components with different velocities. One components will be reflected and the remaining two will be refracted towards the next interface as seen in Figure 3-2.

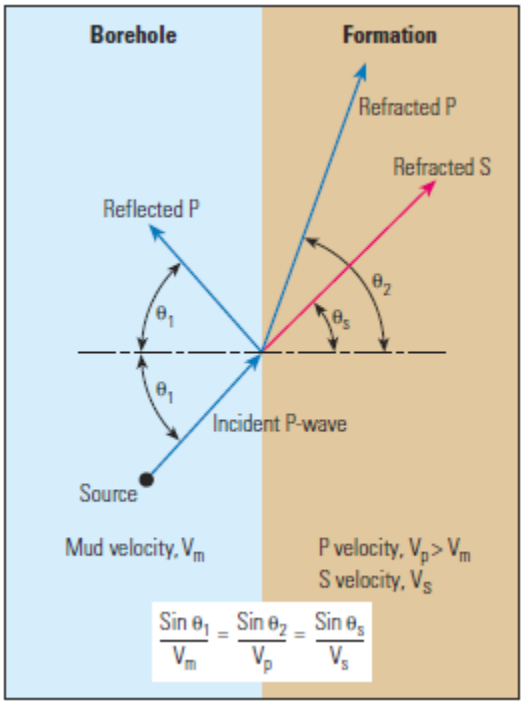

Figure 3-2 - Decomposition of the incident wave into three waves (Haldorsen et al. 2006)

According to Huygens principle, every point along an interface hit by a P-wave creates new sources for P and S waves (Haldorsen et al. 2006). The order of the velocities of the refracted P- and S-waves and the reflected P-wave in Figure 3-2 is as follows, $V_p > V_s > V_m$.

The rate of attenuation, loss of energy, of a sound wave is dependent on the intrinsic properties of the medium it travels through. Compact formations have little attenuation, while loose formations will cause a high degree of attenuation. This is due to the space between the grains, which makes it difficult for the vibration to travel from grain to grain. Formations experience little change in acoustic properties over time, the opposite is true for cements. The same type of cement pumped downhole can have variations with depth, due to different curing temperatures (Nelson and Guillot 2006).

3.2 Sonic

The CBL-VDL, variable density log, sonic tool has two receivers spaced at 3-ft and 5-ft and an omnidirectional transmitter that emits a sound wave with a frequency between 10 – 60 Hz, shown in Figure 3-3. The 3-ft is used to measure the amplitude of the first arrival while the 5-ft receives the full-wave presentation of the received signal. Laboratory experiments have shown that the compressive strength of the cement and the amplitude are related. As mentioned earlier, the attenuation of a sound wave it dependent on the properties of the material meaning that a relative lower measured amplitude would indicate cement. (Albert et al. 1988, Nelson and Guillot 2006, Schmidt 1989).

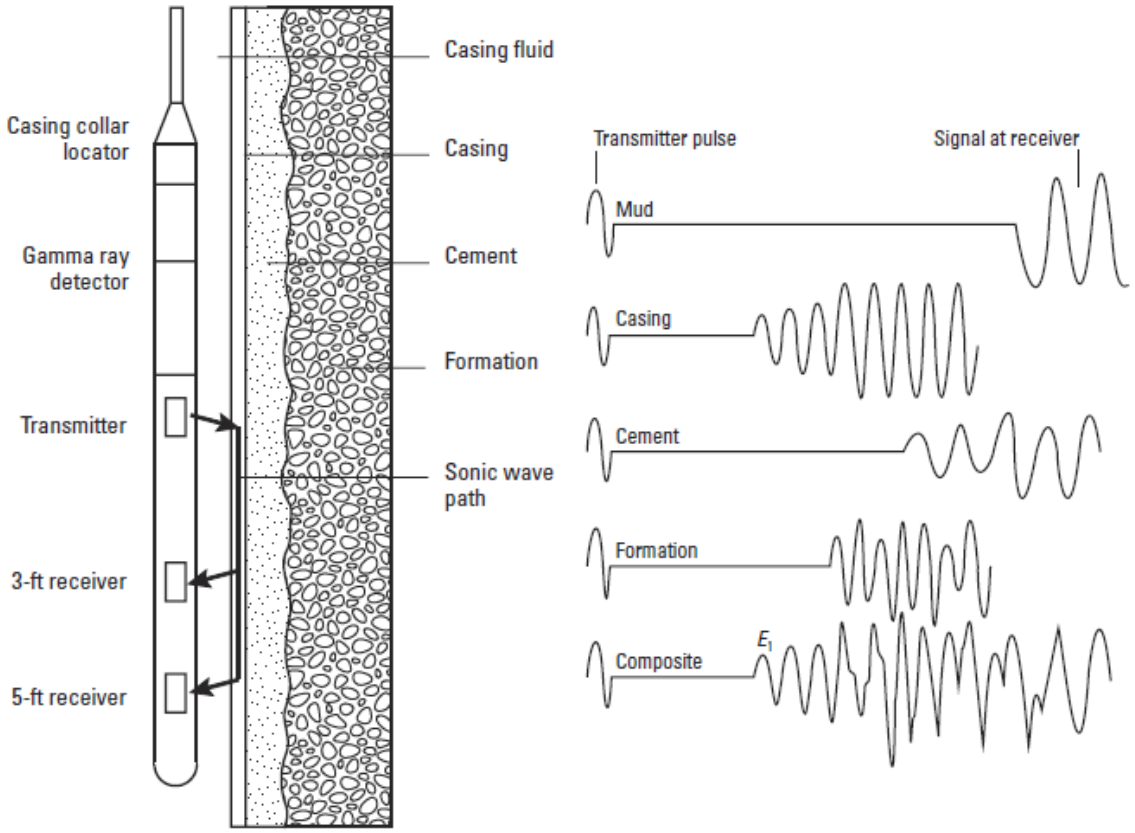

Figure 3-3 CBL-VDL tool configuration and signal arrivals. (Nelson and Guillot 2006)

The mud signal even though it has the shortest distance to travel is the slowest among the three and will be the last signal to arrive at the receiver. The other arrivals, casing, cement and formation are shown in Figure 3-3. Since the transmitter used in this tool is not able to discern direction, it will average the signal arrivals from a section. The 3-ft receiver is used to investigate the 2nd interface. The 5-ft-receiver is used to investigate the 3rd interface, and receives the composite signal in Figure 3-3. The interpretation of this signal is qualitative, thus the attenuation of the signal is of not high concern (Nelson and Guillot 2006).

Segmented Bond Tool (SBT), reduces the limitation of signal averaging since it can investigate 60° at a time. The principles of investigation are the same as CBL (Pilkington 1992).

3.3 Ultra-Sonic

The older Cement Evaluation Tool (CET) and newer Ultra Sonic Imaging Tool (USIT) use higher frequencies, around 200 to 600 KHz (Leigh et al. 1984), than the CBL tool to investigate the cement bond. Instead of a transmitting a signal 360° in the wellbore, USIT is able to discern direction of investigation. The USIT has a transducer, which acts as both transmitter and receiver (Shook and Lewis 2008), that while rotating will emit a sound wave that will resonate the casing. If there are fluids present behind the casing the resonance will be high, comparatively if there is cement behind the casing the resonance will be dampened, this can be seen in Figure 3-4.

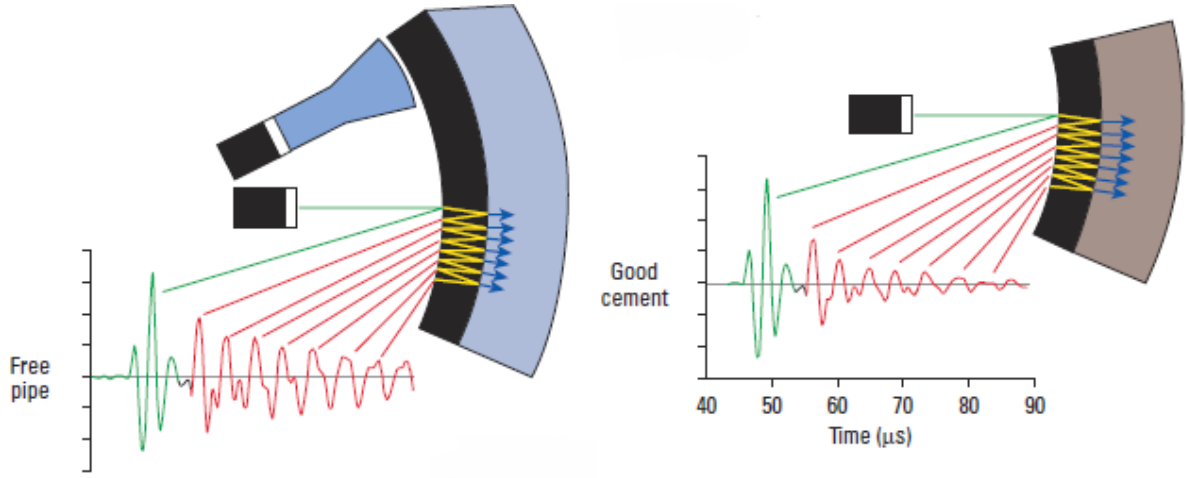

Figure 3-4 - Resonance measurements in free pipe (left) and good cement (right) (Nelson and Guillot 2006)

These tools are used to alleviate some of the limitations of sonic tools (Jutten and Hayman 1993), which will be presented in the following chapter.

3.4 Limitations of Sonic Tools

"…CBL, despite its great potential, is probably one of the most abused, misused, and misunderstood logs run in the oil field today."

- Fertl, Pilkington and Scott 1974 (Fertl and Pilkington 1974)

While CBL has been staple for cement evaluation in the industry for decades, it has its limitations and considerations that need to accounted for. Some of these are presented below:

- Standardization and calibration
  - The industry has not standardized the tool itself and the frequencies used. Which can lead to different companies presenting different conclusions and consequently can result in confusion among the petroleum engineers. Calibration of the tool as well has not been standardized. (Fertl and Pilkington 1974, Fulton 1979).

- Centralization
    - As the transmitter is omnidirectional, good centralization is a requirement. As the method of investigation is dependent on signal arrivals, eccentric receiver leads to erroneous results, up to 50 % reduction in amplitude (Ashena, Thonhauser, and Dianati 2014, Fertl and Pilkington 1974, Nelson and Guillot 2006, Schmidt 1989).
- Temperature and Pressure Effects
    - Sound velocity is affected by temperature, not considering the temperature effects can lead to different than expected signal arrivals (Nelson and Guillot 2006, Schmidt 1989).
    - The compaction of mud due to pressure effects can lead to higher attenuation (Nelson and Guillot 2006).
- Microannuli
    - The presence of microannuli affects the sonic attenuation. Gaps filled with air or water of a certain size in the cement can show similar attenuation as free-pipe. Requiring the tool to be run under pressure to eliminate microannuli (Fulton 1979, Jutten and Hayman 1993, Pilkington 1992).
- Casing and Cement Thickness
    - Increased attenuation of the signal due to increased thickness. Uncertainty in casing thickness change to due to corrosion leads to uncertainty in the log. If the cement sheath is below a certain thickness, the casing signal is not completely attenuated (Ashena, Thonhauser, and Dianati 2014, Nelson and Guillot 2006, Pilkington 1992).
- Fast and slow formations
    - In highly compacted formation like limestones and dolomites, the acoustic wave travels faster and arrives at the receiver earlier and can interfere with the casing arrivals (Ashena, Thonhauser, and Dianati 2014, Schmidt 1989).
    - Unconsolidated formation increase attenuation due to the distance between the grains increases the difficulty for the sound wave to move from grain to grain (Nelson and Guillot 2006)

The culmination of the limitations and considerations above affects the bond index (Haldorsen et al.). This index is used to indicate the presence of cement in the annuli, using laboratory reference values and comparing it to the field values one can estimate the fill percentage in the annuli (Benge 2016). The selection of the reference value is dependent on knowledge of a wells history, making the historical data a requirement. According to Pilkington (Pilkington 1992) CBL provides a good assessment of the cement if the tool and interpretation are properly run and read.

3.5 Limitations of Ultra-Sonic Tools

Limitations inherent in acoustic tools are shared between sonic and ultra-sonic tools. The use of higher frequencies will reduce some of the limitations found in sonic tools, and introduces its own limitations. The limitations and considerations to account for with ultra-sonic tools are presented below:

- Sensitivity to gas
  - If gas is present behind the casing, the resonance is not dampened and the wave will be reflected. Therefore, the tool indicates that there is no cement at the second interface. (Leigh et al. 1984, Nelson and Guillot 2006).
- Microannulus
  - The effect of microannulus is dependent on if it is filled with gas or water. The former will affect the response, while the latter will cause a small difference in the measurement (Nelson and Guillot 2006).
- Casing roughness
  - The rugosity of the casing affects the measurements, and can give higher results than in theory (Sheives et al. 1986).
- Sensitivity to density
  - Heavy density fluids
    - Higher attenuation in heavy density muds and oil based muds (Nelson and Guillot 2006).
  - Low density cement
    - Due to the method of investigation used by ultra-sonic tools, low-density cements has about the same response as water. Making differentiating between them difficult (Nelson and Guillot 2006).

Based on the limitations stated above for both sonic and ultra-sonic, we wish to investigate how light, photons, would perform in light of these limitations.

4 Fiber optics

In 1993, the first iteration of fiber optics for use in the oil industry was carried out, which consisted of a simple point pressure and temperature measurer. Since then, the industry has embraced the technology as a new way to provide continuous measurements along the entirety of the fiber optic cable. It has a distinct advantage over tools based on quartz technology as it can operate at higher temperatures (Johannessen, Drakeley, and Farhadiroushan 2012). Initial use of these tools was to monitor the reservoir, and assess injection and fracturing programs.

Parameters like temperature and strain can be measured by assessing the different sections of the returning data stream. The principles of the technology is unchanged, but we wish to use it for evaluating the cement in the annuli. Our interest does not lie in fiber optics for use in the reservoir section but above the production packer.

4.1 Sensing

As mentioned earlier, the first iteration measured the pressure and temperature at a single point, this method of sensing is named point sensor. Further development allowed for multiple point sensors along the cable, but there is no continuity between the sensors hence the name quasi-distributed sensor. The two former sensor placement methods use the fiber optic cable as a way to transmit the data from the sensors. Distributed sensing is to use the cable as measurements points along the entirety of the fiber cable (Li, Wang, and Tao 2015). The different configurations of sensors are shown in Figure 4-1. To initiate the measurement process, a surface tool sends a pulse laser through the cable. The laser is an infrared light beam with a wavelength just above the visible light spectrum. The parameters to be investigated are found by analyzing the backscattered pulse.

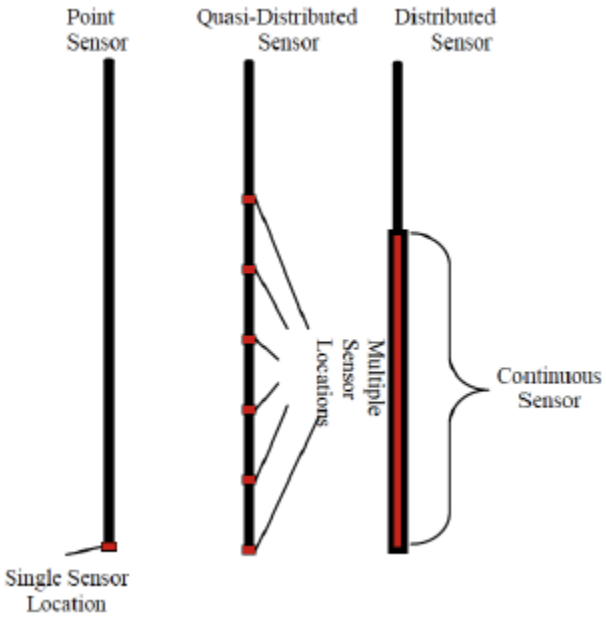

Figure 4-1- The three sensor configurations of fiber optics (Li, Wang, and Tao 2015)

A dynamic system is required to measure the conditions. One example is that of a temperature change caused by gas leakage. The method of investigation is a passive one, but requires activation from surface. The fiber optic cable itself is not proprietary to any company, as long as the parameters of the cable is known. The data processing is what separates each provider. This leaves the possibility of permanently installing the cable in the well and separate companies can use their surface tool to assess the well conditions. There are three different categories of deployment of a fiber cable in well (Li, Wang, and Tao 2015):

- Retrievable: The fiber is run into a well in a similar way as wireline tools
- Semi-Permanent: The fiber is run into a steel jacket installed outside production tubing
- Permanent: The fiber is installed behind the casing

The retrievable option is the cheapest method of deployment, but has the lowest data quality and requires more processing on surface. The cost and data quality increases with the more permanent deployment.

4.2 Principles

So far, we have discussed the sensor and fiber placement, now we will discuss how light travels inside the fiber and the different spectral bands present in the backscattered light.

There are two categories of fiber cables, which we will discuss, single and multimode. To understand how light travels through these types of cables we need to describe Snell's Law (Wikipedia 2017b). The formula describes the relationship of the angle of incidence and refraction, and it is given by the following relations:

$$\frac{\sin\theta_1}{\sin\theta_2} = \frac{v_1}{v_2} = \frac{\lambda_1}{\lambda_2} = \frac{n_2}{n_1} \qquad \textit{Eq. 4-1}$$

where θ_1 and θ_2 are the incident and refraction angles to the normal, v is the light phase velocity in a medium, λ is the wavelength and n is the refractive index. The refractive index describes the velocity of light in a material and is given by (Wikipedia 2017a):

$$n = \frac{c}{v} \qquad \textit{Eq. 4-2}$$

where c is the speed of light. In a vacuum the value of n = 1 and water n = 1.33, meaning that light travels 1.33 times as fast in water compared to in a vacuum. The refractive index for some materials is given in Table 4.1.

There is a critical angle which if exceeded will cause the light to not reflect and be dispersed in the material. To calculate the critical angle, where θ_2 is 90°, the following equation is used (Wikipedia 2017b):

$$\theta_{critical} = \arcsin\left(\frac{n_2}{n_1} \cdot \sin\theta_2\right) \qquad \textit{Eq. 4-3}$$

Table 4.1 - Refractive Index of materials (The Physics Classroom 2016)

Material	Refractive index
Vacuum	1
Air	1.0003
Water	1.333
Plexiglas	1.51
Crown Glass	1.52
Light Flint Glass	1.58
Dense Flint glass	1.66
Diamond	2.417

Figure 4-2 shows that the backscattered signal can be broken down to three spectral parts, Rayleigh, Brillouin and Raman. The latter two are inelastic scattering phenomena, meaning that there is a change in wavelength. While Rayleigh can be considered elastic meaning that there is little no reduction in energy. This can be seen in Figure 4-2, where the Rayleigh energy is equal to the incident energy. A more in-depth explanation will be given in the subchapters for the relevant tools. For now, how these spectral parts are found in the single- and multimode will be presented.

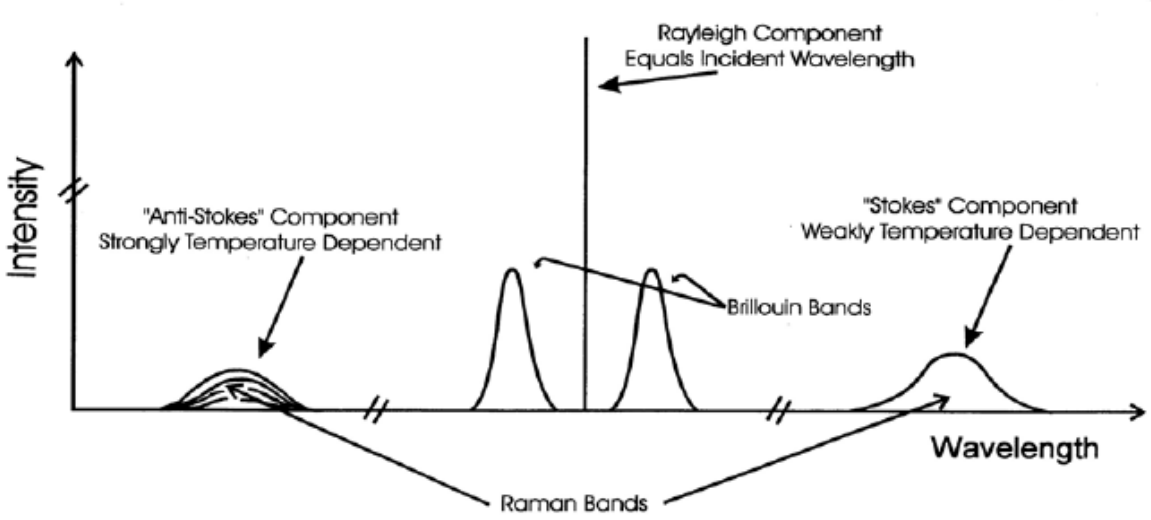

Figure 4-2 – The spectral parts of the infrared pulse. The Rayleigh band does not experience frequency change seen by the straight line. The Raman and Brillouin bands experience a change in wavelength.(Smolen and van der Spek 2003)

The similarities between single- and multimode is that they both have a glass core, cladding and require a protective shell, usually made of carbon, for use in harsh environments. The differences lies in the diameters of the three, with single mode having a core of 9 µm while multimode has a core of 50 µm. The cladding has a 0.5% lower refractive index than the core (Smolen and van der Spek 2003). This is to assure entrapment of the light pulse inside the core. Since the core of the multimode is larger than single mode, the critical angle is higher allowing the pulse to enter the fiber at an angle which allows for the emergence of multiple patterns, spectral parts, of movement inside the fiber, hence the name multimode. The patterns that can emerge in a multimode cable

depends on the profile of the refractive index. With a graded index, meaning that the refractive index gradually increases, a spiral pattern will emerge. A step index results in a zigzag pattern. With great difficulty, since the critical angle is small, it is possible to achieve multiple patterns in a single mode cable. One can consider that only one pattern emerges, which is the straight line but if the cable is bent, the light will reflect in the bend. The types of cables, refractive index profiles and patterns are shown in Figure 4-3.

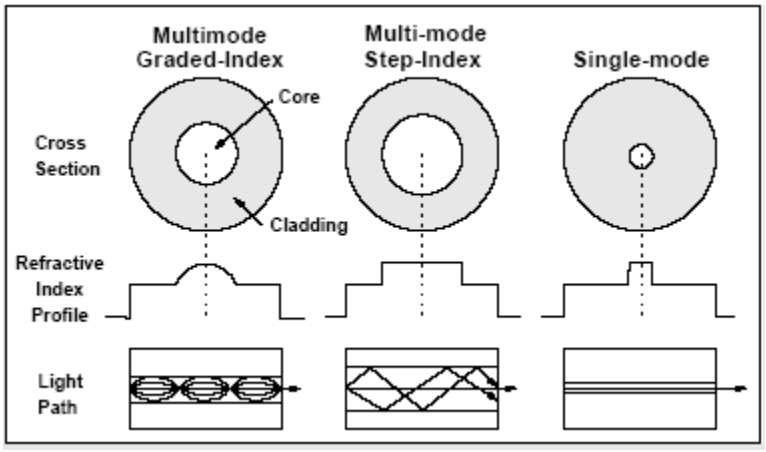

Figure 4-3 – Different types of fiber optic cables and the light path in these types (Infocellar)

If the refractive index of a fiber is known, usually between 1.5 - 1.7 as seen in Table 4.1 , the phase velocity is calculated by using Eq. 4-2 (Smolen and van der Spek 2003). If we use n = 1.5, then the phase velocity is:

$$v = \frac{c}{n} = \frac{(3 \cdot 10^8)}{1.5} = 2 \cdot 10^8 \frac{m}{s} \qquad \textit{Eq. 4-4}$$

Given the time of 10 ns, the length of the pulse in meters is given by the following equation:

$$L_{pulse} = v \cdot t = 2 \cdot 10^8 \cdot 1 \cdot 10^{-9} = 2\ m \qquad \textit{Eq. 4-5}$$

As the light travels through the cable, it needs to return hence the two-way travel time. If it travels a distance Z_L, it takes distance of $2 \cdot Z_L$ for the pulse to return to surface. To calculate the time required for the pulse to give us 1 m of vertical resolution, we use the following equation:

$$\Delta t = \frac{2\Delta Z_L}{v} = \frac{2 \cdot 1}{2 \cdot 10^8} = 10\ ns \qquad \textit{Eq. 4-6}$$

If the light pulse is 2 m, we can investigate the well in 1 m increments

$$t_{launch} = \frac{2 \cdot MSD}{v} = \frac{2 \cdot 3000}{2 \cdot 10^8} = 3 \cdot 10^{-5} s \qquad \textit{Eq. 4-7}$$

If we have a well that is 3000 m long, we can send a pulse 33 thousand times a second. This is just the theoretical maximum as time on surface is required to process the data, lowering the number of pulse launches between four and ten thousand. The reason for launching many pulses is due to weak acquisition from a single probe. To increase the resolution, the data from several probes is stacked and averaged to pronounce the anomalies. Resolution has a quadratic relationship with the number of samples acquired. Increasing the resolution by two would require four times the number of samples (Smolen and van der Spek 2003).

4.3 Distributed Acoustic Sensing

Acoustic sensing uses Rayleigh scattering of the photon beam to listen to flow in the annuli or seismic events that are generated in the formation. As the laser is traveling through the fiber, around 0.1% of the light is backscattered as it is refracted by the micro-heterogeneities in the cable (Boone et al. 2014). These uneven surfaces in the cable occurs naturally during fabrication of the cable. The result of this is that there are many points in the cable that will cause the light to be scattered. An analogy would be to have thousands of microphones listening to the well.

The principle of Rayleigh scattering is that a photon collides with a bound atomic electron, the electron absorbs the momentum energy but the energy is not sufficient to eject the electron from its shell or ionize it. The scattered photon exits the collision with a similar energy as the incident photon. This phenomena occurs when the incident photon carriers low energy and the atom has a high Z number (Podgorsak 2010).

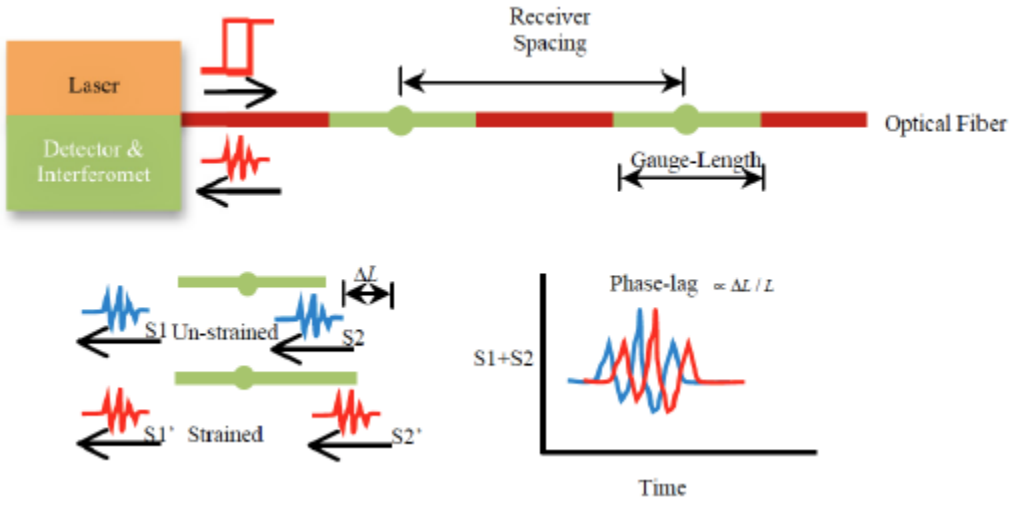

Figure 4-4 – Anomaly detection principle for DAS. Disturbance will cause a phase lag, which can be measured (Li, Wang, and Tao 2015)

Rayleigh is independent of temperature variations, eliminating an important variable that could affect measurements. Acoustic waves, caused by for example flow from a leak in the casing or cement, will collide with the backscattered wave that in turn will cause the wave to shift phase, seen in Figure 4-4. If the refraction index of the cable is known and we know that the speed of light is constant, one is able to calculate the point of origin of the anomaly. This is possible through several casing strings since acoustic waves can travel through casings at the cost of fidelity.

Length of the well is a limiting factor when using DAS, due to the two-way travel time it limits the sampling rate possible. One example is that a 1 km long well can use a 100-kHz sampling rate, as opposed to the 20-kHz possible for a 5 km well (Parker, Shatalin, and Farhadiroushan 2014). The sampling rate affects the resolution of the data, since measurements that are more frequent provide a finer image of the conditions. One should also mind the travel time, as sending another pulse before the preceding one has returned will cause interference between the signals. Furthermore, DAS is not able to discern the direction of the leak, as it investigates the circumference around the wellbore. Further reading on the advantages and disadvantages of DAS can be found in the following reference (Boone et al. 2014).

4.4 Distributed Temperature Sensing

We use the Raman spectral components to determine temperature changes in the well. This is due to the anti-Stokes component of the Raman band is sensitive to temperature, while the Stokes component is insensitive as seen in Figure 4-5. Anti-Stokes and stokes are shifted by $\Delta\lambda$, for example 40 nm to the left and right, another name for this phenomenon is blue and red shift. An example is if the Rayleigh band is 1000 nm, equal to the launched pulse, the anti-Stokes wavelength would be 960 nm while stokes would be 1040 nm. This change in wavelength changes the refractive index, thus the phase velocity (Smolen and van der Spek 2003). The consequence of this is that the position of anomaly detection is different and needs to be aligned, the tool on surface does the computation and realigns the returning signals.

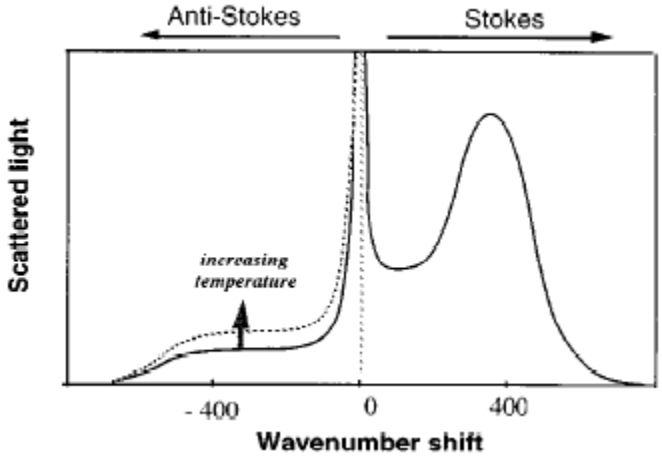

Figure 4-5 – Shift in wavenumber of the Raman bands and the temperature dependency of the Anti-Stokes component (Kersey 1996)

One method to calculate the change in temperature is given below, the derivation of the Equation 4-8 can be found in (Smolen and van der Spek 2003)

$$T(z) = T_{ref}\left(1 + \frac{\Delta\alpha Z}{ln\left(\frac{C_+}{C_-}\right)} + \frac{\ln\left(\frac{I_+(z)}{I_-(z)}\right)}{ln\left(\frac{C_+}{C_-}\right)}\right) \qquad \textit{Eq. 4-8}$$

C_- and C_+	Measured constants
I_- and I_+	Anti-Stokes and Stokes intensities respectively
$\Delta\alpha$	Difference in attenuation rates
Z	Distance
T	Temperature

Other methods calculate the temperature changes exists (Hausner et al. 2011, Oishi et al. 2014), some can give a reading with accuracy of ±0.2 °C under static conditions and ±1–2 °C during with rapid temperature changes.

One example of how a DTS log would look like is given in Figure 4-6 below, one should notice that the log also has a time component along the x-axis. This is an important advantage over conventional tools, as they can only provide a snapshot of the conditions and not the development of a situation.

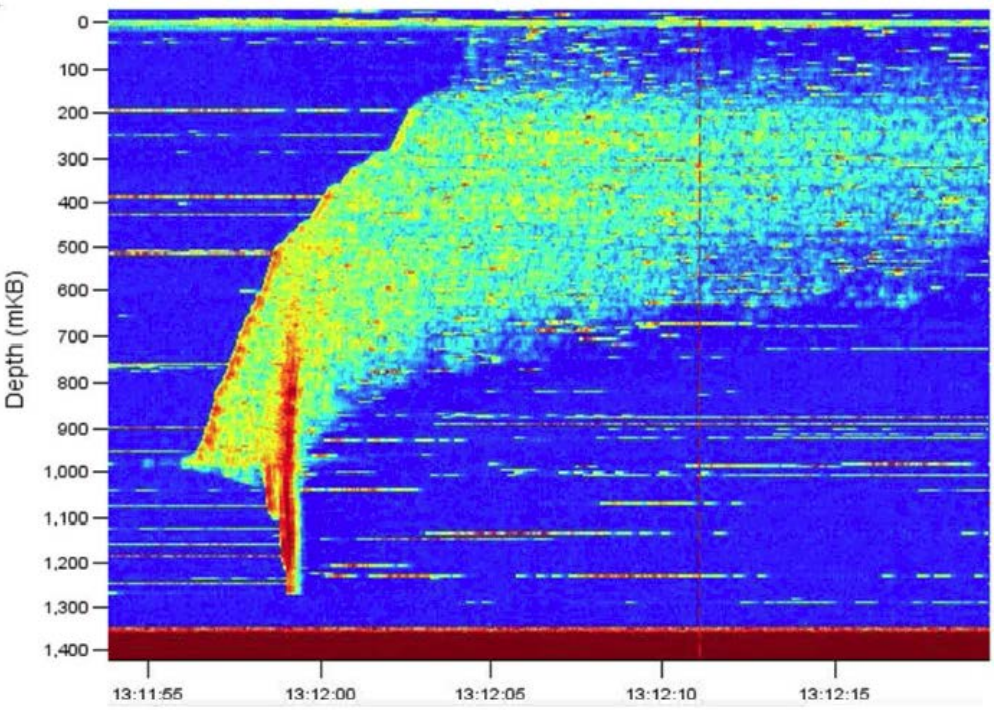

Figure 4-6 - DTS log, monitoring of a gas leak (Boone et al. 2014)

Primary cement, when placed will harden after sufficient time has passed. This hardening or hydration will generate heat. The amount of additives in the cement, often used to change the properties of cement, increases the temperatures generated. Contamination of the cement will cause the opposite effect, reducing the temperature expected (Wu et al. 2016).

In the following chapter, we will investigate a different application of photons than their use in fiber optics. We will move to an active method of investigation, where we will transmit photons to evaluate the barrier behind casing.

5 X-Ray

The following chapter will describe the principles of x-rays, and in the subsequent chapter, we will assess the ability of x-rays in cement evaluation.

5.1 What are X-Rays?

Wilhelm Conrad Röntgen discovered x-rays in 1895, while investigating the discharge of electrons in a tube that he covered up from the outside to prevent the light from escaping. Radiation from the tube passed through wood and paper, but metal objects left a shadow. His biggest finding was when he placed his hand in the radiation path and his bones were visible on the screen. The news of this discovery quickly spread and its implication in the field of medicine is felt today (Als-Nielsen and McMorrow 2001)

To understand what x-rays are and how they behave, we need to understand what light is. While the subject of quantum mechanics is outside the scope of this thesis, we can briefly state that it is the science of the behavior of particles in the atomic scale. It is the foundation of our understanding of how light functions, and it went through several revisions to reach what we know today (Harris and Freudenrich 2000). Light is both a wave and a particle, this duality allows for explanation that light travels through space as a wave but acts like a particle when interacting with matter (Kelkar 2013). The interaction of light with matter is a wide subject. We will cover some of the x-rays interactions in a later subchapter.

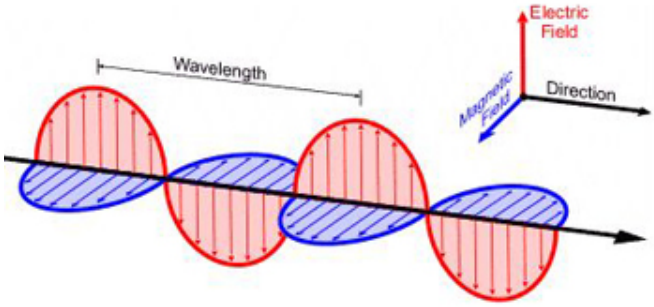

Figure 5-1 - Electromagnetic field traveling through space (National Weather Service)

As light is propagating through space, it is causing a disturbance in the electromagnetic field. The wave is the classical way of defining light propagation, Maxwell's equations describes the wave motion, shown in Figure 5-1, which is constituted of an electric and magnetic field that are always perpendicular to each other. Initially light was described as a wave, as it shared all the properties of a wave like interference, diffraction, reflection and refraction. The blackbody radiation spectrum could not be explained (Natarajan 2013). Imagine an ideal material that is able to absorb all light, hence the name blackbody, as well as emitting all light. Another term is thermal radiation, if for example heating a piece of iron will cause it to glow red and emit radiation, further application of heat will change the color of the iron indicating that it is emitting a different wavelength.

Signifying that light and energy are connected (ESA 2011). Based on this theory Max Plank implicitly proposed that the emitted radiation, or energy, from a material could be quantized by frequency seen by the Equation 5-1 below. Einstein would later explicitly present the idea of a light quantum, known as a photon. Meaning that the classical wave can be viewed from a quantum mechanical perspective as photons propagating in with individual energy and momentum (Als-Nielsen and McMorrow 2001). The wave-particle duality proposal by de Broglie was the final piece for the basis of our knowledge of light we have today (Natarajan 2013).

The Plank-Einstein relation describes how to determine the energy of a photon, which is given by:

$$E = h \cdot f = \frac{hc}{\lambda} \qquad \textit{Eq. 5-1}$$

Symbol	Denotes	Unit
E	Energy of photon	eV
f	Frequency	Hertz
h	Plank's Constant	J·s
c	Speed of light	m/s
λ	Wavelength	nm

The unit for energy of photon is electron volt, which is the charge of the electron multiplied with the potential differential voltage (Knoll 2010). The assumption that the speed of light is $c \sim 3 \cdot 10^8\ m/s$ is valid in a vacuum. Outside a vacuum, it will decrease depending on the matter refractive index n (Koks 2014), but we will assume that the speed is constant. With the former assumption, the energy carried by a photon and its place in the light spectrum is dependent on the frequency of the wave, which leads to an important outcome. That the difference between x-rays, radio waves and visible light is the frequency, and consequently the energy carried by the photon. We categorize the different energy levels in the electromagnetic spectrum, shown in Figure 5-2.

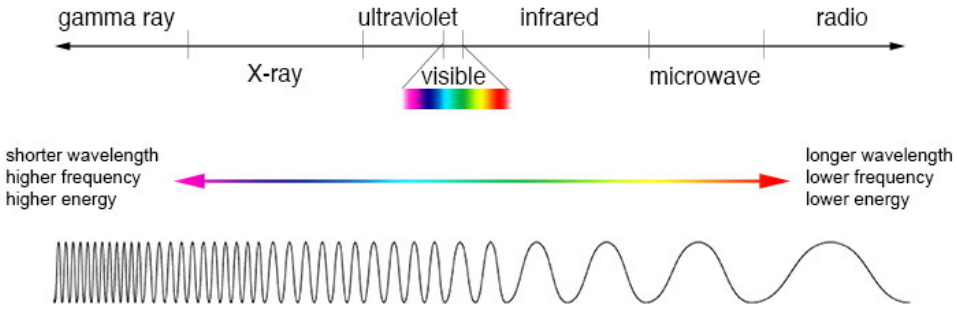

Figure 5-2 - The electromagnetic spectrum (NASA 2013)

Frequency is a function of velocity and the distance between the top of each wave. We measure the number of cycles the wave passes during a period. Knowing the frequency allows us to calculate the wavelength using the following equation.

$$f = \frac{1}{T_p} \qquad \textit{Eq. 5-2}$$

$$\lambda = \frac{c}{f} \qquad \textit{Eq. 5-3}$$

Shown in Eq. 5-3 the frequency and wavelength are inversely proportional to each other, meaning an increase of one results in a decrease of the other. The naked eye can only see the visible light spectrum in the range of 400 nm to 700 nm. Comparatively the weakest x-rays have a wavelength of 10 nm (NASA 2017). Sometimes wavelength is given in Angstrom, where $1\ \text{Å} = 0.1\ nm$.

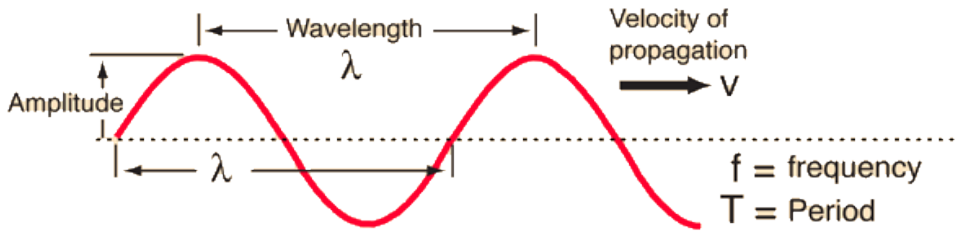

Figure 5-3 Variables of a wave (Nave 2016d)

As mentioned in the introduction, most uses of x-rays has been in the medical field, which uses soft x-rays meaning x-rays closer to ultraviolet energy levels. These rays do not carry enough energy to penetrate steel, which would require energies closer to gamma rays. High energy, or hard, x-rays are more interesting for our application of evaluating the cement. As it is comparable to gamma rays in its ability to penetrate materials (Cleland and Stichelbaut 2013). Generation of these soft and hard x-rays will be presented in the following subchapter.

5.2 Generation of Photons

Produced x-rays are divided into two groups. Bremsstrahlung, which is German for breaking radiation and characteristic x-rays, which is due to vacancies in the atomic shell (Knoll 2010). The photons relative intensity of the two groups can be seen in Figure 5-4, not that this is just an illustration as a change in target material will change the graph.

We will go more in detail with bremsstrahlung first. Intuitively from the name breaking radiation, one can assume it has do with the deceleration of the electrons as it collides with the target. A fraction of the energy carried by the accelerated electrons are converted to photons. Increasing the acceleration of the electron, adding more energy, will increase the energy of the photons generated. A monoenergetic, a single energy level, beam of electrons would produce a spectrum of photon energies with the highest energy level equal to the electron energy level (Knoll 2010).

Characteristic x-rays occur when the collision occurs and a vacancy is created in the K shell of an atom in the target. Electrons have the tendency to rearrange themselves to the lowest energy level. When another electron from higher shells, L and M, fills the vacancy k_α and k_β photons are

produced, respectively. These photons can be used in elemental analysis since the characteristic x-rays are unique to each element (Knoll 2010).

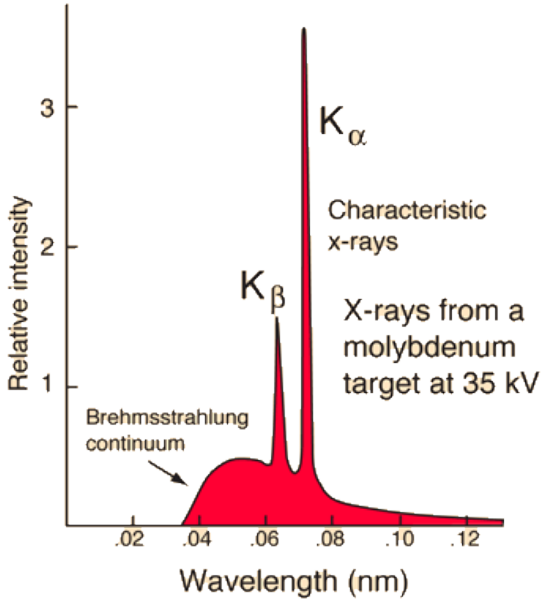

Figure 5-4 - Example of Brehmstrahlung continuum and Characteristic x-rays (Nave 2016b)

5.2.1 X-ray tube

The conventional way of generating x-rays is by accelerating electron emitted from a cathode with sufficient energy towards an anode. The subsequent collision will emit x-rays. The method used by Röntgen in his discovery of x-rays proved not to be a reliable way of generation. Two designs of x-ray tubes are shown in Figure 5-5. In 1912, W.D. Coolidge devised the design on the left, which allowed for controlling the voltage and amperage. This method is limited by the ability to cool the anode. Only marginal improvements had been done on the initial design until a rotating anode was introduced in 1960, shown on the left in Figure 5-5. The rotating design allowed for greater heat dissipation and conversely greater x-ray energies (Als-Nielsen and McMorrow 2001).

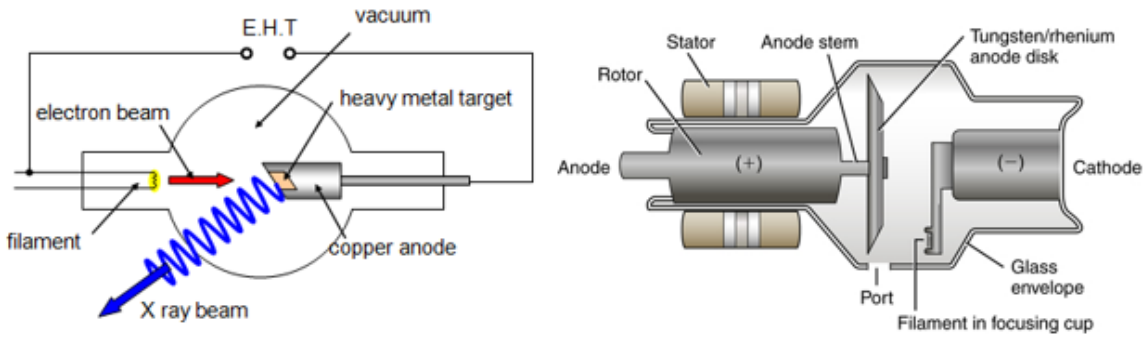

Figure 5-5 - Coolidge Tube (left)(Gibbs 2013) and Rotating Anode (right)(Radiologykey 2016)

The filament, or cathode, is a metal wire that when heat is applied will emit electrons. Furthermore, the electrons are released in all directions, focusing the beam requires the cathode to be placed within a "focusing cup" that aims the electrons at the target. The tube envelope can be made of glass or metal with ceramic disks at each end, use of metal allows for a more durable tube able to withstand thermal and mechanical shocks. The reason for the envelope is due to the inherent need of a vacuum so that the electrons do not collide with air molecules leading to reduction in energy. The anode is the target, a heavy metal such as tungsten or tantalum (Cleland and Stichelbaut 2013). The reason for the use of tungsten and other heavy metals is as following (Technical Manual 2016):

- High atomic number: Higher atomic number, i.e. larger nuclei, results in better x-ray production efficiency since electrons have a larger target
- High melting point: As the electron collides with the target, heat is generated and the use of metals with higher melting point increases durability
- High thermal conductivity: Dissipation of heat increases durability
- Low vapor pressure: Material is resistant to vaporization after collision

The heat generation is one of the major limitations of an x-ray tube. Most of the electrical power is not converted to x-rays. With soft x-rays in the 30 keV range 0.05 percent and 10 percent in the MeV range is converted into x-rays, increasing the voltage not only increases the penetrative capability of the x-ray but also the efficiency of the source. Amperage controls the quantity of electrons directed at the target and is independent of voltage (Technical Manual 2016). Another way to look at it is that of a faucet, at low amperage a trickle of electrons pours out while at high amperage a steady stream of electrons. The intensity of photons is related to the number of photons in a beam per unit area. Keeping the energy of the photons constant and doubling the number of photons will double the intensity.

Mentioned earlier is that the energy of a photon is given by the unit electron volt. Calculating produced photon energy by an x-ray tube is as following:

$$E_{electron} = q \cdot \Delta V \qquad \textit{Eq. 5-4}$$

We have that $q = 1\,electron$ and ΔV is the differential voltage, in other words the additional energy used to accelerate on electron. The maximum energy a photon can have is the maximum produced by the electron, in the Bremsstrahlung spectra (van Biezen 2013)

$$E_{photon\,maximum} = E_{electron\,maximum} \qquad \textit{Eq. 5-5}$$

5.2.2 Radioisotopes

Radioactive isotopes produce gamma rays and x-rays as they decay. One can produce isotopes with varying half-lives and emission energies, and the cost of production is low. The disadvantages compared to tube emitted x-rays is that they cannot be turned off posing a health, safety and environment issue (HSE). Determining the optimum half-life also needs to be considered as producing an isotope with a too long half-life presents difficulties in safe disposal, while too short half-life means replacing the isotope often (Geuther 2007).

$$ {}^{A}_{Z}X \rightarrow {}_{Z+1}{}^{A}Y + \beta^{-} + \overline{\upsilon} $$

The process above describes beta decay, which is a source of fast electrons. X and Y is the states before and after for a nucleus, β^{-} the beta particle and $\overline{\upsilon}$ is the antineutrino. The decay energy is fixed and is shared between the beta particle and the antineutrino, resulting in variations in the energy of the beta particle. The decay particle can eject an electron from its shell, and the filling of the vacancy creates characteristic x-rays and auger electrons. The latter is explained further in chapter 5.5.4. This process is called internal conversion. The nuclear energy is transferred to the electron and the resulting energy of the electron is described by the following equation (Knoll 2010):

$$ E_{e-} = E_{ex} - E_{b} \qquad \textit{Eq. 5-6} $$

E_{e-}	Conversion Electron
E_{ex}	Excitation energy
E_{B}	Binding energy

Internal conversion competes with gamma-ray de-excitation, and if the energies are high enough some bremsstrahlung can be detected. An x-ray source free of gamma-rays is possible but the produced x-rays are much weaker, in the range of 5 keV. This is opposed to 662 keV gamma rays found in a ${}^{137}_{55}CS$ source (Knoll 2010).

5.2.3 Pyroelectric Crystals

Pyroelectric crystals can be used to generate x-rays. These crystals are at equilibrium polarized, meaning that if the crystal is cut at the axis of polarization, one side will have a positive charge and the other negative. The charge of the surfaces in a vacuum is known as spontaneous polarization, P_s. Temperature changes will affect the potential charge of the crystals, and the surface charge can be calculated by using the following formula (Geuther 2007).

$$ \sigma = \gamma \cdot \Delta T \qquad \textit{Eq. 5-7} $$

σ	Surface charge
γ	Pyroelectric coefficient
ΔT	Temperature change

Increasing the temperature of the crystals would in turn increase the electric potential. The limit is the Curie temperature, which is the temperature where the properties of the crystal will change and it will lose its use of pyroelectricity. This limit can be ignored in most cases if certain crystals are used. Lithium niobate [$LiNbO_3$] has a curie temperature of 1200 °C and lithium tantalate [$LiTaO_3$] has Curie temperatures of 620 °C.

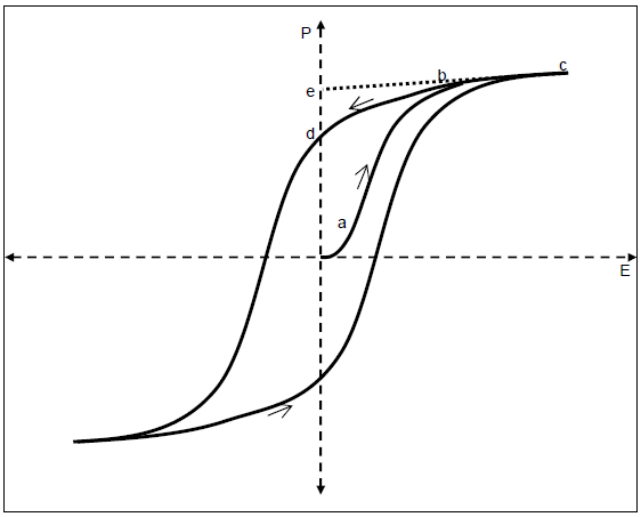

Figure 5-6 - Ferroelectric hysteresis loop showing the polarization and electric field relation (Geuther 2007)

Figure 5-6 shows the polarization changes caused by temperature change and the following electric fields generated. A virgin crystal would follow path (a) to (b) as its polarization increases, once the crystal is saturated, it is at point (c). Removing the external field would not return the crystal to its origin point 0, but to point (d) which is called the remnant polarization.

The results from experiments done by (Geuther 2007) shows that this method can produce x-rays with an energy level of 200 keV, if two crystals are used in combination. The limitations of this method are that the production is temperature and time dependent. As the x-ray yields from the crystal, goes from zero to maximum during the temperature cycles, which can span over several minutes.

5.3 Heat Generation and its Effects

An object subjected to higher temperatures, will have its thermal energy increased. Heat transfer describes the movement of thermal energy in a body or between two bodies. Heat will always try to reach equilibrium, meaning that heat will transfer from a hot body to a cold body naturally.

Thermal energy and temperature is not equal, as temperature is a measurement of the average kinetic energy of the particles while thermal energy is the total kinetic energy of all particles. There are three types of heat transfer, and these can occur alone or in conjunction with each other (Tada 2002).

- Conduction
    - Transfer of heat between solids and stationary fluids. Imagine a grid of particles, as temperature increases on one side the particles on that side will start to vibrate. The vibration will cause the particles to move and collide with the colder particles. During this collision heat is transferred, and the process is repeated until the entirety of the grid reaches equilibrium.

- Convection
  - Transfer of heat by the way of moving fluids. Imagine a hot surface that heats up the surrounding air. The warm air travels upwards due to wind and is replaced with colder air which starts to warm. The warm air cools as it travels upwards and begins to travel down to the hot surface warming it up again. The circulation process has begun and is then repeated.
- Radiation
  - Transfer of heat occurs when emitted radiation, photons, are absorbed by the target matter. As an incident radiation beam hits a surface, some of the beam is either reflected, refracted or absorbed. The latter is what transfers heat. An important aspect of radiation transfer of heat is that it does not require contact of matter for the transfer to occur, as photons can travel through space.

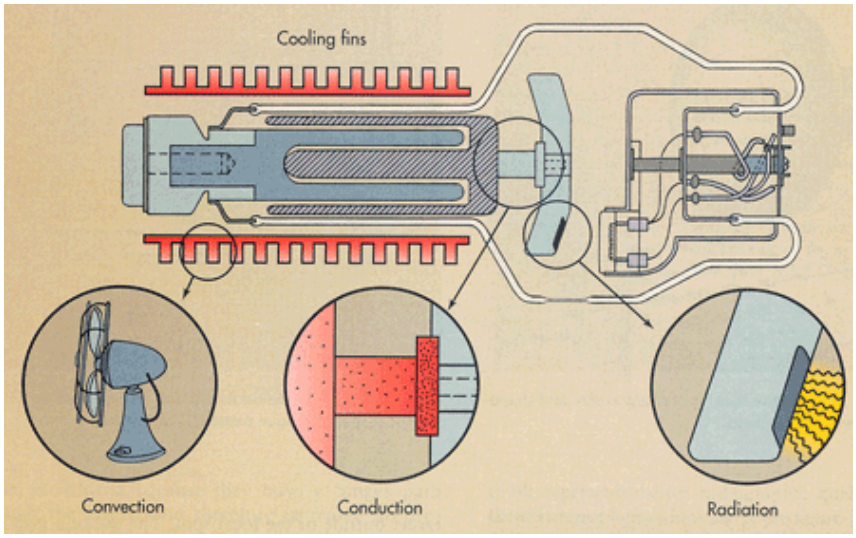

Figure 5-7 - Methods of heat transfer in an X-ray tube (Wenatchee)

All three of these methods of heat transfer are relevant to the X-ray tube, as seen in Figure 5-7. Since transfer of heat occurs inside the tube due to radiation and conduction. Convection occurs if the fluid surrounding the tool in the wellbore is dynamic. Modelling of the temperature generated and dissipation of heat inside the wellbore by a proposed tool is outside the scope of this thesis.

Generation of x-rays in an x-ray tube is an inefficient process, as almost 99% of the electrons are converted to thermal energy. Calculation of the heat generated at the anode when producing x-rays is given by the following equation (Wenatchee):

$$HU = kVp \cdot mA \cdot exposure\ time \cdot generator\ constant \qquad \textit{Eq. 5-8}$$

The measurement of heating is given by heating units (HU), but is actually Joule (J). We have mentioned the effects of voltage and amperage on generation earlier but we will review it again in addition to exposure time and the equation constant (Serman 2001).

- Voltage
    - Voltage affects the energy of the electron as it is accelerated towards the anode. Increasing the potential difference between the cathode and anode results in greater mean and maximal photon energy.
- Amperage
    - Amperage affects the number of electrons accelerated towards the anode. Thus, there is a linear relationship between amperage and radiation produced.
- Exposure time
    - Affects the duration of which photons are produced. Similarly, to amperage it controls the amount of radiation produced.
- Generator Constant
    - Affected by the generator type, and the voltage pulses it creates. If the machine is a single phase then it is equal to 1, consequently if its high-frequency then it is 1.45. In a single-phase generator, the voltage has to reach zero before increasing voltage again, high frequency on the other hand increases and lowers voltage more frequently while still maintaining a higher minimum voltage (Hill's X-Ray Services 2017).

To convert HU into degrees Celsius, we need to use specific heat. It is the amount of heat units required to increase the mass of a body by certain amount of degrees Celsius. Given by the following equation (Nave 2016c):

$$Q = c_s m \Delta T \qquad \textit{Eq. 5-9}$$

$$T_{final} = \frac{Q}{c_s m} + T_{initial} \qquad \textit{Eq. 5-10}$$

Q	Heat added	Joule
c_s	Specific heat	joule/gm°C
m	Mass	g
ΔT	Change in temperature	° C

Given the equations above it is possible to do a simplified calculation of the heat generated by the tool in degrees, but in fact one would need to account for the methods of heat transfer, the dynamic movements of fluids and the materials of the tool and encountered in the well.

H. S. Read (Read 1926) investigated the effects of temperature on x-ray absorption of different wavelengths, i.e. different energy levels. Initially one thought that the absorption of photons was independent of temperature. The elevated temperatures used in the experiment, which involved heating nickel to between 700°C and 1000°C, resulted in small change in attenuation rate. These temperatures are much greater than expected temperatures inside a wellbore.

Research done by Chen and Cheng (Chen and Cheng 2013) concluded that it is possible to determine temperature in materials by measuring x-ray transmission. They stated that the method is an improvement over other methods like fiber optics and infrared due to the inability of the

former methods to penetrate the surface layer, only measuring the surface temperature of an object. The x-ray method utilizes measurement of changes in density in a material due to thermal expansion to infer the temperatures that caused the change. The results between the actual and calculated values correlated with some error percentage.

5.4 Detection

The investigation of matter with x-rays requires both generation and measurement of the rays. This chapter will cover how we can detect photons, amplify and convert them into usable data. Measurements of photons can be done using a combination of a scintillator and a photomultiplier (PMT). This coupling can take a photon, converts it to an electron and amplifies one electron to millions of electrons. Shown in Figure 5-8 is a schematic of a possible setup of the coupling of a scintillator and a PMT. Any ray that can ionize can replace the gamma ray in the Figure 5-8, which is to excite an electron so that it will vacate its shell. We will discuss each part separately, as different processes take place in each component.

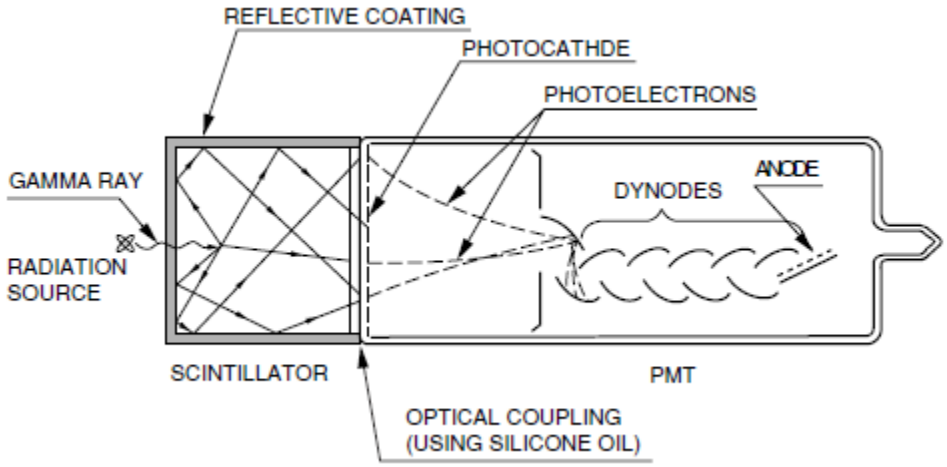

Figure 5-8 - A scintillator and photomultiplier setup (Hamamatsu Photonics 2007)

5.4.1 Scintillator

Scintillation detection of ionizing radiation is not a new technique, but the method is has stayed appropriate as it is one of the more suitable methods. A simplified view of the process is that ionizing radiation hits the scintillator, which in turn produce a flash of light that can be measured. The ideal scintillator material should have the following properties (Knoll 2010):

- High efficiency conversion of kinetic energy to detectable light
- Linearity in conversion as the deposited kinetic energy should be proportional to the light generation
- The material is transparent to its own emission of light
- Short time for electrons to decay to their original state as it allows for higher pulse detection
- Production of the material should be of good optical quality and size variation
- The refraction of the material should be close to glass to increase efficiency of the system

As with most ideal things in theory, they do not exist in reality. Thus, comprise between the six factors above must be made. There are mainly two types of scintillator materials, inorganic and organic. The scintillation mechanism between the types are different, which in turn results in different qualities.

Organic scintillators

Organic scintillators can be (Hamamatsu Photonics 2007):

- Plastics
- Liquids
- Anthracene of organic crystal

The scintillation mechanism is due to the elevation of a single molecule, making the organic scintillator less sensitive to its physical state.

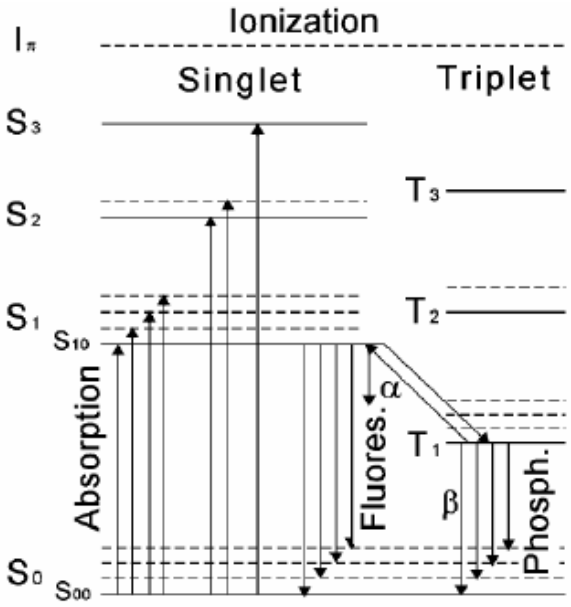

Figure 5-9- Energy levels of organic molecules (Knoll 2010)

At room temperature, the energy state is at S_0 seen in Figure 5-9. When kinetic energy is absorbed, the electrons become excited and move up to S_1 and above. Electrons that are sufficiently excited to level S_2 and above will have its energy decay quickly and consequently fall down to S_1 through internal conversion. Fluorescent light is produced when the electron return from S_1 to their initial state S_0. The intensity of the light produced is described by the following equation:

$$I = I_0 e^{-t/\tau} \qquad \textit{Eq. 5-11}$$

Where I and I_0 are the intensities, t is the time and τ is the decay time. For organic scintillators the decay time is in the nanosecond scale, making them very responsive (Knoll 2010). Phosphorescence, which is light that is not immediately emitted, occurs when electron returns from T_1 to S_0. As the wavelength and time is different from fluorescent light one can discriminate against

phosphorescence. Since the emissions between the levels above S_1 is smaller than the minimum absorption means that the emitted light will appear transparent to the material passing through it.

Some properties of organic scintillators are (Hamamatsu Photonics 2007):

- Fast response time due to short decay time
- No issues with temperature
- Easy to cut and shape
- Low absorption coefficient
- Lower probability for photoelectric effect

The photoelectric effect will be discussed in a later chapter 5.5.4. More in-depth explanation of scintillation mechanisms and organic scintillator types can be found in (Knoll 2010). The two latter points is why inorganic scintillators are more commonly used for energy analysis.

Inorganic scintillators

This type of scintillators are often halogen compounds like NaI (TI), sodium iodide with parts thallium. The mechanism for inorganic differs from organic as the crystal lattice is important. The energy or band gap between the valence band and the conduction band is a space that electrons cannot occupy, shown in Figure 5-10. An insulator would have a larger band cap, while a semiconductor and a conductor has increasingly smaller band gap. In a pure or ideal crystal, the energy required to excite an electron from the valence band to the conduction band is such that it would result in emission of photons with wavelengths shorter than the visible light range. To remedy this problem one introduces impurities in the crystal. In the case of a NaI crystal, TI is added. The addition of impurities modifies the band gap in a way that electrons can occupy positions in the gap. The impurities are called activators, and there are three types of activation centers (Knoll 2010).

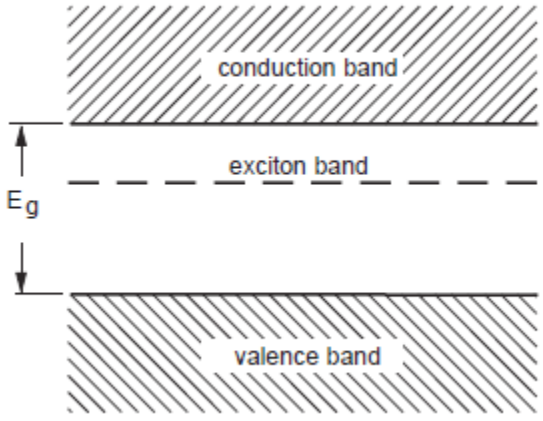

Figure 5-10 - Energy band diagram in an ideal crystals (Flyckt and Marmonier 2002)

- Luminescence or recombination centers
    - The electron-hole pair in the band gap allows electrons to excite or de-excite without traveling the whole length of the band cap. Resulting in fluorescence emissions with longer wavelengths.

- Quenching centers
    - Similar to the centers above, but here the excitation results in heat instead of light. This results in a loss in conversion from kinetic energy to scintillation light.
- Traps
    - These levels are stable, meaning that the electron will not decay as rapidly and will not move until sufficient thermal energy is acquired before moving towards the conduction band or valence band. The delayed movement of the electron will result in phosphorescence light.

Some properties of inorganic scintillators are (Hamamatsu Photonics 2007):

- Excellent energy conversion efficiency
- High absorption efficiency
- Good probability for photoelectric effect
- Prone to melting
- Vulnerable to shock and impact

5.4.2 Photomultiplier

As the scintillator converts ionizing radiation to low energy photons, the PMT converts these photons into electrons and amplify them.

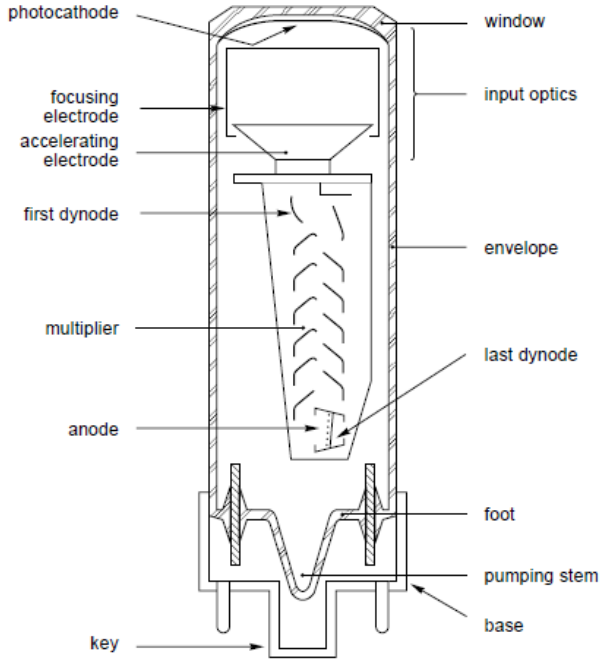

Figure 5-11 - Photomultiplier components (Flyckt and Marmonier 2002)

Figure 5-11 displays the components of the PMT, some we will describe in detail. The photocathode converts the photons gathered from the scintillator into electrons. The process is similar to what has been described in the inorganic scintillator section, as both are semiconductors. The difference is that we want the electrons to escape into vacuum, converting electron into

photoelectrons. There are two types of photocathodes (Flyckt and Marmonier 2002, Hamamatsu Photonics 2007):

- Semi-transparent cathodes
  - The electrons are deposited opposite of the incident photons. Allows for a large window and can be either flat or curved. Seen in Figure 5-11. Known as transmission mode.
- Opaque cathodes
  - The electrons are deposited on a metal electrode inside the tube, and the electrons are deposited on the same side as the incident photons. Limited size due to the focusing of the electrons. Known as reflection mode.

The quantum efficiency describes the efficiency of the photocathode to convert incident photons to electrons. It is given by following equation (Hamamatsu Photonics 2007):

$$\eta(f) = (1 - R) \cdot \frac{P_V}{k} \cdot \left(\frac{1}{1 + {}^{1}/_{kL}} \right) \cdot P_s \qquad \textit{Eq. 5-12}$$

η	Quantum efficiency
R	Reflection coefficient
k	Full absorption coefficient of photons
P_V	Probability that light absorption may excite electrons to a level greater than vacuum level
L	Mean escape length of excited electrons
P_s	Probability that electrons reaching the photocathode surface may be released into the vacuum
f	Frequency of light

The type of photocathode governs the parameters R, k and P_v above, and the efficiency of the photocathode is a function of the incident photons and the average is around 15 – 30% (Knoll 2010).

The focusing electrode gathers the deposited electrons from the photocathode and directs them towards the first dynode. The collection efficiency is usually greater than 80% (Flyckt and Marmonier 2002). The dynodes is what amplifies the number of electron from a few to the order of millions (Hamamatsu Photonics 2007), the dynodes are of materials that easily emits electrons. They are placed such that the electric fields accelerates the electron so that the collision with the next dynode emits additional electrons, continuing the process is why electron gain goes from one single electron to millions. All dynodes are identical except for the first and last one, and there are various shapes and structures of the dynode field. The anode at the end of the dynode field collects the electrons so they can be used an electrical signal.

PMTs for use in the oil industry require some special considerations, as the environment they will encounter is much harsher than what is found in the lab. To remedy the susceptibility of vibration and shock, ruggedized PMT versions have been designed. The basis of the design is similar to the

one described earlier, but weak points of the system have been reinforced shown in Figure 5-12 (Hamamatsu Photonics 2007).

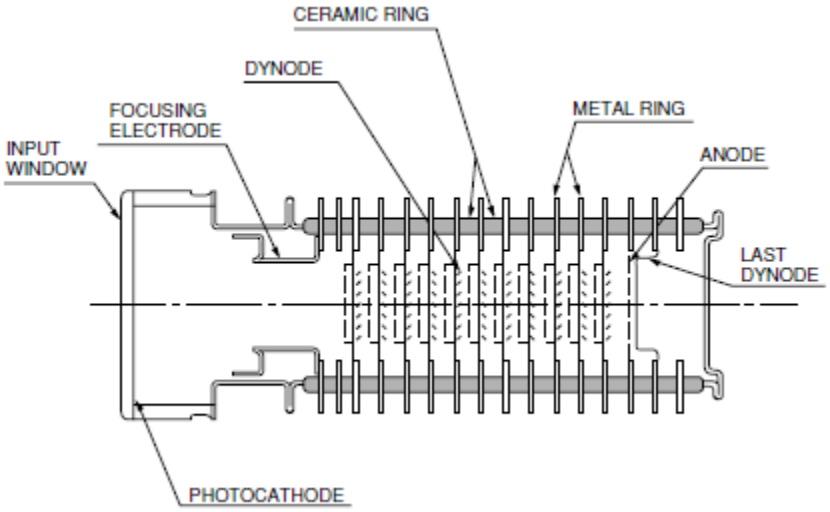

Figure 5-12 - Ruggedized PMT (Hamamatsu Photonics 2007)

Temperature is an issue as the capability of most photocathodes are severely degraded if temperatures exceed 80° - 100 °C (Flyckt and Marmonier 2002). One bialkali metal, a combination of two alkali metals, increases the operational temperature to 175 °C (Hamamatsu Photonics 2007).

This was a brief overview of scintillators and photomultipliers, I recommend the Hamamatsu Handbook found in reference (Hamamatsu Photonics 2007) for a more in-depth view concerning principals, materials and design.

5.5 Photon interactions

Photons interact with matter in a two-step process (Podgorsak 2010):

1. Step-energy is transferred to an energetic light charged particle (electron or positron)
2. Energy is deposited in the absorbing medium by the charge particle

The interaction of photons is dependent on the energy level of the photon itself and the atomic number of the target. It can either occur with the whole atom, the nucleus or an orbital electron. Once the collision occurs, the outcomes are confined to two possibilities. The affected particle will either absorb the photon completely or scatter the photon. Likewise, the type of absorption or scattering interaction is dependent on the energy level and the atomic number. If the target is an orbital electron, the interaction is divided into two groups, depending on if the electron is loosely or tightly bound.

If the photon energy is magnitudes larger than the binding energy of the electron then the following interactions can occur, $Photon\ Energy \gg E_B$:

- Thomson scattering
- Compton scattering
- Pair Production

Conversely, if the photon energy is slightly larger or equal to the binding energy the following interactions can occur, $Photon\ Energy \geq E_B$:

- Photoelectric effect
- Rayleigh Scattering

Rayleigh scattering has been previously explained in chapter 4.3. Pair production occurs if the incident photon energy possesses energy above 1 MeV. Generating these energy levels requires large facilities that can house synchrotrons. Thomson scattering on the other hand is an elastic scattering phenomena, in which the incident photon does not transfer energy to the electron. The consequence of this is that the wavelength of the incident and scattered photons are approximately equal. This interaction will occur at low energy levels, levels that are not sufficient to penetrate the casing. Pair production and Thomson scattering will not be discussed in depth due to them being irrelevant to our application. In essence it is minimum limit of Compton scattering, this will be shown later. If there is further interest in these two interactions, more information can be found in following books (Attix 2007, Podgorsak 2010).

Figure 5-13 shows the relationship between the photon energy, the atomic number of the target and the dominating interaction that will occur during a collision. We will discuss photoelectric and Compton effects in more detail in chapters 5.5.3 and 5.5.4.

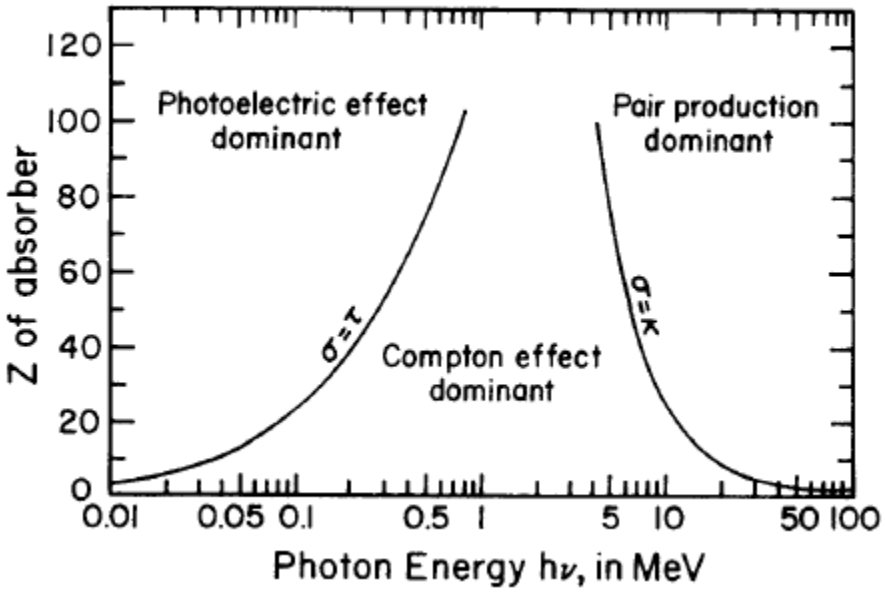

Figure 5-13 - Dominating interaction as a function of atomic number and photon energy (Attix 2007)

5.5.1 Attenuation

Once the collision occurs, the energy carried by the photon can result in a transfer or no transfer of energy. If there is no transfer of energy, then the photon will exit the collision with the same energy as before the incident. When a transfer of energy occurs, the energy of the photon is reduced after the collision and the difference in energy before and after the collision will be transferred to the electron. The attenuation of the beam is shown in Figure 5-14.

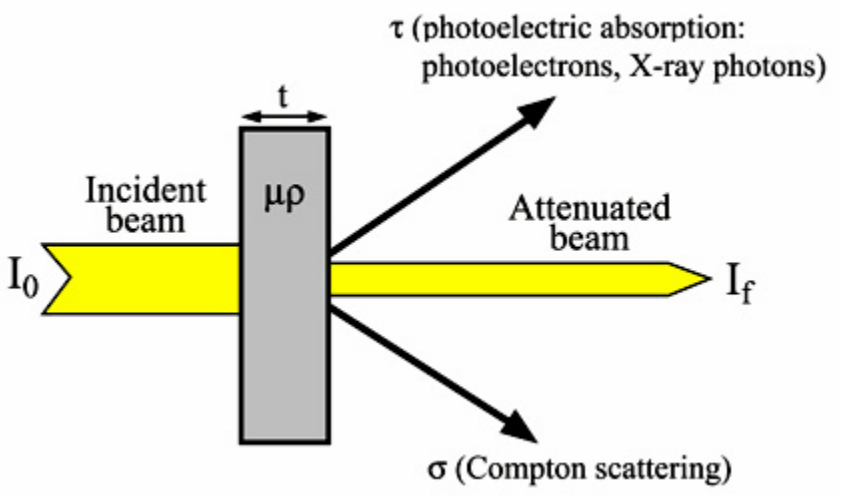

Figure 5-14 - Attenuation of an x-ray beam as it passes through a sample (Wittke 2016)

The parameter μ, linear attenuation coefficient, describes the probability of the number of interactions that will occur as a photon travels through a medium. μ itself is a function of the photon energy and the atomic number Z of the medium, which the beam travels through. It can also be given as the mass attenuation coefficient, which is the linear attenuation divided by the density, μ/ρ.

Determination of this parameter can be done through a narrow beam experiment. Monoenergetic, single energy level, photons are sent from a source towards a detector, both are collimated which means that the photons travel in parallel. The material under investigation is placed between the source and detector, which will decrease the intensity, i.e. the number of photons, reaching the detector. If we use I as a symbol for intensity, then I_0 is the intensity as it leaves the source and I_x is the intensity after it passes through the material and reaches the detector. To describe the thickness of the material we use dx' and it will reduce dI if dx' increases. Since the relation $-dI/I$ is proportional to the attenuation coefficient and the thickness dx' we can express this relation (Podgorsak 2010).

$$-\frac{dI}{I} = \mu dx'$$

$$\int_{I_0}^{I_x} -\frac{dI}{I} = \int_{0}^{x} \mu dx'$$

$$\ln \frac{I_x}{I_0} = -\mu x$$

$$I_x = I_0 e^{-\mu x} \qquad \textit{Eq. 5-13}$$

With this equation, known as Lambert's law (Wittke 2016), we can calculate the attenuation of the incident beam after passing through a material. Yet there are some limitations as this equation assumes that the linear attenuation coefficient is constant and no scattering or secondary radiation is present. If the latter is present, it is not taken into account when calculating I_x.

5.5.2 Differential Cross Section

The trajectory of a particle is not possible to ascertain (Corni et al.), but it is possible to know if a particle has been scattered. We will describe the idea behind differential cross section, but the derivation of the formulas is outside the scope of this paper. If there is interest in knowing more about this subject, it can be found in the following books. (Als-Nielsen and McMorrow 2001, Podgorsak 2010)

Imagine a source emitting x-rays, I_0, at a target which has N number of particles per unit area. The scattered photons, I_{sc}, will do so at a solid angle $\Delta\Omega$. I_{sc} is proportional to all the parameters mentioned above. It also depends on the efficiency of the sample to scatter the photons, which is given by the differential cross section ($\frac{d\sigma}{d\Omega}$), another way to look at this parameter is that it is the probability for the scattering phenomena to occur (Als-Nielsen and McMorrow 2001).

$$I_{sc} = I_o N \Delta\Omega (\frac{d\sigma}{d\Omega}) \qquad \textit{Eq. 5-14}$$

$$\left(\frac{d\sigma}{d\Omega}\right) = \frac{Number\ of\ photons\ scatter\ per\ second\ into\ \Delta\Omega}{I_o N \Delta\Omega}$$

5.5.3 Compton Scattering

Compton scattering is incoherent, meaning that the result of the interaction between the photon and particle results is that the scattered photon has less energy than the incident photon. The latter photon beam will eject an electron with a kinetic energy E_K, the ejected electron is named the recoil electron. Figure 5-15 shows the angle θ, this is the symbol for the scattering angle, which is defined as the angle between the incident and scattered photons. It can range from 0 to 180 degrees, with 0 degrees being that the scattered photon continues to travel in the same direction as the incident photon. The recoil electron angle ϕ is defined as the angle between the incident photon and the recoil electron and can range from zero to 90 degrees. Subsequent figures will use the symbol v for the frequency, we will continue using f as the symbol for frequency in the text.

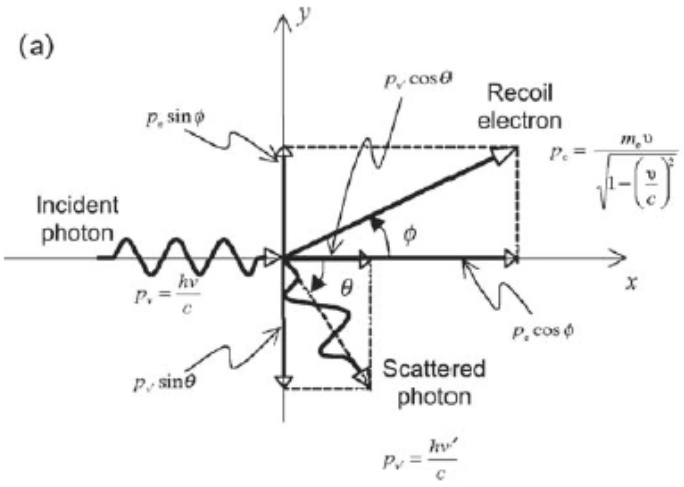

Figure 5-15 – Decomposition of momentum during Compton scattering (Podgorsak 2010)

This interaction is of interest, as it is the basis for why both transmitter and detector can be on the same side. We are not limited to the true backscattering angle of 180 degrees. Depending on the angle of transmission from the source and the distance of the detector in relation to the source, we can reduce the angle to reduce the attenuation that comes with increasing θ (Podgorsak 2010).

Our focus will be on the scattered photon, but we will briefly discuss the recoil electron. One does not usually measure what occurs with the recoil electron, but is possible to determine the density of a material by using the transferred momentum to the recoil electron. The momentum of the recoil electron is related to the angle, but the method requires vacuum for measuring the electron as air can interfere with the path of electrons (Cooper 1997). It is also considered when designing the PMT, as one wishes to have the highest collection rate of electrons possible. We will continue with how to determine the angles θ and ϕ depending on the incident beam.

Using Figure 5-15, we will begin by deconstructing the forces of the recoil electron and the scattered photon into x and y coordinates. Notice that there must be conservation of momentum.

$$x: P_v = P_v' cos\theta + P_e cos\phi$$

$$y: P_e sin\phi = P_v' sin\theta$$

where P_e and P_v' are the momentums for the recoil electron and scattered photon, respectively. The derivation of the relation is as follows (Podgorsak 2010):

$$P_e = P_v' \frac{sin\theta}{sin\phi}$$

$$P_v = P_v' cos\theta + P_v' \frac{sin\theta}{sin\phi} cos\phi$$

$$P_v = P_v' cos\theta + P_v' sin\theta cot\phi$$

$$\frac{P_v}{P_v'} = cos\theta + sin\theta cot\phi \qquad \textit{Eq. 5-15}$$

we have also the following relation

$$\frac{P_v}{P_v'} = \frac{hf/c}{hf'/c} = 1 + \varepsilon(1 - cos\theta) \qquad \textit{Eq. 5-16}$$

equating Eq. 5-15 and Eq. 5-16, we get the following result (Podgorsak 2010):

$$1 + \varepsilon(1 - cos\theta) = cos\theta + sin\theta cot\phi$$

$$tan\phi = \frac{1}{1+\varepsilon} cot\frac{\theta}{2} \qquad \textit{Eq. 5-17}$$

The parameter $\varepsilon = hf/m_e c^2$ is the normalized photon energy, where $m_e c^2$ is electron rest mass multiplied with the speed of light squared. Using the Eq. 5-17, we can investigate the relationship

between θ and ϕ. An increase in photon energy will reduce the recoil angle for a certain θ. We can also determine the limiting angles.

- If $\theta = 0$, meaning that the photon will continue the same path as the incident beam, then $\phi = \pi/2$ meaning that the electron will travel perpendicular to the incident path.
- If $\theta = \pi$, then the photon returns in the opposite direction of the incident beam resulting in the recoil electron having an angle of $\phi = 0$. Thus, we can say that an increase in scattering angle reduces the recoil angle and the opposite is true as well.

The following equations describe the relationship between the scattered and incident photons as either a function of the scattering or recoil electron angles. The derivation of these equations will not presented here, but can be found in reference (Podgorsak 2010).

$$hf' = hf \frac{{}^{1}\!/_{\sin^2\frac{\theta}{2}}}{{}^{1}\!/_{\sin^2\frac{\theta}{2}} + 2\varepsilon} \qquad \textit{Eq. 5-18}$$

$$hf' = hf \frac{(1+\varepsilon)^2 - \varepsilon(\varepsilon+2)\cos^2\phi}{(1+\varepsilon)^2 - \varepsilon^2\cos^2\phi} \qquad \textit{Eq. 5-19}$$

If we continue with the Eq. 5-18

1. If $\theta = 0$ then $hf' = hf$, meaning that there has been no transfer of energy and we have Thomson scattering
2. If $\theta = \pi/2 = 90°$ then the equation will be:
   $hf' = hf \ 1/(1+\varepsilon)$
   If we set limit $hv \to \infty$
   $hf' = \lim_{hf\to\infty}\left(\frac{hf}{1+\varepsilon}\right)$
   $= \lim_{hf\to\infty}\left(\frac{hf}{1+\frac{hf}{m_ec^2}}\right) = \lim_{hf\to\infty}\left(\frac{1}{\frac{1}{hf}+\frac{1}{m_ec^2}}\right) = m_ec^2 = 0.511\ MeV$
3. If $\theta = \pi = 180°$ then the equation is simplified to:

   $hf' = hf \ 1/(1+2\varepsilon)$
   $hf' = \lim_{hf\to\infty}\left(\frac{hf}{1+2\varepsilon}\right)$
   $= \lim_{hf\to\infty}\left(\frac{hf}{1+\frac{2hf}{m_ec^2}}\right) = \lim_{hf\to\infty}\left(\frac{1}{\frac{1}{hf}+\frac{2}{m_ec^2}}\right) = \frac{1}{2}m_ec^2 = 0.255\ MeV$
4. If $\theta = {}^{3}\!/_{4}\ \pi = 135°$ then the equation is simplified as:

   $hf' = hf \ 1.17/(1.17+2\varepsilon)$

$$hf' = \lim_{hf\to\infty}\left(\frac{1.17hf}{1.17+2\varepsilon}\right)$$
$$= \lim_{hf\to\infty}\left(\frac{1.17hf}{1.17+\frac{2hf}{m_ec^2}}\right) = \lim_{hf\to\infty}\left(\frac{1.17}{\frac{1.17}{hf}+\frac{2}{m_ec^2}}\right) = \frac{1.17}{2}m_ec^2 = 0.299\ MeV$$

Since we are interested in analyzing the backscattered photons, we should take note that the photon energy that can return has a limit of 255 KeV for true backscattering, meaning any increase in incident photons will be transferred to the recoil electron and not provide additional energy to the backscatter photon. Reducing the angle from 180° to 135°, assuming that we aim the source 45° downwards will increase the allowable energy to almost 15%. One can identify multiple angles and their corresponding energy levels to find the optimum solution, yet one has to work within the limits of:

$$0.255\ MeV < hf' < 0.511\ MeV$$

Figure 5-16, generated by using Eq. 5-18, shows that the relation between maximum backscattered photon energy and the backscatter angle is not linear.

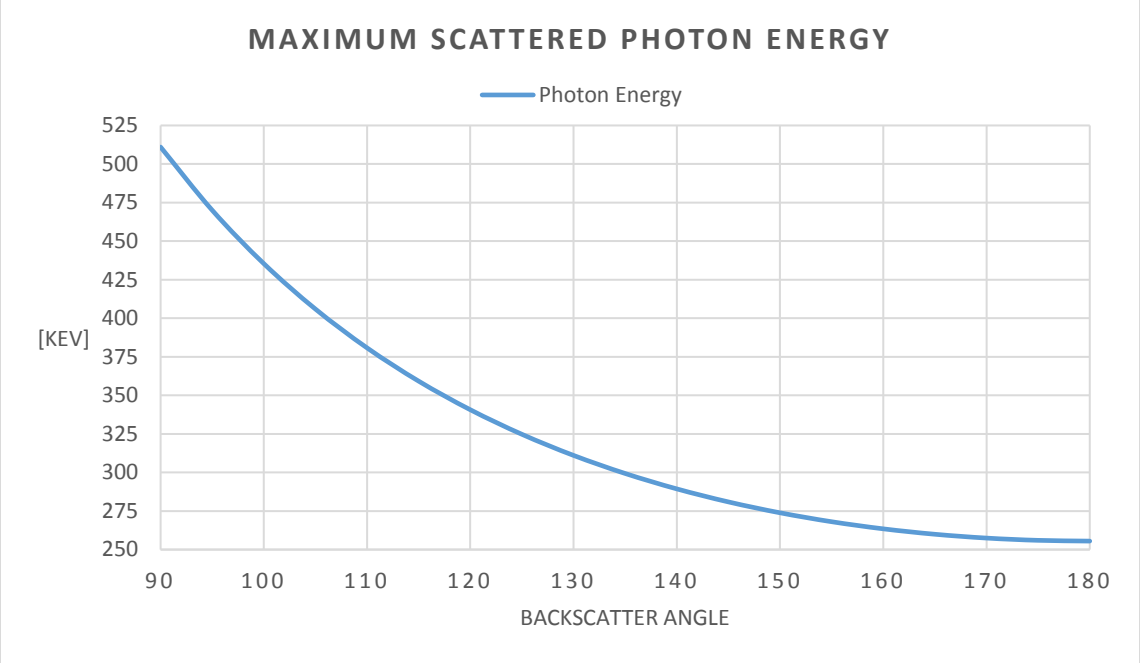

Figure 5-16 – Presentation of maximum photon energy at different backscatter angles

The differential cross section, or probability, of the occurrence of Compton scattering is described by the Klein-Nishina equation. The derivation of this formula is beyond the scope of this thesis, but is presented below (Podgorsak 2010):

$$\frac{d_e\sigma_c^{KN}}{d\Omega} = \frac{r_e^2}{2}\left(\frac{f'}{f}\right) = \frac{r_e^2}{2}(1+\cos^2\theta)\cdot F_{KN} = \frac{d_e\sigma_{Th}}{d\Omega}\cdot F_{KN} \qquad \textit{Eq. 5-20}$$

f	Incident photon frequency
f'	Scattered photon frequency
r_e	Radius of electron
$\frac{d_e\sigma_{Th}}{d\Omega}$	Differential electronic cross section per unit solid angle
F_{KN}	Klein-Nishina form factor, $f(hv,\theta)$
θ	Scattering Angle

Using the Klein-Nishina formula one can generate the graph in Figure 5-17. The graph shows the probability of the direction of scattering. The graph shows that if $\varepsilon = 0$, then there is equal probability for forward- and backscattering, the probability is halved for side scattering, 90°. With increasing incident photon energy levels, ε grows larger since $\varepsilon = \frac{hf}{m_e c\hat{}2}$, it results in the reduction of the probability for backscattering. At the highest energies, the innermost circle, backscattering is eliminated and only forward scattering will occur.

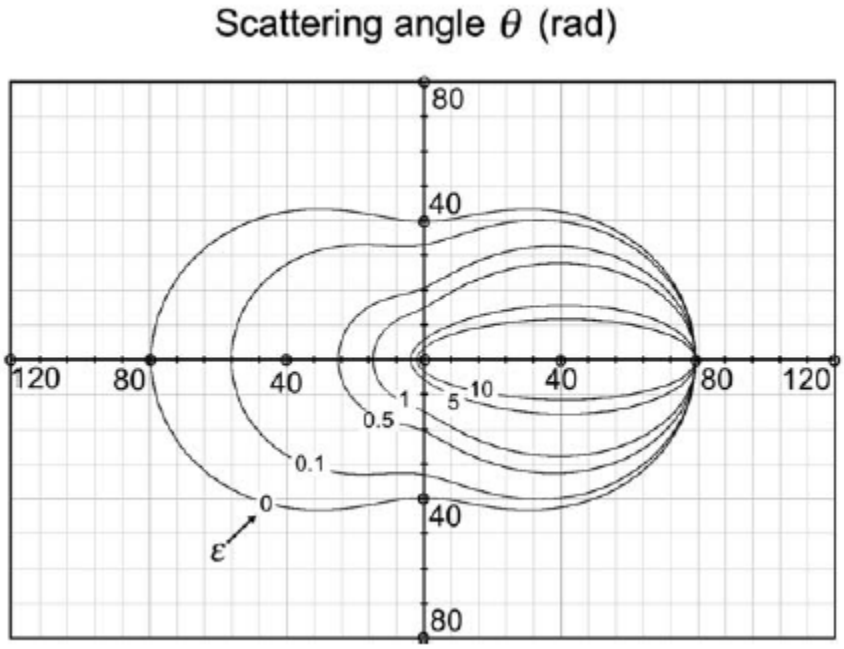

Figure 5-17 - Klein – Nishina scattering plot describes the probability of the angle of the photon as a function of photon energy (Podgorsak 2010)

5.5.4 Photoelectric effect

Interaction between the incident photon and a tightly bound orbital electron, most often results in the photoelectric effect. Mentioned previously, the difference between a tight and loose electron is the energy level of the incident photon. There is no scattering of the photon as its energy is completely absorbed by the electron. The transfer of energy will cause the affected electron to be ejected from its shell with an energy, E_K. The energy is equal to the incident photon, after subtracting the binding energy E_B The interaction is shown is Figure 5-18.

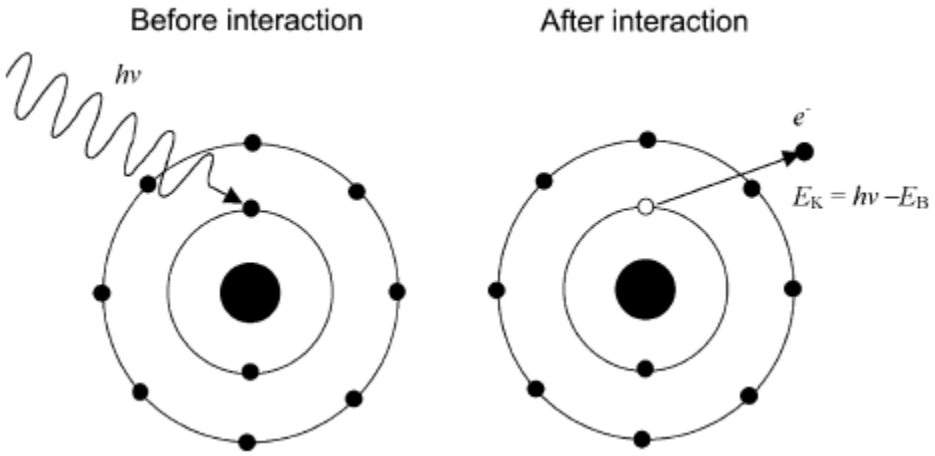

Figure 5-18 – Photoelectric absorption interaction (Podgorsak 2010)

Approximately 80 % of all photoelectric interactions occur with the K-shell, which is the innermost shell. The incident photon might not carry enough energy to eject the electron from the atom, but sufficient to force the electron to a higher orbit. This will leave a vacant shell. When an electron from a higher orbit fills the vacancy, two things can occur which are emission of a characteristic photon or an Auger electron. Auger electrons are created due to the Auger effect. When a vacancy in an atom is filled by an electron from a transition from another shell in the same atom, usually the energy transfer results in photons, but it can transfer to another electron which are called Auger electrons (Nave 2016a). The probability of either occurring is a function of the fluorescence (characteristic) yield ☐.

Similarly, to how we calculate the recoil electron scattering angle in the Compton scattering section, the angle is found by using the following equation:

$$P_v = P_e cos\phi \qquad \textit{Eq. 5-21}$$

Figure 5-19 shows the probability of recoil electron angle for different photon energy levels. Side scattering, $\theta = \pi/2 = 90°$, is limited to regions around 10 KeV.

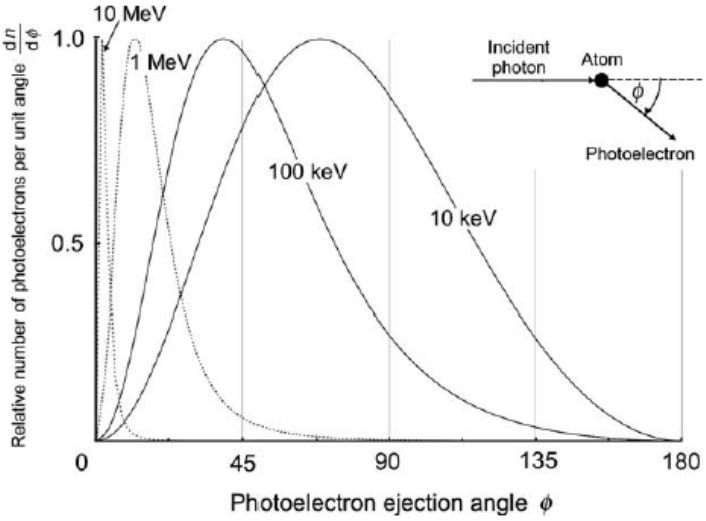

Figure 5-19 Angular Distribution of the recoil electron (Podgorsak 2010)

Atomic cross section, attenuation coefficient, for the photoelectric effect $a\tau$ exhibits a characteristic saw tooth, each peak corresponds to the orbital layers K, L, M, N. For example, for copper, the absorption edge for K is 8.98 KeV. The different materials shown in Figure 5-20 have different absorption levels and their electron behavior differs with the same incident photon.

Mentioned previously, the release of characteristic or Auger electrons is determined by the characteristic yield $\bar{\omega}$. When $\bar{\omega}$ is equal to one, no Auger electrons are release and if $\bar{\omega}$ is equal to zero, no characteristic photons are released. If $\bar{\omega}$ is between these two limits, then both are released during the interaction with an incident photon.

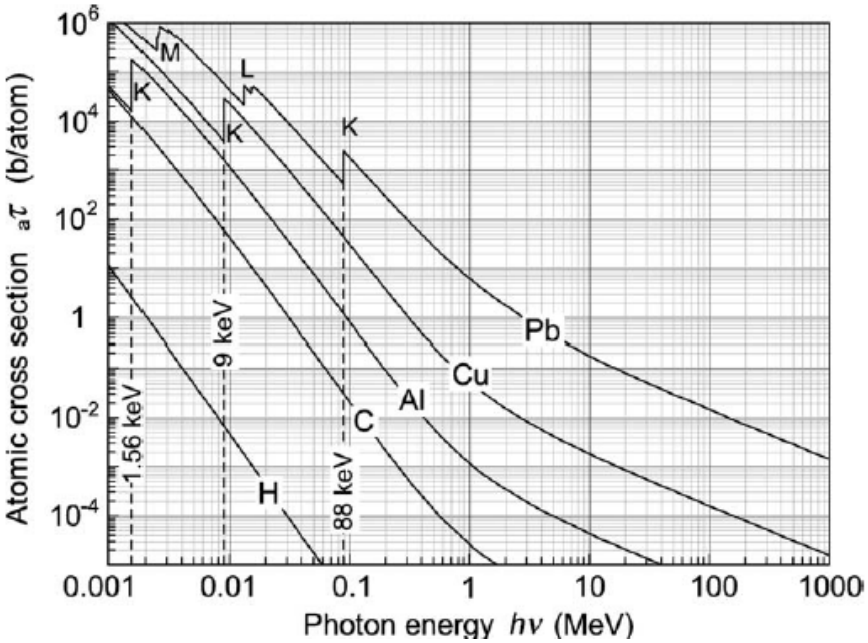

Figure 5-20 Absorption edges for different elements (Podgorsak 2010)

6 Analysis

So far, we have discussed generation, interaction and detection of x-rays. The subsequent chapter will cover how x-ray performs in scenarios where we will evaluate the cement. General assumptions made in the analysis are presented below:

- Initial strength of the beam is equal to the electron energy.
- Tool effects and size not considered, as the purpose of this analysis is to investigate the performance of the x-ray beam itself
- Temperature effects not considered
- No secondary scattering or radiation considered
- The matrix of the materials is assumed homogenous
- Porosity is not taken into account, as well as any influx of liquids or gases in the pores
- Presence of mud is not taken into account
- Single photon considered, no consideration given to the photoelectric absorption or Compton scattering cross sections
- Photon scatters at predetermined angle

6.1 Material Attenuation

In this section, we will investigate the attenuation of materials often found in a wellbore. The x-ray beam is in transmission mode, meaning that the beam travels straight through the material and is not reflected back towards the point of origin. This exercise is to see how different energy levels of x-rays perform depending on a type of material. The energy levels selected for the analysis are 200 KeV, 500 KeV, 800 KeV and 1000 KeV. These energies will be consistent throughout the analysis. We will present the materials selected and their composition if possible.

6.1.1 Casing

The first challenge of x-rays is to pass through the casing. We have selected L80 as our casing, which is commonly found in wellbores, as there are several permutations of L80 casing we will select L80 9-5/8, 43.50 lbf/ft with a thickness of 11.05 mm and density of 7.89 g/cm^3. The chemical composition is shown in Table 6.1.

Table 6.1 - Chemical composition of L80 casing and pure iron (Continental Alloy & Services 2017)

	C	Mn	Ni	Cu	P	S	Si	Fe	∑
L80	0.430	1.900	0.250	0.350	0.030	0.030	0.450	96.56	100
Iron	-	-	-	-	-	-	-	100	100

As we can see while L80 is an alloy, the dominating constituent is iron, comparing the total attenuation of L80 with pure iron is done to determine if iron can be used as an analogue with little deviation from the results. The National Institute of Standards and Technology (NIST) XCOM 2007 database (Berger et al. 2010) allows for inserting the chemical composition of materials and receive the mass attenuation for inputted photon energy levels. Figure 6-1 presents the results given by the program, and the similarities are evident.

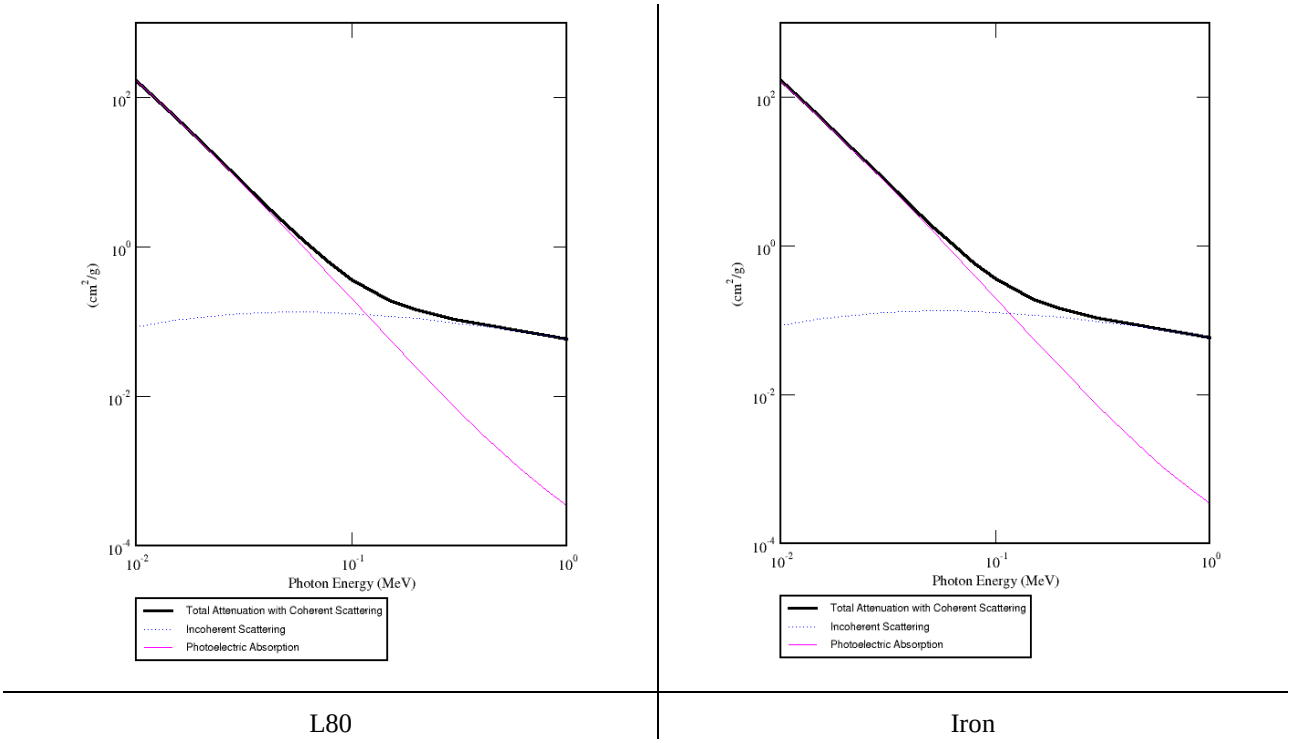

Figure 6-1 – Mass attenuation coefficients plots for L80 steel and pure iron given by XCOM (Berger et al. 2010)

If the dominating constituent, if of sufficient total percentage, in a material determines the mass attenuation coefficient, this could simplify possible future experiments.

Using the Eq. 5-13 for attenuation of an x-ray beam, we can generate graphs of the attenuation of the different energy levels in casing. This is presented in Figure 6-2

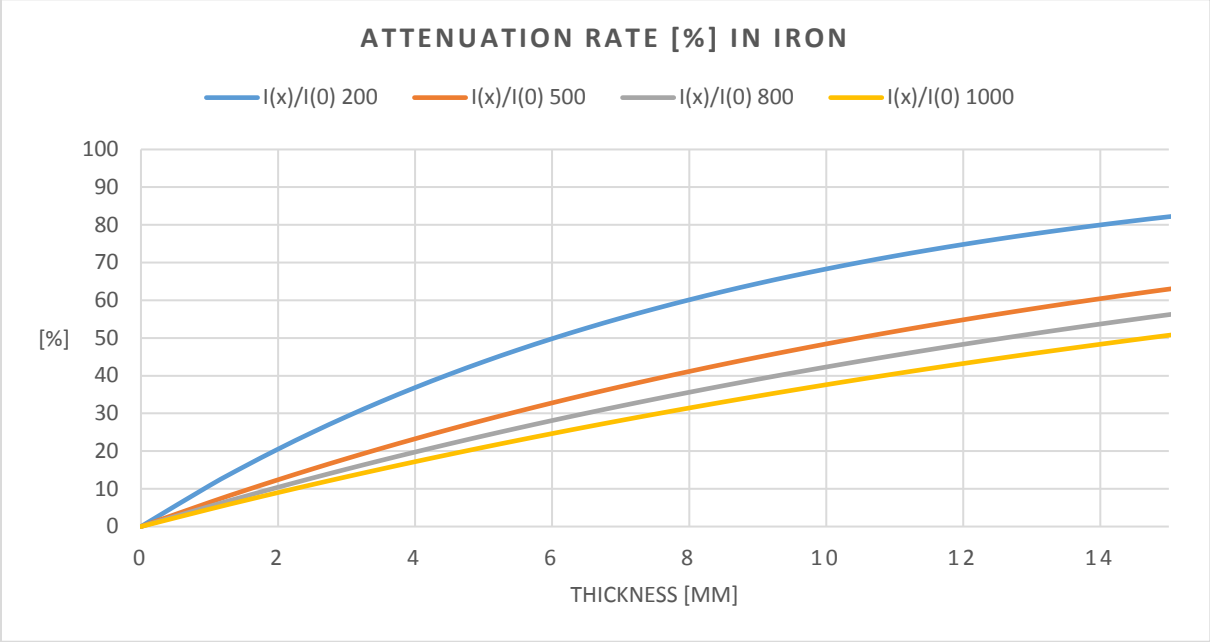

Figure 6-2 - Attenuation rate in iron by various X-ray energy levels

One should take note that the vertical axis is the attenuation of the beam through the various thicknesses relative to the initial beam. Furthermore, that the addition of attenuation and transmission rates is equal to the initial beam.

In the initial penetration of the casing, all the beams excluding the weakest has around 10 % of its beam attenuated at 2 mm. The weakest one is attenuated by 20 %. The 200 KeV beam is further weakened with increasing thickness and does not follow a similar rate of attenuation as the stronger beams. The attenuation rate is not linear, which is not surprising considering that Lambert's Law is an exponential function. The beams above 500 KeV see an increase in the difference between them as thickness increases. At 11 mm, the approximate thickness we are using in our scenario, the attenuation of the beam is presented in the Table 6.2:

Table 6.2 - Attenuation rate after 11 mm of iron

Initial beam	Attenuation rate (Approximation)
200 KeV	70 %
500 KeV	50 %
800 KeV	45 %
1000 KeV	40 %

Doubling of the initial beam does not equate in twice the reduction of the attenuation, and the difference of 10 % in attenuation rate stays relatively constant as soon as the beams have settled.

6.1.2 Cement and Foam Cement

Before we compare the performance of x-rays between class G cement and foam cement, we will again use the XCOM database to compare class G cement (Guner, Ozturk, and Erkayaoglu 2017) with assumed composition of standard concrete. The plots in Figure 6-3 show no discernable differences, so an assumption that the attenuation in both is comparable is valid.

Table 6.3 - Chemical compositions of class G cement, concrete and foam cement

	CaO	SiO_2	Al_2O_3	Fe_2O_3	MgO	SO_3	Na_2O	K_2O	Cl^-	N_2	∑
Class G Cement	63.52	18.69	4.35	5.19	1.43	2.94	0.31	0.54	0.02	-	98.99
Concrete	65	20	5	3	4	3	-	-	-	-	100
Foam Cement	38.11	11.21	2.61	3.11	0.86	1.76	0.186	0.324	0.01	40	98.19

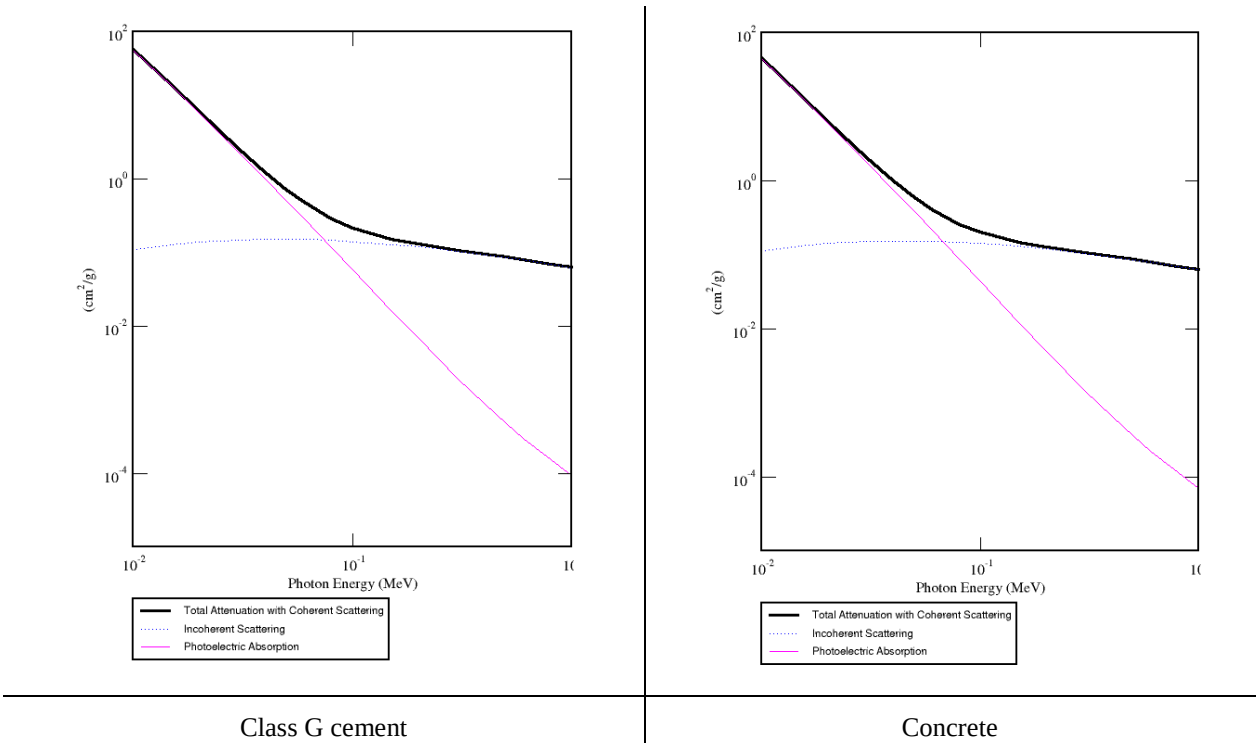

Class G cement | Concrete

Figure 6-3 - Mass attenuation coefficients plots for class G cement and concrete given by XCOM (Berger et al. 2010)

The result for attenuation by class G cement can be seen Figure 6-4, the selected cement has a density of 1.89 g/cm^3.

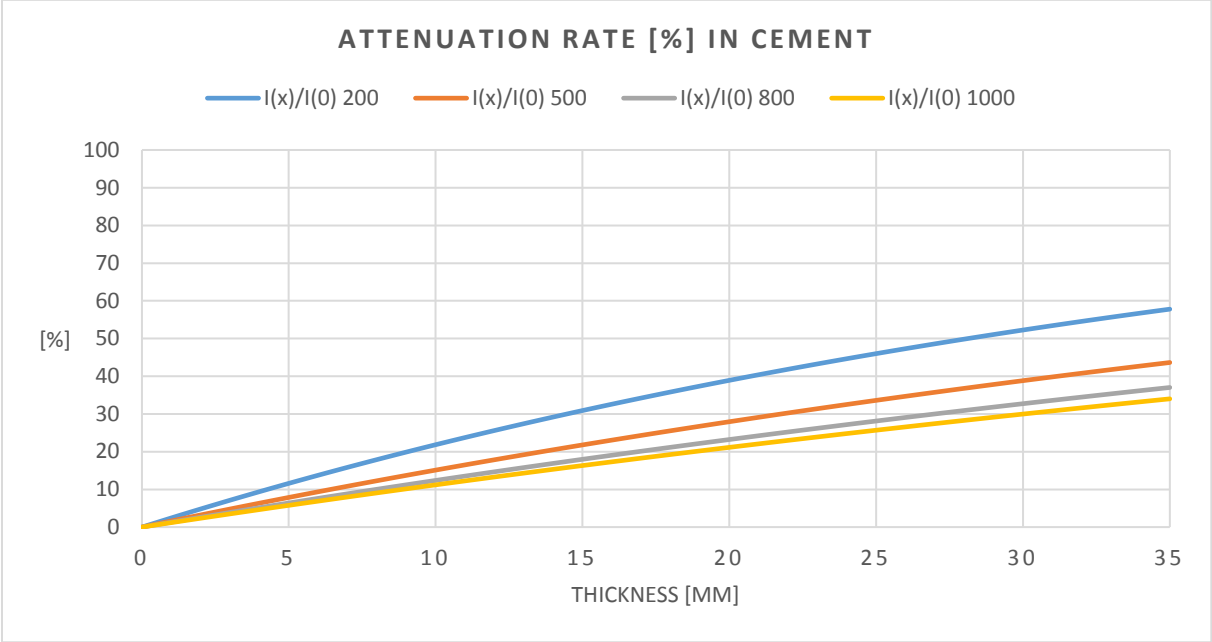

Figure 6-4 Attenuation rate in class G cement of various X-rays energy levels

Figure 6-5 displays the results for foam cement, with a density of 1.2 g/cm^3. Foam cement is sometimes necessary when the fracture pressure of the formation is such that the use of class G cement will cause the pressures downhole to exceed the fracture pressure. There are various ways

to reduce the density of cement and we have decided to insert 40 % of nitrogen gas (N_2) to the slurry. The assumption made with regards of inserting the values into the XCOM database is that if we have volume X, the Y percentage of N_2 introduction would reduce the constituents of class G cement by the same volume introduced. As mentioned in the beginning of the chapter we do not consider the porosity and assume that the investigated material is homogenous.

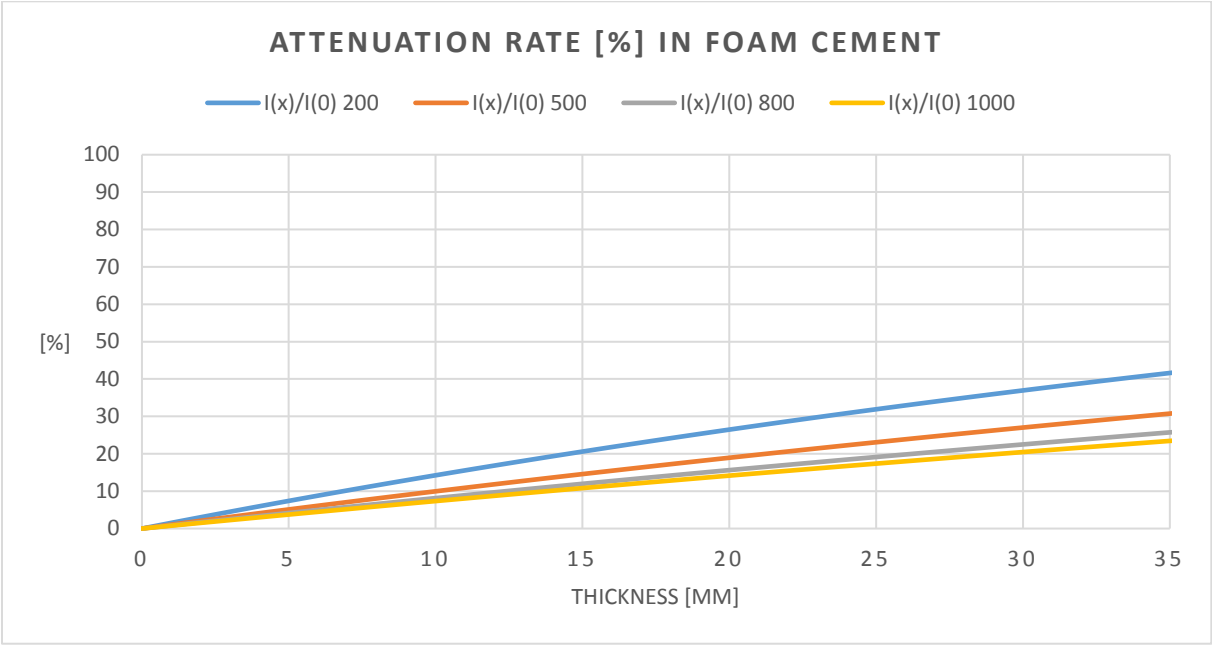

Figure 6-5 - Attenuation rate in foam cement by various X-ray energy levels

The reduction of the density from 1.89 g/cm^3 and 1.2 g/cm^3 has a considerable effect on the rate of attenuation. A 20 % difference at 35 mm for the 200 KeV beam is substantial, but the difference for the higher energy levels is reduced. At 33 mm, the attenuation in the two materials is are presented Table 6.4, the selection of the thickness is not arbitrary and the reasoning will be presented later.

Table 6.4 - Difference in attenuation rate between class G cement and foam cement after 33 mm

	Class G cement [%]	Foam cement [%]	Δ [%]
200 KeV	55.7	39.8	15.9
500 KeV	41.3	29.3	12
800 KeV	34.9	24.5	10.4
1000 KeV	32.4	22.3	10.1

For the energies above 500 KeV, the attenuation rate shows more linearity than the attenuation rate for the casing, indicating that the cement is an easier medium for the x-ray to travel through.

6.1.3 Seawater

The two final materials are seawater and gas. Inclusion of these materials is due to the high probability of finding them in the annuli. Gas will be covered in the next subchapter. In free pipe, meaning the absence of any material that provides zonal isolation, seawater occupies the annuli. The chemical composition of the seawater is the global average seen in Table 6.5:

Table 6.5 - Chemical composition of seawater (Duxbury, Mackenzie, and Byrne 2015)

	H_2O	Na	Cl	∑
Seawater	97	2	1	100

The density of the seawater is 1.03 g/cm^3, the graph of the attenuation rate is presented in the Figure 6-6.

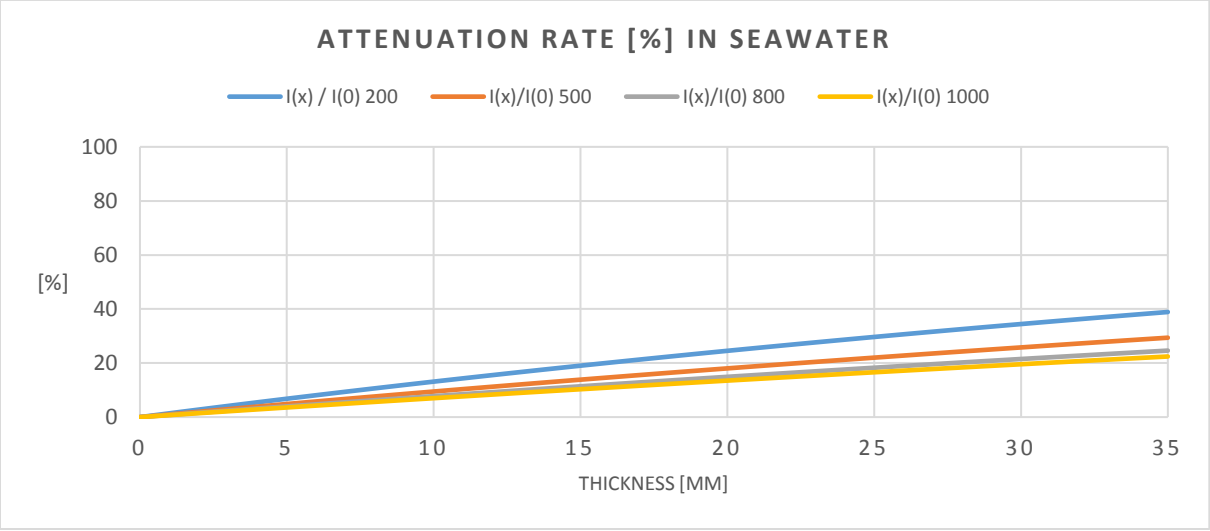

Figure 6-6 - Attenuation rate in seawater by various X-ray energy levels

We can see that the attenuation of x-rays in seawater and foam cement is similar, the values are presented in Table 6.6. This is due to a combination of the composition of foam cement and its corresponding density, and differences in the matrix is not considered and all are heterogeneous. Variations in the density and composition will result in an increase or decrease in the difference, but an issue arises. Which is if the contrast is sufficient to differentiate between the two, an educated guess would say that this is improbable as it could be relegated to noise in the interpretation.

Table 6.6 - Difference in attenuation rates between foam cement and water

	Foam cement	Water	Δ [%]
200 KeV	39.8	37.1	2.7
500 KeV	29.3	27.0	2.3
800 KeV	24.5	23.4	1.1
1000 KeV	22.3	21.3	1

6.1.4 Gas

Gas can be present in the annuli if there is a leak from the formation during cementing or debonding of cement. Unlike solid materials where their density is assumed constant regardless of temperature and pressure, gas density is a function of temperature and pressure. In our scenario, we assume methane in the annuli in a well with true depth of 3500 meters. Using the geothermal gradient and hydrostatic pressure gradient, we have that temperature is 87.5 °C and the pressure is 350 bar. The ideal gas law allows us to calculate the density with these parameters. The gas selected is methane, and has the following properties at atmospheric conditions seen in Table 6.7.

Table 6.7 - Methane properties at atmospheric conditions

Methane	At 25 °C and 1 atm.
Density	6.56×10^{-4} g/cm^3
Molar weight	16.04 g/mol

We will not show how to derive the ideal gas law to the result below. Using Eq. 6-1 results in the density of methane at 3500 m being 0.1872 g/cm^3.

$$\rho = \frac{M \cdot P}{R \cdot T} \qquad \textit{Eq. 6-1}$$

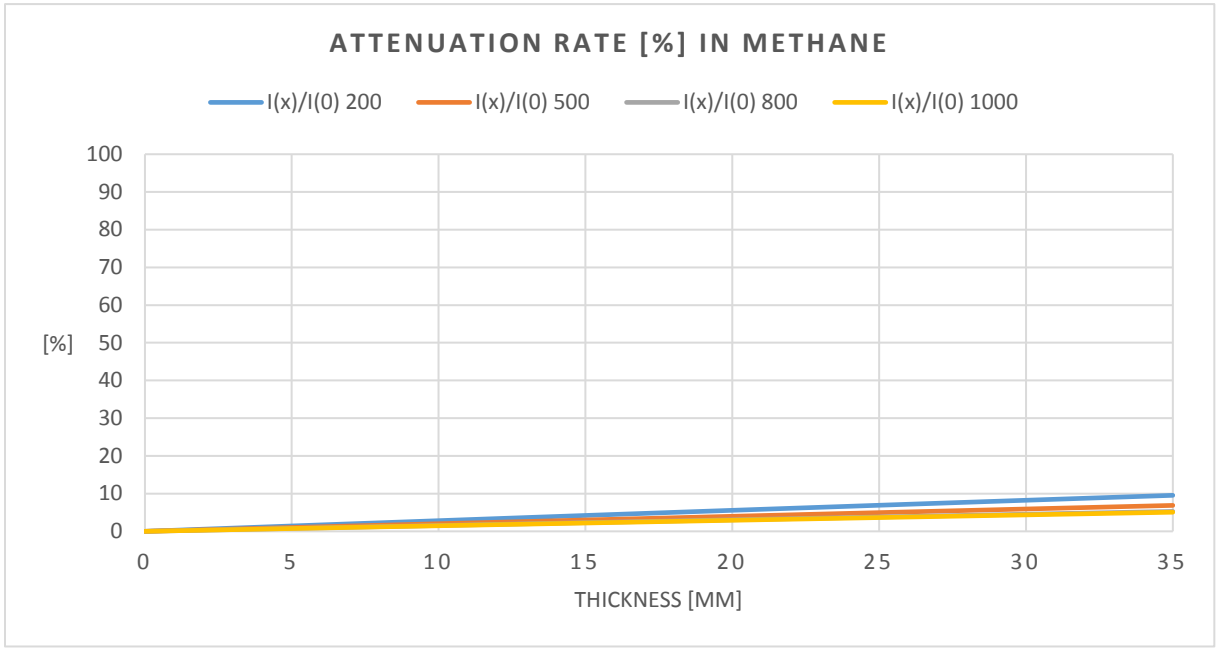

Figure 6-7 - Attenuation rate in methane by various X-ray energy levels

The attenuation of the x-ray beam in methane is minimal, Figure 6-7. The results is interesting is regards to gas channels in the cement, which is an issue for ultra-sonic tools appears to have little effect on x-rays. Detecting the contrast between cement and gas may be possible.

6.2 Backscattering

The plots above do not accurately describe how one would evaluate cement behind the casing found inside a wellbore, as they assume the strength of the beam only travels in one direction. This method works when one has access to the opposite side of the investigated material. Inside the wellbore access is only given from one side. To investigate any point beyond the casing requires the sent beam to return to its origin. This movement of the investigative beam is possible through backscattering. As the thicknesses downhole is usually known with a degree of certainty, a more accurate portrayal would be to determine how much of the signal is attenuated by a fixed thickness and investigation depth.

We will present five scenarios

- Concentric casing
  - Cement in the annulus
  - Foam cement in the annulus
- Eccentric casing
  - Cement in the annulus
  - Foam cement in the annulus
- Concentric with channels or micro annuli in the cement

The two main situations for the casing is either a casing being concentric inside the well with equal thicknesses of cement on all sides. Eccentric casing is when the casing is offset from the center of the borehole, in one case the thickness of the cement can be doubled on one side. Figure 6-8 shows the two situations, the inner circle is our casing and the outer casing represents the formation.

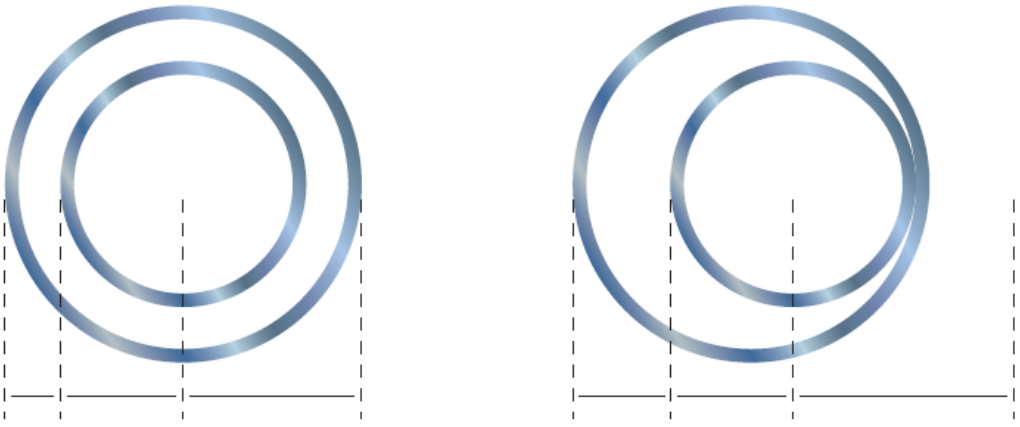

Figure 6-8 - Concentric (left) and Eccentric (right) casing strings (Abshire et al. 2012)

The inner and outer sizes can be different, but most often a large section of the production string has formation outside. As mentioned earlier in this chapter we will select a casing with the properties presented in Table 6.8:

Table 6.8 - Casing properties

L80

Outer diameter	9-5/8 inch
Thickness	11.05 mm
Weight	43.50 lbf/ft
Density	7.89 g/cm^3

As we will not exceed the diameter of the borehole, information of the formation is not important. The annulus has a thickness equal to the bit used to drill the borehole and subtracted with outer diameter of the casing. The 9-5/8 section of the well is often drilled with a 12-1/4 inch bit, meaning that the annuli thickness is equal to:

$$(12\frac{1''}{4} - 9\frac{5''}{8}) \cdot \frac{25.4\,mm}{1''} \cdot \frac{1}{2} = 33.34\,mm$$

We will use 33 mm as our annuli thickness in the subsequent calculations. Adding the casing thickness means that the distance from the inner diameter of the casing to the edge of annuli is 44 mm. The distance the beam needs to travel is twice the length, as the beam needs to return to reach the detector. The distance from the inner diameter to the source of x-rays as well as washouts in the formation are not taken into account. The additional thickness will of course further attenuate the beam. Illustration of the travel path is shown in Figure 6-9.

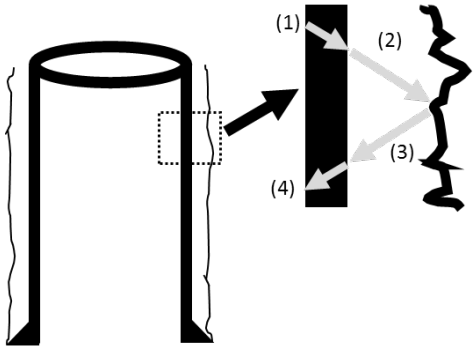

Figure 6-9 – Beam travel path as it originates in the wellbore and investigates the annulus before returning to the detector

In our scenarios, the path from (1) to (2) will be perpendicular to the casing, while the beam will return at an angle which will be the scattering angle of the photon. The consequence of the angle will be the additional thickness the beam has to travel before reaching the detector. Figure 6-10 shows the additional travel path due to angle of the retuning photon. The y-axis describes the factor the initial travel path increases with. Intuitively if the scattered photon returns in the same path as the incident path the result will be no change in travel path. The additional travel path does not increase rapidly until the scattering angle exceeds 130^o, using angles lower than this will results in debilitating attenuation of the beam.

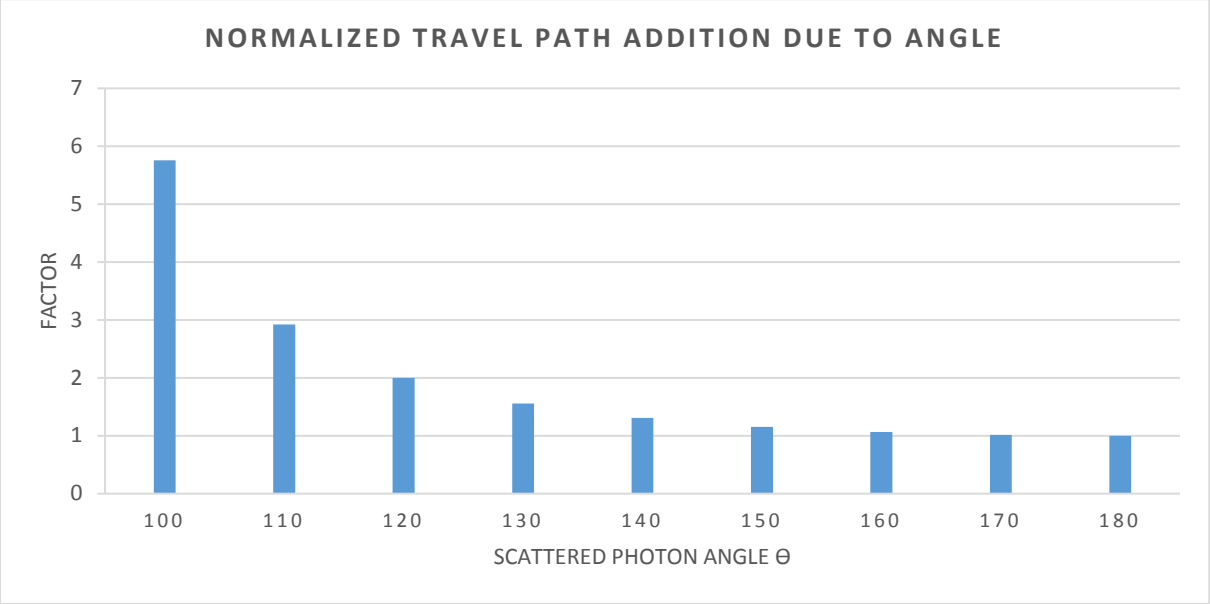

Figure 6-10 - Added travel path for the photon due to angle selection

Using Eq. 5-18, we can calculate the attenuation due to the Compton Effect, shown in Figure 6-11.

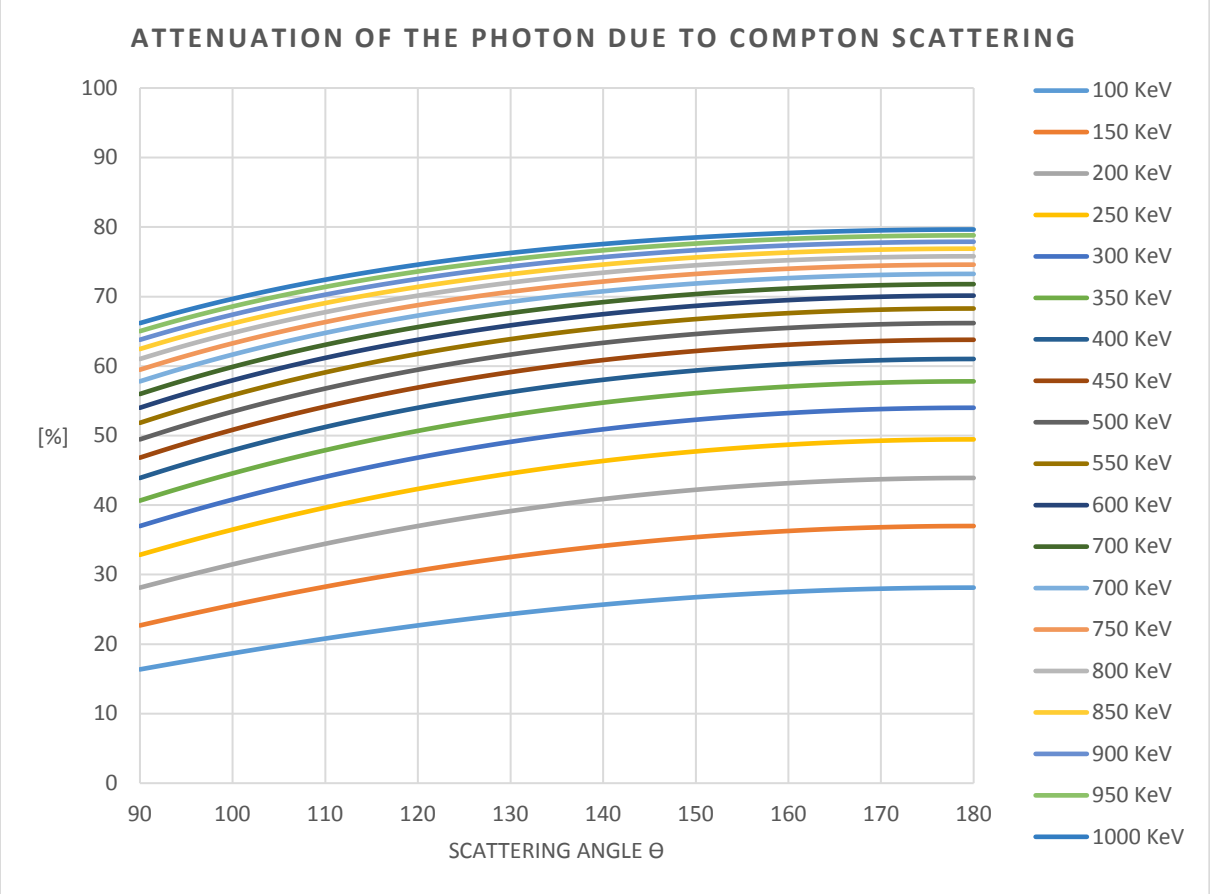

Figure 6-11 - Attenuation of photon energy due to Compton scattering

The attenuation of the scattered photon, after going through the Compton scattering process, due to angle is dependent on the initial strength of the beam. We can gather that the attenuation is similar if the initial strength of the beams are similar. The stronger the beam the more attenuation occurs regardless of angle. The weaker beams do not experience the same degree of attenuation, but in turn are more susceptible to photoelectric absorption. Concerning the angle, we should also remember that the maximum possible energy level that can return is confined between the energy limits:

$$0.255\ MeV < hf' < 0.511\ MeV$$

With the lower limiting angle being 180° and the upper limit is 90°. A 1000 KeV beam has only 200 KeV left after scattering at 180°, thus one should not be concerned by the limits as the beam is already weakened by the attenuation due to the material.

6.2.1 Concentric

The results from the model for our first scenario is shown in Figure 6-12.

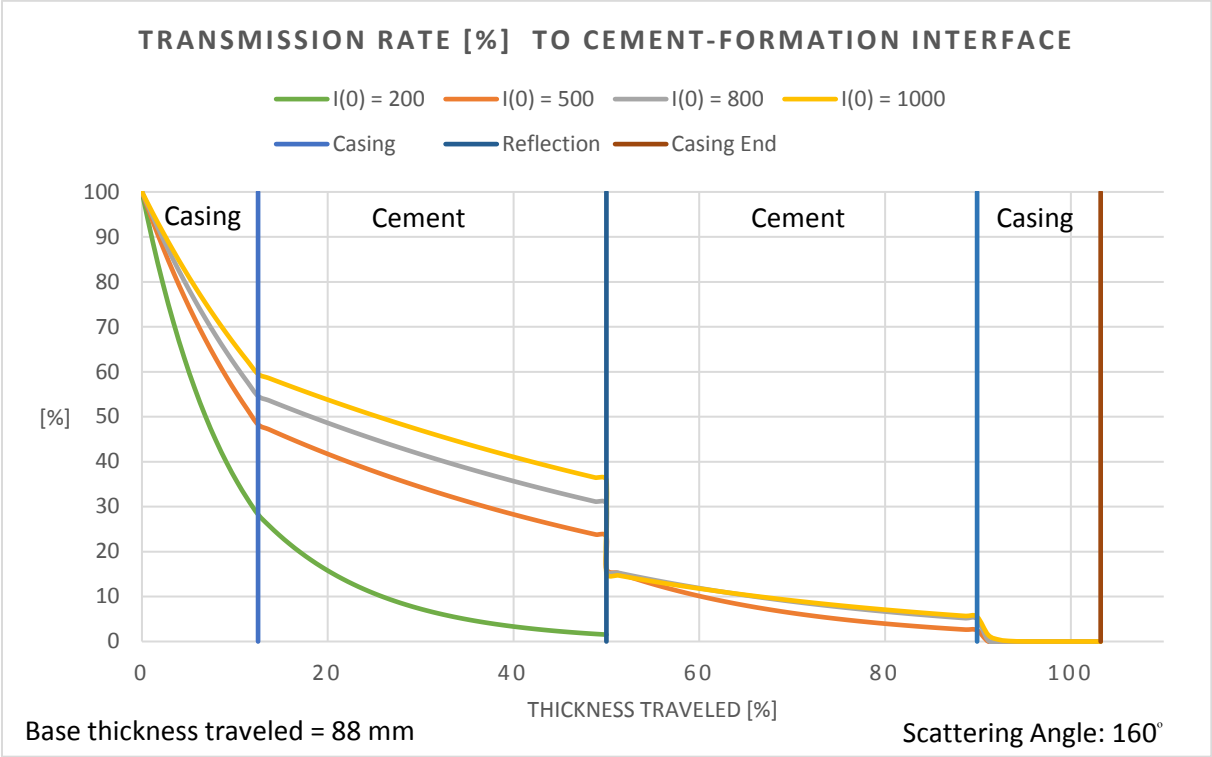

Figure 6-12 - Transmission rate [%] to cement-formation interface, angle 160°

Before discussing the results, we will explain the axes used in this graph and subsequent graphs, the y-axis describes the remaining intensity of the beam relative to the initial intensity while the x-axis describes the distance the beam travels relative to the base length. The base length for the concentric scenario is 88 mm, which is the casing and cement thickness multiplied with two.

When setting the angle to 160°, we follow the photon that is scattered at this angle. As not all photons will scatter at the same angle, the angle is dependent on where the photons hit the

electrons. If it the photon collides with the electron head-on the photon will be scattered 180°. From the Figure 6-12, it is apparent that the initial beam of 200 KeV does not have sufficient energy to return as is effectively stopped by the thickness of cement. Regarding the other beams, they do not manage to exit the casing with any significant energy left. After the Compton scattering, at the reflection line in the graph, the reduction of beam strength is too severe for it to return and penetrate the casing. Also of note is how the Compton Effect gives the remaining beams the same relative starting point after the scattering, regardless of the remaining strength of the beam prior to scattering.

A decrease in angle will reduce the attenuation due to the scattering effect, but doing so will increase the distance necessary for the beam to travel. In Figure 6-13, we decreased the scattering angle by 25° to 135° and consequently the length of travel for the beam increased from 90.8 mm to 106.2 mm.

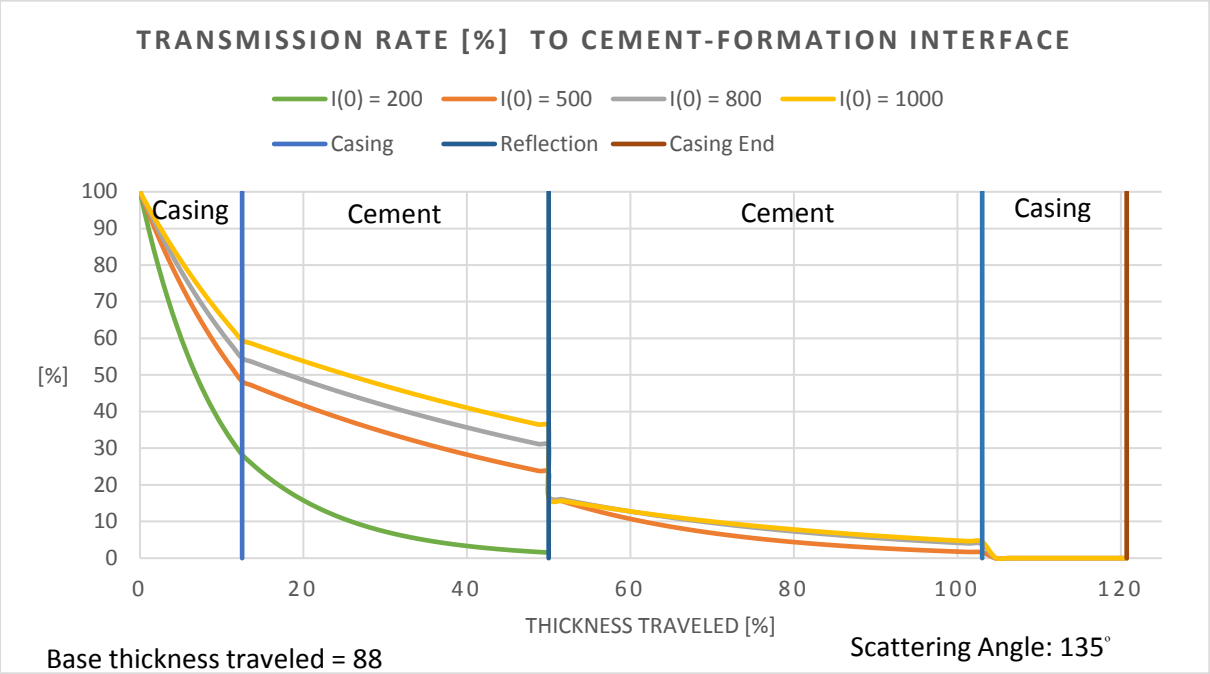

Figure 6-13 - Transmission rate [%] to cement-formation interface 135°

The results up to the reflection line are the same, as a change in angle does not have any consequence on these sections. The alteration in scattering angle does convert in a change in beam strength that would allow it to penetrate the casing. As any increase in beam strength due to the change in angle would be counter-acted by the increase in length.

Changing the material in the annulus from class G cement to foam cement will change the attenuation of the beam, as there is a change in density. Figure 6-14 shows the results.

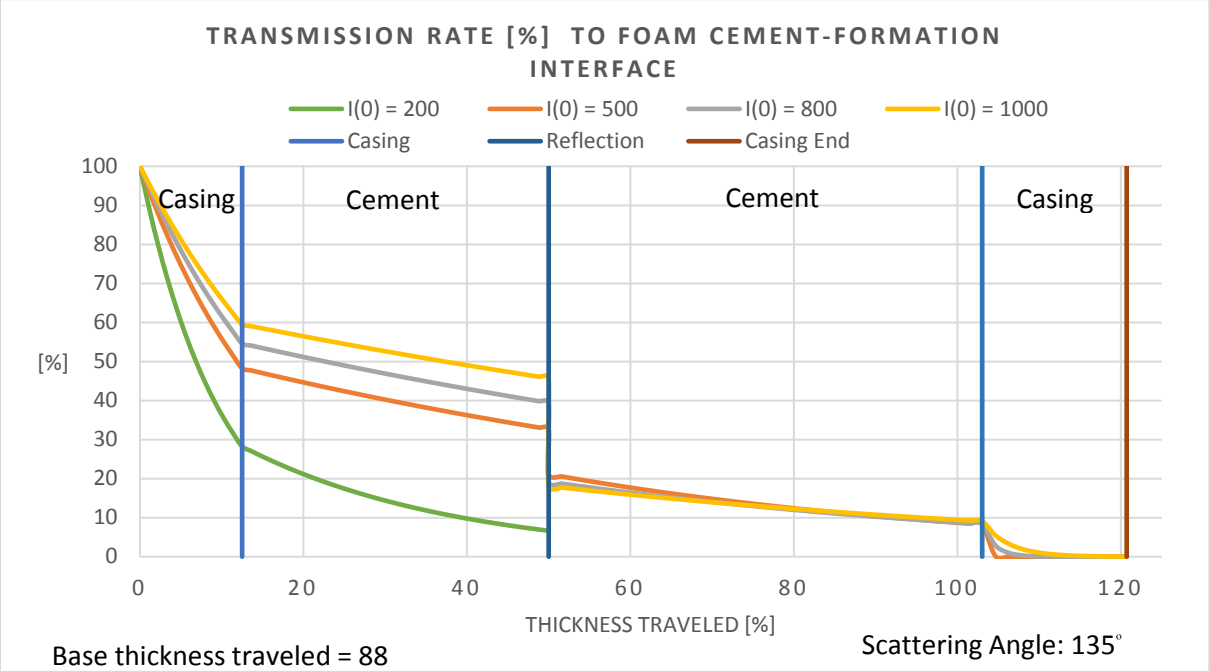

Figure 6-14 - Transmission rate [%] to foam-cement-formation interface 135°

The change in material had positive effect on the results, as the attenuation at the reflection point was not as severe as the case with cement. The positives of the change in density is counter-acted by the Compton Effect. The increased strength prior to the reflection point results in more attenuation due to the scattering. Seen in the graph the 1000 KeV beam has around 45% of its strength remaining at the reflection point, after the scattering only around 18% remain. The lines after the reflection point intersect due to the strengths being relative, as 18% of the 1000 KeV beam is 180 KeV while 20% of the 500 KeV beam is 100 KeV. The 500 KeV beam will experience increased attenuation rate due to initially being weaker. The final result does not change with a change in density. The remaining strength of the beams at the end of the casing is improved but not sufficient to exit the casing.

6.2.2 Eccentric

Based on the results of the previous scenarios, the doubling of the cement thickness will lead to earlier full attenuation of the beam. On the next page Figure 6-15 and Figure 6-16, show the results. In the eccentric scenarios, the base length is 154 mm, which is the sum of the casing thickness of 11 mm and the cement thickness of 66 mm multiplied with 2. We do not consider the opposite side in this scenario, where the base length would be 44 mm of only casing.

The foam cement allows for greater transmission rates through the cement, but this is not of consequence due to the small amounts of photon energy left before the penetration of casing occurs.

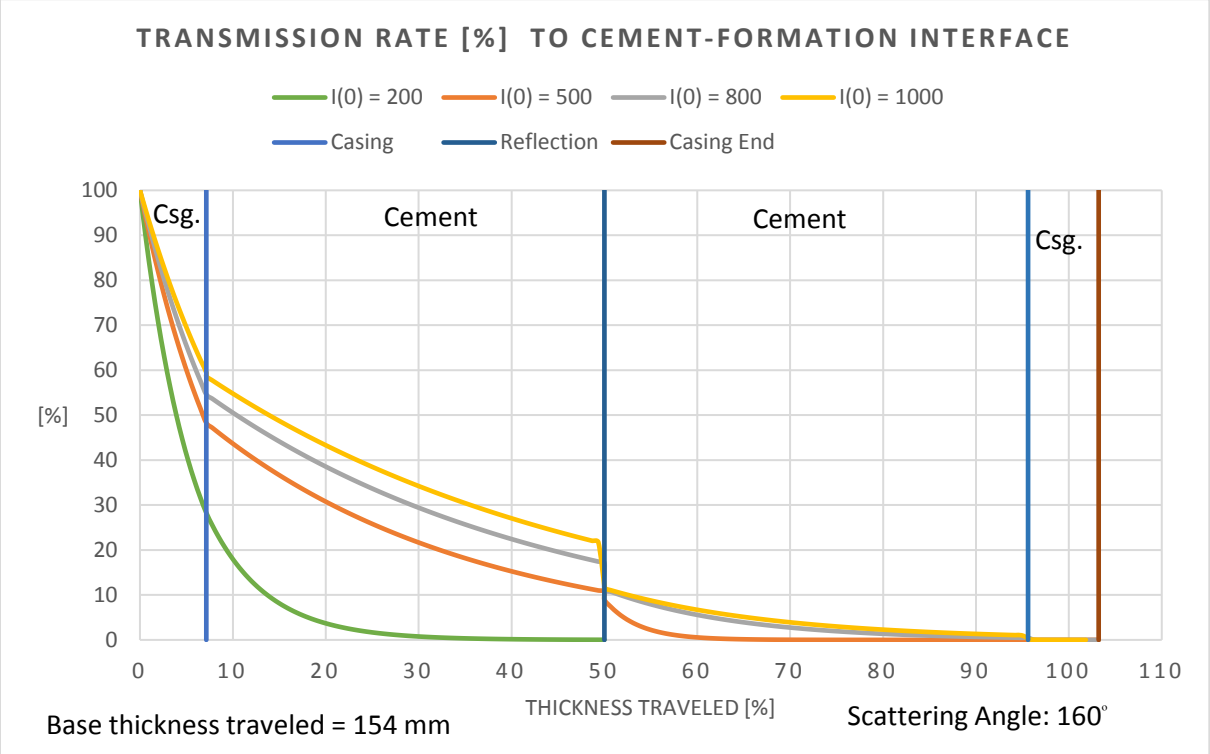

Figure 6-15 - Eccentric casing, Transmission rate [%] to cement-formation interface 160°

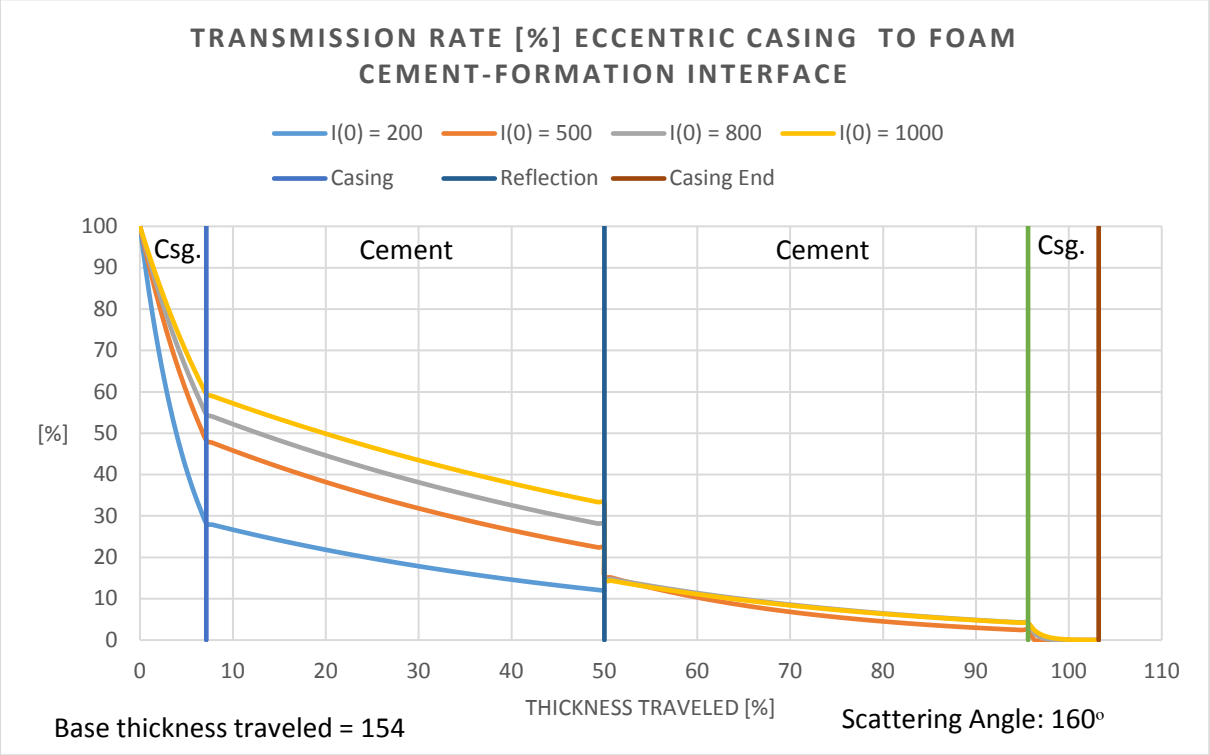

Figure 6-16 - Eccentric casing, Transmission rate [%] to foam-cement-formation interface 160°

6.2.3 Micro annuli and channeling

Channeling in cement due to improper or failed cement job is an issue, as channeling can allow for communication across the barrier. To evaluate how the detection of these channels would reflect on the graph, we have placed two channels in the cement. These are:

- Water channel
  - Depth: 9 mm in cement
  - Diameter of channel: 30 % of thickness, approximately 10 mm
- Gas channel
  - Depth: 24 mm in cement
  - Diameter of channel: 15 % of thickness, approximately 5 mm

We are using the data from Figure 6-12 as a foundation. The intention of this scenario is not to determine if the beam has sufficient energy to return to origin, but the investigation of x-ray performance in light of the presence of channels in the cement. Therefore, we have shortened the x-axis to focus on the cement sections.

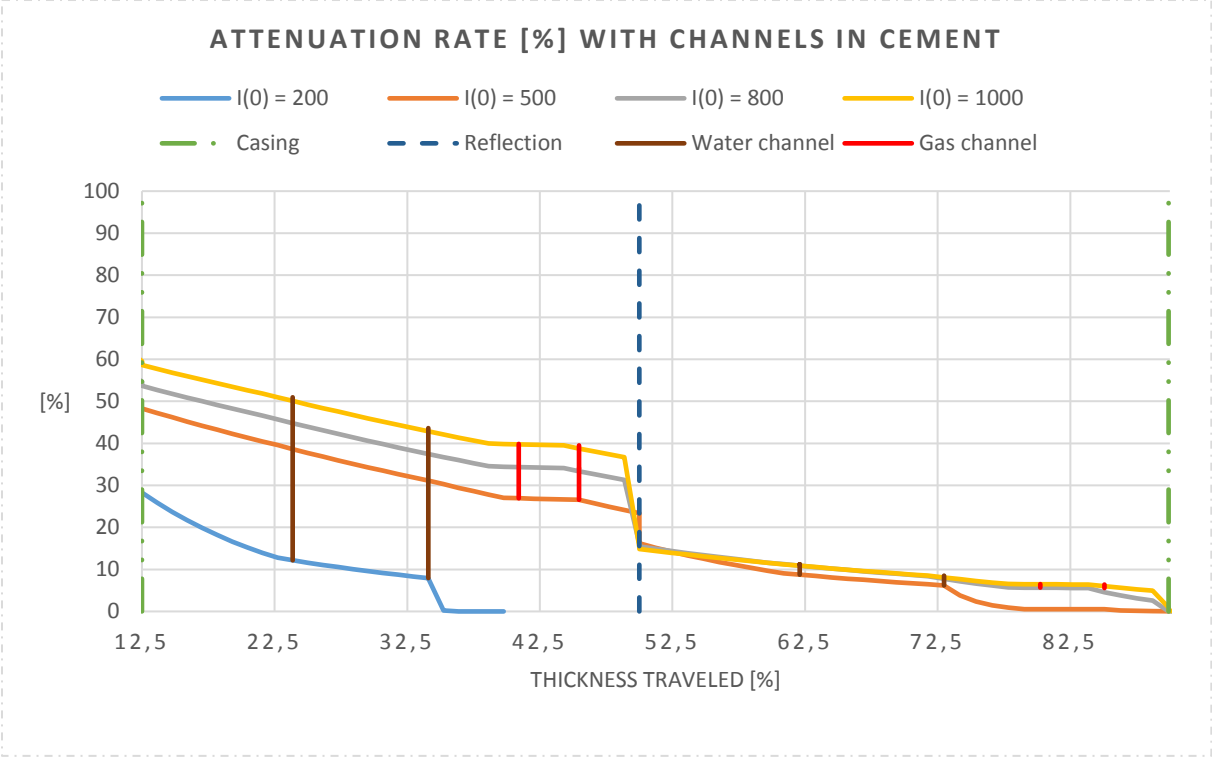

Figure 6-17- Transmission Rate [%] with channels in cement

The intervals between the brown and red lines in Figure 6-17**.**, indicate the placement of the water and gas channels respectively. Interestingly the water channels seem to have little effect on the higher energy beams, but the weaker ones experience a sudden drop in transmission rate after moving through the cement. This could be due to the inability of the Eq. 5-13 to portray accurately low energies in this situation, since we calculate a new attenuation coefficient with the energy that remains after being attenuated by the water channel. Gas channels on the other hand have a visible

effect on the results, since the density of the gas is so low little attenuation occurs. This is seen as the transmission value repeating over a thickness interval on the graph. If this repeating pattern can be detected on the log, if one takes into account noise and tool losses is uncertain.

Using experimental data for the performance of sonic and ultra-sonic tools (Jutten and Hayman 1993), we have investigated the effect of micro annulus on a relatively weak beam compared to the previous scenarios. The beam selected is 62.5 KeV, which is 16 times weaker than the 1000 KeV beam. The selection is due to weaker beams being more susceptible and if the weak beam shows no signs of being affected by micro annuli, one can assume stronger beams will not be affected. The micro annulus sizes are based on experimental data mentioned above, and are as follows:

- Water filled micro annulus
    - Size: 0 to 1000 µm, with 40 µm increments
- Gas filled micro annulus
    - Size: 0 to 25 µm, with 1 µm increments

Figure 6-18 presents the results, as seen micro annuli do not possess sufficient thickness to change the results severely. The x-axis represents the fraction of a cement sample filled with either water or gas, starting with a cemented annulus at 0 before being completely filled with either phase at the end of the axis. The y-axis represents the change in attenuation relative to the initial attenuation of the beam in a completely filled micro annulus.

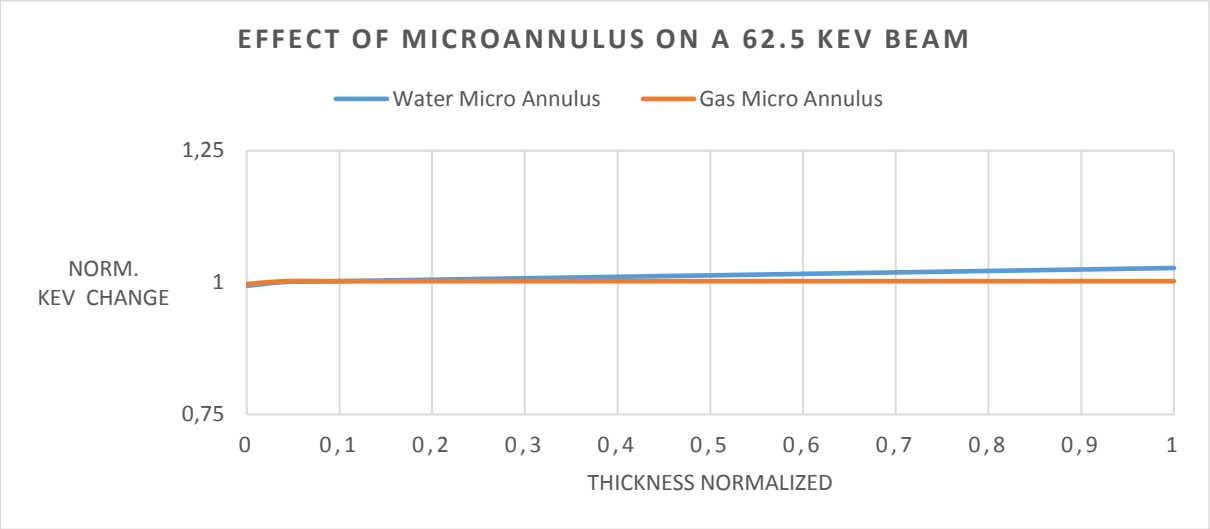

Figure 6-18 - Effect of micro annulus on a 62.5 KeV beam

6.2.4 Transmitting at an angle

In the previous scenarios, the beam was transmitted at an angle perpendicular to the casing. The intention behind Figure 6-19 was to investigate if there was any change from the previous figures if the transmitter itself was transmitting the beam at an angle. In the previous scenarios, the reflected beam is traveling the longest distance, due to the change in angle increases the travel path. Transmitting at an angle of 45°, relative to the casing, allows the incident beam to take the brunt of the additional thickness that comes with traveling at an angle. The reflected beam is scattered at an angle of 135°, such that it would travel perpendicular to the casing. Setting the returning travel path equal to the base thickness of the casing and cement, which is 44 mm. The results from these set of angles is that the additional travel path the incident beam has to travel through as expected increases the attenuation prior to the reflection line. The increase in attenuation prior to the scattering would mean less attenuation due to the Compton Effect. Comparison of the values, from Figure 6-13 and Figure 6-19, show that the former statement holds true. The issue is that the incident beam is more severely weakened prior to the reflection, meaning that while the reflected beam suffers less attenuation due to Compton it is overall weaker.

Table 6.9 - Incident and reflected beam comparison for angled and non-angled transmitters

Initial: 1000 KeV	Incident beam [%]	Reflected beam [%]	Difference [%]
Transmitted angle: 0	36	16	20
Transmitted angle: 45	22	13	9

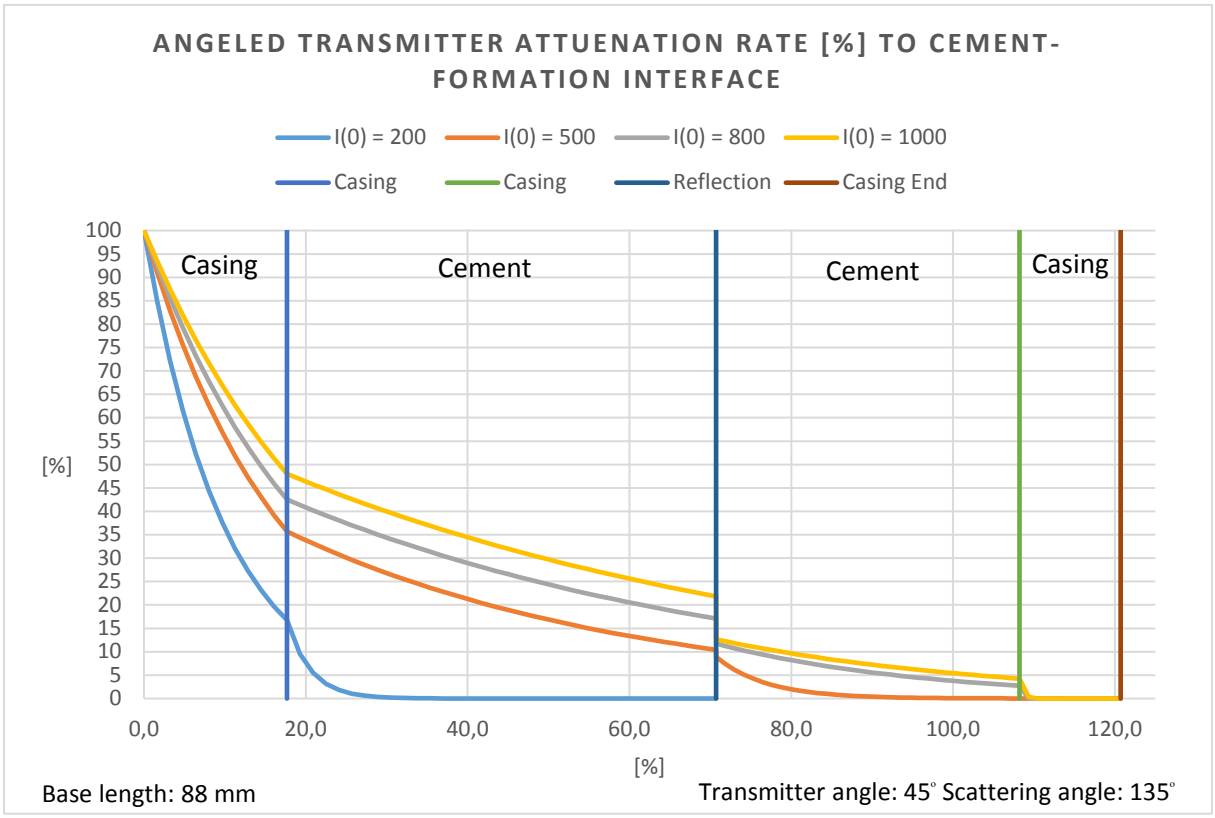

Figure 6-19 - Angled transmitter attenuation rate [%] to cement-formation interface

7 Discussion

The challenges of P&A are prevalent, and the cost for the industry is substantial. Therefore, the proper cement evaluations are essential. The intention behind this thesis was to evaluate the feasibility of using x-rays downhole, numerous considerations would need to be accounted for if one wishes to realize the use of x-ray to evaluate the barriers behind casing.

One key issue with any current technology used for cement evaluation is that they do not measure actual zonal isolation, but infer it through other physical parameters. No tool or method is able to determine the quality of the hydraulic seal the cement provides, except for a pressure test. Yet the acoustic tools dominate the evaluation business as they provide the simplest way to infer isolation and in a conservative industry, usually the proven method is always preferred.

7.1 Fiber Optics

Placing fiber optic cables permanently behind the casing may allow with a degree of uncertainty to evaluate the cement. The monitoring would have to be continuous so that any leaks that can occur throughout a wells life are detected. This predicates that the primary cement job has been done properly and tested. If access to the annuli is available, these cables can be placed in each annulus to improve accuracy of the measurements. This may be one-step in the direction of solving cement evaluation through multiple casings. The increase in initial investment required to install fiber optics in the well may be not welcomed, but it is miniscule compared to the costs of complex P&A operations.

7.2 X-rays

The following subchapters will discuss the various topics pertaining to x-rays covered in this thesis.

7.2.1 Generation of Photons

There are many unresolved issues concerning employment of x-ray downhole, from generation to detection. The generation of x-rays, as mentioned in chapter 5.2, can be done in several ways. The piezoelectric crystals are currently not suitable for our application. The temperature cycles are difficult to realize downhole, as the initial temperature would help with the heating of the crystal. The subsequent cooling of the crystal is the issue, leaving the crystal to cool by itself would limit the logging speed. If each small section takes several minutes, the cost of the cement evaluation would not make economic sense.

The use of radioisotopes carries with it special considerations. However, while issues like temperature is not as significant and some are able to provide a 662 KeV beam, the source will always emit radioactivity. Safety precautions that would be required to be set in place may complicate operational procedures. The only way to generate radiation with an on-demand function is by using electricity.

The x-ray tube satisfies the safety and time aspects, but is difficult to engineer. The design of the tool would need to consider several aspects as such size, heat generation and placement of

transmitter and detector. The diameter of the production casing only allows for small diameter sized tools. Current small sized generators do not have the output required to satisfactory investigate beyond the casing. To accelerate the electrons with significant energy, high voltages are required. A 1000 KeV beam requires a supply of 1000 KV, and this is the peak energy of the beam. As seen by the bremsstrahlung graph, Figure 5-4, only a small percentage of the photons has the energy equal to the incident electrons, the majority will possess less energy. The consequence is that one should generate a peak energy level higher than required for the investigation. In the analysis, we selected 200, 500, 800 and 1000 KeV, which we felt was appropriate as 200 KeV should be achievable and radioisotopes can reach 662 KeV. Higher than this, we approach energy regions that are currently not achievable except for facility housed generators.

To work around the low probability of photons with peak energy, one can increase the number of transmitted photons at the target as one would then increase the probability of achieving photons with peak energies equal to the incident electrons. As well as increasing the intensity of the beam. Two parameters that control the number of photons generated are the amperage and exposure time. How to balance these two parameters if the voltage is set is important. Increasing the amperage will make it more difficult to transfer power through the cables downhole, since the cables have limits on the number of watts that can be transferred through them. While decreasing the exposure, time can reduce the logging speed. The combination of all three parameters voltage, amperage and exposure time affect the generated temperature. Since the generator is inherently inefficient at converting electrons to photons, most of the energy applied to the electrons are converted to heat.

7.2.2 Heat

We have not discussed the generation and dissipation of heat in a wellbore in detail, but it is an important factor when using an x-ray tube. If the tube is run without any safety guards set in place, the scenario of the anode melting is a possibility, which is an indicator of the temperatures possible when using an electric x-ray generator. Assuming the tool is run properly the heat in the anode will dissipate into the surroundings. The initial temperature in the borehole is elevated compared to surface and increases with depth, meaning any surface safety ratings for the electrical tubes cannot be used. Dissipation of heat from the tool to the surroundings must be considered, as it can have an effect on casing and cement, and subsequently the well integrity.

7.2.3 Detector

The detector method most often used for radiation is a scintillator coupled with a photomultiplier. As mentioned in chapter 5.4, the detector capability is reduced if the temperature exceeds its operational work window. Specialized detectors developed for the industry still have too low of a temperature rating to withstand the temperatures in the well when the generator is in use. The whole method of investigation is mute if one is not able to measure the photons. The detector itself is a source of attenuation of the beam, seen in Eq. 5.12. It is as well governed by the same principles of photoelectric absorption and Compton scattering, and their corresponding cross-sections. The efficiency of the detector is important as the number of photons lost due to attenuation when traveling through the materials is already significant. It could be pertinent to consider using several

detectors to increase the probability of gathering the returning photons. One should be aware of the natural radiation from the formation as these could influence the readings, one solution could be to record the data before using the generator and filter out the natural radiation.

7.3 Analysis

Concerning the analysis there are several key points that need to be addressed. We considered a single photon under the assumption that is not absorbed or scattered before reaching the cement-formation interface. On the one hand, the validity of this can be discussed, but we felt that the probability of a single photon making it to the reflection point was high. On the other hand, the probability of absorption after the reflection point is high, yet we assumed no absorption effects. It is possible to calculate the probabilities for each effect, but these have not been included in this analysis.

Determination of the optimal placement of the detector in regards to the angle window the photons can scatter is a key point. Since the angle is the parameter that determines the distance between the transmitter and detector, a decreasing the angle from a straight return at 180° to an angled return allows for increased distance between sender and receiver. Any change will consequently change the travel path of the beam, which has to be accounted for concerning the attenuation. Considering the temperature sensitivity of the detector, it may be beneficial to space the two components at the maximum allowable distance.

7.3.1 Attenuation

The material attenuation graphs showed that density is a determining factor for the performance of x-rays. As expected iron severely affects the transmission of x-rays, as it possesses a high atomic number. Low energy beams, as the 200 KeV will almost be 80% attenuated at the end of 15 mm of iron. Interestingly, among the higher energy beams, 500, 800 and 1000 KeV, doubling the energy from 500 to 1000 KeV does not result in doubling of the transmission. Since the Lambert's law is an exponential function the difference in attenuation between the initial strengths is not linear, and it will increase to a peak before decreasing. This would require thicknesses exceeding ones we have used in the analysis. This leaves us in the position of having to make a decision if the increase in transmission validates the increase in power of a proposed energy source.

Low-density materials such as the foam cement and gas appear to follow a linear trend, but this due to the thickness interval chosen. Extending the thickness interval further and the shape of the lines will appear similar to the one of iron. Nevertheless, in a well these can essentially be regarded as linear. An issue arises with materials with similar densities seen with our selected foam cement and seawater. Due to the composition and density combination, these materials have similar attenuation effect on the x-ray beam. This poses a challenge, as the model could not differentiate between foam cement and seawater, seen in Table 6.6. This could be due the model assumes that the investigated medium is homogenous, and does not account for the porosity.

Concerning voids and micro annuli in the cement, the size of the void was the deciding factor in this analysis. When we inserted channels in the cement, Figure 6-17, the seawater was not discernable from cement if the strength of the beam was high. As the contrast between the two

materials is not greatly apparent, it can cause a challenge as any small and unexpected change could be relegated to noise in the signal interpretation. The weaker 200 KeV beam showed a noticeable difference between seawater and cement. Upon reentering the cement the 200 KeV beam experienced full attenuation, this could be due to the inability of Lambert's Law to describe situations where the beam transitions from one material to another. The gas-filled voids were very noticeable, since gas will cause minimal attenuation of the beam. Still the size of the void must be sufficient for it to display on any graph, Figure 6-18 shows a weak beam that is susceptible to change in materials experiences little change due to micro annuli. Based on this one can assume that x-rays are not affected by micro annuli in the cement.

7.3.2 Travel path and Compton effects

As seen by Figure 6-10 and Figure 6-11, reduction of the scattering angle from 180 degrees increases the travel path and decreases the attenuation due to the Compton Effect. Which of the two effects that contribute the most to the attenuation of the beam is dependent on the initial strength of the beam. The margins of penetration through the casing with x-ray is already slim, therefore the optimization of the angles so that it allows the maximum possible return is necessary. To counteract the effect of the Compton we investigated if transmitting at an angle would increase the strength of the returning photon. Transmitting at the angle of 45° increased the attenuation of the beam, prior to the reflection point, as expected due to the increase in travel path. At the reflection point, the photon would scatter at an angle that would set the travel path equal to the thickness of casing and cement. As seen in Table 6.9 increasing the initial travel path had a positive effect on attenuation from Compton, but the weakening of the initial beam had a negative effect on the overall strength of the returning beam compared to the non-angled transmitter.

The maximum energy limits for what the backscatter photon can possess should not be of concern. The reasoning behind this is simple as any of the energies that are used will not be able to reach the necessary energy levels that will cause the attenuated energy will reach the limits.

7.4 Final thoughts

X-ray was not able to evaluate the cement in any of the scenarios that were set-up. The scenarios themselves were realistic, and acoustic tools would have been able to detect cement with some degree of certainty. The initial travel to the formation was manageable for all beams except the 200 KeV beam. The scattering of the beams due to the Compton Effect resulted in attenuation so severe that they had no remaining capability to penetrate the whole thickness of the casing. Alteration of the transmitting angle had a negative impact of the strength of the scattered photons. No optimization of the selection of angles was done in this analysis, leaving the door open for finding the optimum set of angles that would maximize the strength of the scatter photons. As it pertains to the analysis, initial investigations of x-rays viability to analyze cement has shown that reaching the cement-formation interface is too demanding of x-rays and other methods should be considered. Since distance traveled by the beam and the consequent attenuation is one of the main limiting factors, one can consider shortening the length that would be required to travel. Shifting the focus of investigation from cement-formation bond to the cement-formation bond and a shorter distance in the cement. Essentially the use x-rays in this analysis would measure the density of the

materials in its path, and there are existing tools and methods that are able to perform this task. A final point is that any proposed x-ray tool would not measure directly the zonal isolation, but infer it based on physical parameters.

8 Conclusion

- Safe generation of x-rays is a challenge, as the power required for generation of photons with sufficient energy to penetrate the casing and satisfactorily in the annuli exceed what is commercially available.
- Piezoelectric crystals are not applicable in our situation in their current state. The temperature cycles required to generate photons would reduce the logging speed to such levels that they are no longer feasible for use.
- Radioisotopes can provide photons with sufficient energies to penetrate the casing, but safe use and disposal of the radioisotopes are a concern.
- If required generation of photon energies with an x-ray tube were to be achieved the heat generation would be significant, cooling counter-measures needs to be designed.
- X-rays experience higher attenuation when passing through high density materials such as casing steel.
- Attenuation due to the Compton Effect is dependent on the incident beam, resulting in a significant effect on the attenuation of the beam, and must be accounted for.
- An increase the scattering angle relative to the incident beam reduces the attenuation from the Compton Effect but increases the attenuation from the additional length the beam has to travel to reach the detector.
- Detection of photons in a wellbore is a challenge, as the PMT cannot withstand the temperatures that will occur if an electric generator is used
- Preliminary analysis of x-ray performance of cement evaluation at the cement-formation interface it is not achievable.
- Modification of Lambert's Law to account for the porosity of the materials in addition to its ability to accurately describe the inhomogeneity found in the wellbore is required.

9 Future Work

- Determination of heat generated when using an electric generator and modelling of heat dissipation in the wellbore, and subsequent required cooling schemes.
- Modelling of the photoelectric absorption and Compton scattering differential cross-sections, and the inclusion of secondary scattering effects and radiation.
- Experimental work and modification of the model to account for porosity and density of non-homogenous materials.
- Investigation of information extraction from returning photons
- Experimental determination of the validity of Lambert's law to describe micro annuli and voids.
- Run Monte-Carlo N-particle (MCNP) simulations to simulate detector response.
- Investigation of the viability of neutrons for cement evaluation. Neutrons are heavily attenuated by materials with low atomic numbers, opposite of x-rays. Reducing the challenge of casing penetration.

Bibliography

Abshire, L.W., P. Desai, D. Mueller et al. 2012. Offshore Permanent Well Abandonment (in *Oilfield Review* **24** (1): 42 - 50. https://www.slb.com/resources/publications/industry_articles/oilfield_review/2012/or2012spr04_abandon.aspx

Albert, L.E., T.E. Standley, L.N. Tello et al. 1988. A Comparison of CBL, RBT, and PET Logs in a Test Well With Induced Channels (in *Journal of Petroleum Technology* **40** (09): 1,211 - 1,216.https://doi.org/10.2118/16817-PA

Als-Nielsen, J., D. McMorrow. 2001. *Elements of Modern X-Ray Physics* Chichester, West Sussex, Wiley (Reprint).

Ashena, R., G. Thonhauser, D. Dianati. 2014. Assessment of Reliability of Cement Bond Evaluation with Some Interesting Field Case Studies. Abu Dhabi International Petroleum Exhibition and Conference, Abu Dhabi, UAE, 10-13 November. https://doi.org/10.2118/172039-MS

Attix, F.H., ed. 2007. *Introduction to Radiological Physics and Radiation Dosimetry*, Wiley.

Benge, G. 2016. Cement Evaluation--A Risky Business (in *SPE Drilling & Completion* **30** (04): 322 - 326. SPE-170712-PA.https://doi.org/10.2118/170712-PA

Berger, M.J., J.H. Hubbell, S.M. Seltzer et al. 2010. *NIST Standard Reference Database 8* trans. Office of Health and Environmental Research Department of Energy, Washington (Reprint).

Boone, K., A. Ridge, R. Crickmore et al. 2014. Detecting Leaks in Abandoned Gas Wells with Fibre-Optic Distributed Acoustic Sensing. International Petroleum Technology Conference, Doha, Qatar 19-22 January. IPTC-17530-MS https://doi.org/10.2523/IPTC-17530-MS

Chen, S., R. Cheng. 2013. Research on temperature measurement by X-ray transmission intensity (in *Nuclear Instruments and Methods in Physics Research Section B: Beam Interactions with Materials and Atoms* **296**: 61-65. http://www.sciencedirect.com/science/article/pii/S0168583X12007379.https://doi.org/10.1016/j.nimb.2012.11.014

Cleland, M. R., F. Stichelbaut. 2013. Radiation processing with high-energy X-rays (in *Radiation Physics and Chemistry* **84**: 91-99. http://www.sciencedirect.com/science/article/pii/S0969806X12003258.http://dx.doi.org/10.1016/j.radphyschem.2012.06.038

Continental Alloy & Services. 2017. L80, http://www.contalloy.com/products/grade/l80 (downloaded 13 April 2017).

Cooper, M.J. 1997. Compton scattering and the study of electron momentum density distributions (in *Radiation Physics and Chemistry* **50** (1): 63-76. http://www.sciencedirect.com/science/article/pii/S0969806X97000248.http://dx.doi.org/10.1016/S0969-806X(97)00024-8

Corni, F., M. Michelini, L. Santi et al. The Concept of the Cross Section, www.fisica.uniud.it/URDF/laurea/idifo1/.../Cross_GIREP.pdf.

Duxbury, A.C., F.T. Mackenzie, R.B. Byrne. 2017. Seawater, https://www.britannica.com/science/seawater (downloaded 18 April 2017).

ESA. 2017. Blackbody Radiation, http://sci.esa.int/jump.cfm?oid=48986 (downloaded 17 March 2017).

Eshraghi, D.T. 2013. *P&A- status on regulations and technology, and identification of potential improvements*. MS thesis, University of Stavanger, Stavanger, Norway (June 2013).

Fertl, W.H., P.E. Pilkington. 1974. A Look at Cement Bond Logs (in *Journal of Petroleum Technology* **26** (06): 607 - 617.https://doi.org/10.2118/4512-PA

Flyckt, S.O., C. Marmonier. 2002. *Photomultiplier Tubes: Principles and Applications*. Brive, France, Philips Photonics (Reprint). https://web.archive.org/web/20060908113719/http://www.jhu.edu/iic/Photomultipliers.pdf.

Fulton, D. K. 1979. *Critical Factors Affecting Cement Bond Logs*, Society of Petroleum Engineers (Reprint). https://www.onepetro.org/general/SPE-8021-MS.

Geuther, J.A. . 2007. *Radiation Generation with Pyroelectric Crystals*. PhD PhD, Rensselaer Polytechnic Institute, Troy, New York (May 2007).

Gibbs, Keith. 2017. X-rays, http://www.schoolphysics.co.uk/age16-19/Medical%20physics/text/X_rays/index.html (downloaded 27 January 2017).

Guner, D., H. Ozturk, M. Erkayaoglu. 2017. Investigation of the elastic material properties of Class G cement (in *Structural Concrete* **18** (1): 84-91. http://dx.doi.org/10.1002/suco.201600020.https://doi.org/10.1002/suco.201600020

Haldorsen, J.B.U., D.L. Johnson, T. Plona et al. 2006 Borehole Acoustic Waves (in *Oilfield Review* **18** (1).https://www.slb.com/resources/publications/industry_articles/oilfield_review/2006/or2006spr03_borehole_acoustic_waves.aspx

Hamamatsu Photonics. 2007. *Photomultiplier Tubes: Basics and Applications*, Third edition, Hamamatsu Photonics (Reprint). http://www.hamamatsu.com/resources/pdf/etd/PMT_handbook_v3aE.pdf.

Harris, W. , C. Freudenrich. 2017. How Light Works. HowStuffWorks, http://science.howstuffworks.com/light.htm/printable (downloaded 2 February 2017).

Hausner, M.B., F. Suárez, K.E. Glander et al. 2011. Calibrating Single-Ended Fiber-Optic Raman Spectra Distributed Temperature Sensing Data (in *Sensors* **11** (11): 10859. http://www.mdpi.com/1424-8220/11/11/10859.http://dx.doi.org/10.3390/s111110859

Hill's X-Ray Services. 2017. Single-Phase vs. Hi-Frequency. Hill's X-Ray Services, http://www.hillsxray.ca/single-phase-vs-hi-frequency.php (downloaded 6 March 2017).

Infocellar. 2017. Fiber Basics, http://www.infocellar.com/networks/fiber-optics/fiber.htm (downloaded 22 March 2017).

Johannessen, K., B.K. Drakeley, M. Farhadiroushan. 2012. Distributed Acoustic Sensing - A New Way of Listening to Your Well/Reservoir. SPE Intelligent Energy International, Utrecht, The Netherlands, 27-29 March. https://doi.org/10.2118/149602-MS

Jutten, J. J., A. J. Hayman. 1993. Microannulus Effect on Cementation Logs: Experiments and Case Histories. SPE Asia Pacific Oil and Gas Conference, Singapore, 8-10 February. SPE-25377-MS https://doi.org/10.2118/25377-MS

Kelkar, S.M. 2013. *Using X-ray Imaging Techniques to Determine Density of Foods*. PhD PhD, Purdue University, West Lafayette, Indiana (December 2013).

Kersey, A.D. 1996. A Review of Recent Developments in Fiber Optic Sensor Technology (in *Optical Fiber Technology* **2** (3): 291-317. http://www.sciencedirect.com/science/article/pii/S106852009690036X.http://dx.doi.org/10.1006/ofte.1996.0036

Khalifeh, M., A. Saasen, H. Hodne et al. 2013. Techniques and Materials for North Sea Plug and Abandonment Operations. Offshore Technology Conference, Houston, Texas, USA, 6-9 May. OTC-23915-MS https://doi.org/10.4043/23915-MS

Knoll, G.F. . 2010. *Radiation Detection and Measurements* Fourth edition. Hoboken, New Jersey, Wiley (Reprint).

Koks, D. 2017. Is The Speed of Light Everywhere the Same?, http://math.ucr.edu/home/baez/physics/Relativity/SpeedOfLight/speed_of_light.html (downloaded 26 February 2017).

Leigh, C.A., C.G. Finlayson, C. van der Kolk et al. 1984. Results Of Field Testing The Cement Evaluation Tool SPWLA 25th Annual Logging Symposium, New Orleans, Louisiana 10-13 June. SPWLA-1984-H

Li, M., H. Wang, G. Tao. 2015. Current and Future Applications of Distributed Acoustic Sensing as a New Reservoir Geophysics Tool (in *The Open Petroleum Engineering Journal* **8**: 272-281.http://dx.doi.org/10.2174/1874834101508010272

Liversidge, D., S. Taoutaou. 2006. Permanent Plug and Abandonment Solution for the North Sea. SPE Asia Pacific Oil & Gas Conference & Exhibition, Adelaide, Australia, 11-13 September. SPE 100771 https://doi.org/10.2118/100771-MS

NASA. 2017. The Electromagnetic Spectrum, https://imagine.gsfc.nasa.gov/science/toolbox/emspectrum1.html (downloaded 18 January 2017).

NASA. 2017. What Wavelength Goes With a Color?, https://science-edu.larc.nasa.gov/EDDOCS/Wavelengths_for_Colors.html (downloaded 15 February 2017).

Natarajan, V. 2013. What is a photon? (in *Resonance* **18** (1): 39-50.http://dx.doi.org/10.1007/s12045-013-0005-7

National Weather Service. 2017. Introduction to Remote Sensing, http://www.srh.noaa.gov/jetstream/remote/remote_intro.html (downloaded 18 January 2017).

Nave, R. Auger Effect. Georgia State University, http://hyperphysics.phy-astr.gsu.edu/hbase/Atomic/auger.html.

Nave, R. 2017. Characteristic X-Rays http://hyperphysics.phy-astr.gsu.edu/hbase/quantum/xrayc.html (downloaded 25 January 2017).

Nave, R. Specific Heat. Georgia State University, http://hyperphysics.phy-astr.gsu.edu/hbase/thermo/spht.html.

Nave, R. 2017. Traveling Wave Relationship, http://hyperphysics.phy-astr.gsu.edu/hbase/wavrel.html (downloaded 20 January 2017).

Nelson, E.B., D. Guillot. 2006. *Well Cementing*, Second edition. Sugar Land, Texas, Schlumberger (Reprint).

Norsok D-010. 2004. Well Integrity in Drilling and Well Operations.

Oil & Gas Uk. 2012a. Guidelines for suspension and abandonment of wells.

Oil & Gas UK. 2012b. *Guidelines on qualification of materials for the suspension and abandonment of wells*, Oil & Gas UK (Reprint).

Oil & Gas UK. 2016. Decommissioning Insight

Oishi, K, T Umeno, N Takeuchi et al. 2014. Improved Calibration Method for Raman Distributed Temperature Sensor (in.https://www.researchgate.net/publication/282321118_Improved_calibration_method_for_Raman_distributed_temperature_sensor

Parker, Tom, Sergey Shatalin, Mahmoud Farhadiroushan. 2014. Distributed Acoustic Sensing – a new tool for seismic applications (in *First Break* **32** (2): 61-69.http://dx.doi.org/10.3997/1365-2397.2013034

Pilkington, P.E. 1992. Cement Evaluation - Past, Present, and Future (in *Journal of Petroleum Technology* **44** (02): 132 - 140. SPE-20314-PA.https://doi.org/10.2118/20314-PA

Podgorsak, E.B. 2010. *Radiation Physics for Medical Physicists*, Second edition. Heidelberg Dordrecht, London, New York: Biological and Medical Physics, Biomedical Engineering, Springer (Reprint).

Radiologykey. 2017. The X-ray Tube, https://radiologykey.com/the-x-ray-tube-2/#s0025 (downloaded 25 January 2017).

Read, H. S. 1926. Some Effects of Temperature on X-Ray Absorption (in *Physical Review* **28** (5): 898-906. https://link.aps.org/doi/10.1103/PhysRev.28.898.https://doi.org/10.1103/PhysRev.28.898

Scanlon, E., G.L. Garfield. 2011. New Technologies to Enhance Performance of Section Milling Operations that Reduces Rig Time for P&A Campaign in Norway. SPE/IADC Drilling Conference and Exhibition, Amsterdam, The Netherlands 1-3 March. SPE-140277-MS https://doi.org/10.2118/140277-MS

Schmidt, M.G. 1989. The Micro CBL - A Second Generation Radial Cement Evaluation Instrument. SPWLA 30th Annual Logging Symposium, Denver, Colorado, 11-14 June. SPWLA-1989-Z

Serman, N. Production of X-rays and Interactions of X-rays with Matter, http://www.columbia.edu/itc/hs/dental/sophs/material/production_xrays.pdf.

Sheives, T. C., L. N. Tello, V. E. Maki, Jr. et al. 1986. A Comparison of New Ultrasonic Cement and Casing Evaluation Logs With Standard Cement Bond Logs. SPE Annual Technical Conference and Exhibition, New Orleans, Louisiana, 5-8 October. SPE-15436-MS https://doi.org/10.2118/15436-MS

Shook, E.H., T.W. Lewis. 2008. Cement Bond Evaluation. SPE Western Regional and Pacific Section AAPG Joint Meeting, Bakersfield, California, USA, 29 March-4 April. SPE-108415-MS https://doi.org/10.2118/108415-MS

Skalle, P. 2001. Cementing problems when setting casing through porous gas & water bearing formations. 52. Berg- und Huttenmannsicher Tag, Freiberg Research Forum, Freiberg, Germany, 20-22 June. www.ipt.ntnu.no/~pskalle/files/.../24_cementing.pdf

Smolen, J.J, A. van der Spek. 2003. Distributed Temperature Sensing: A DTS Primer for Oil and Gas Production. Shell International Exploration and Production, The Hague, The Netherlands. w3.energistics.org/schema/witsml_v1.../Shell_DTS_Primer.pdf

Tada, H. 2017. Chapter 1: Overview of Heat Transfer, http://emerald.tufts.edu/as/tampl/en43/lecture_notes/ch1.html (downloaded 4. March 2017).

Technical Manual. 2016. Nondestructive inspection methods, basic theory, United States Air Force (15 October).

The Physics Classroom. 2017. Optical Density and Light Speed, http://www.physicsclassroom.com/Class/refrn/u14l1d.cfm#table (downloaded 3 March 2017).

van Biezen, M. 2017. Physics - Modern Physics (6 of 26) X-Rays https://www.youtube.com/watch?v=AGJq39byYKk (downloaded 20 January 2017).

van der Kuip, M. D. C., T. Benedictus, N. Wildgust et al. 2011. High-level integrity assessment of abandoned wells (in *Energy Procedia* **4**: 5320-5326. http://www.sciencedirect.com/science/article/pii/S1876610211007922.http://dx.doi.org/10.1016/j.egypro.2011.02.513

Wenatchee, H.S. 2017. Chapter 6 Lecture Notes. Wenatchee High School (downloaded 5 March 2017).

Wikipedia. 2017. Refractive index, https://en.wikipedia.org/wiki/Refractive_index (downloaded 17 March 2017).

Wikipedia. 2017. Snell's law, https://en.wikipedia.org/wiki/Snell%27s_law (downloaded 17 March 2017).

Wittke, J.H. 2017. Signals. Northern Arizona University, http://nau.edu/cefns/labs/electron-microprobe/glg-510-class-notes/signals/#Absorption_of_electromagnetic_radiation (downloaded 5 April 2017).

Wu, Q., S. Nair, M. Shuck et al. 2016. Advanced Distributed Fiber Optic Sensors to Monitor Cement Hydration and Detect Annular Hydrocarbon Migration for Enhanced Zonal Isolation. SPE Annual Technical Conference and Exhibition, Dubai, UAE 26-28 September. SPE-181429-MS https://doi.org/10.2118/181429-MS

Zentai, G. 2008. X-ray Imaging for Homeland Security. IEEE International Workshop on Imaging System and Techniques, Chania, Greece, 10-12 September. http://dx.doi.org/10.1109/IST.2008.4659929